MACHINE LEARNING-INCORPORATED TRANSIENT STABILITY PREDICTION AND PREVENTIVE DISPATCH FOR POWER SYSTEMS WITH HIGH WIND POWER PENETRATION

A Thesis Submitted to the
College of Graduate and Postdoctoral Studies
In Partial Fulfillment of the Requirements
For the Degree of Doctor of Philosophy
In the Department of Electrical and Computer Engineering
University of Saskatchewan
Saskatoon

By

YUCHUAN CHEN

Permission to use

In presenting this thesis in partial fulfillment of the requirements for a Postgraduate degree from the University of Saskatchewan, I agree that the Libraries of this University may make it freely available for inspection. I further agree that permission for copying of this thesis in any manner, in whole or in part, for scholarly purposes may be granted by the professor or professors who supervised my thesis work or, in their absence, by the Head of the Department or the Dean of the College in which my thesis work was done. It is understood that any copying or publication or use of this thesis or parts thereof for financial gain shall not be allowed without my written permission. It is also understood that due recognition shall be given to me and to the University of Saskatchewan in any scholarly use which may be made of any material in my thesis.

Requests for permission to copy or to make other uses of materials in this thesis/dissertation in whole or part should be addressed to:

Head of the Department of Electrical and Computer Engineering
University of Saskatchewan
57 Campus Drive
Saskatoon, Saskatchewan, S7N 5A9
Canada

OR

Dean
College of Graduate and Postdoctoral Studies
University of Saskatchewan
116 Thorvaldson Building, 110 Science Place
Saskatoon, Saskatchewan (S7N 5C9)
Canada

Abstract

Historically, transient instability has been the most severe stability challenge for most systems. Transient stability prediction and preventive dispatch are two important measures against instability. The former measure refers to the rapid prediction of impending system stability issues in case of a contingency using real-time measurements, and the latter enhances the system stability against preconceived contingencies leveraging power dispatch. Over the last decade, large-scale renewable energy generation has been integrated into power systems, with wind power being the largest single source of increased renewable energy globally. The continuous evolution of the power system poses more challenges to transient stability. Specifically, the integration of wind power can decrease system inertia, affect system dynamics, and change the dispatch and power flow pattern frequently. As a result, the effectiveness of conventional stability prediction and preventive dispatch approaches is challenged.

In response, a novel transient stability prediction method is proposed. First, a stability index (SI) that calculates the stability margin of a wind power-integrated power system is developed. In this method, wind power plants (WPPs) are represented as variable admittances to be integrated into an equivalent network during transients, whereby all WPP nodes are eliminated from the system, while their transient effects on each synchronous generator are retained. Next, the calculation of the kinetic and potential energies of a system is derived, and accordingly, a novel SI is put forward. The novel approach is then proposed taking advantage of the machine learning (ML) technique and the newly defined *SI*. In case of a contingency, the developed *SI* is calculated in parallel for all possible instability modes (IMs). The *SI*s are then formed as a vector and applied to an ensemble learning-trained model for transient stability prediction. Compared with the features used in other studies, the SI vector is more informative and discriminative, thus lead to a more accurate and reliable prediction. The proposed approach is validated on two IEEE test systems with various wind power penetration levels and compared to the existing methods, followed by a discussion of results.

In addition, to address the issues existing in preventive dispatch for high wind power-integrated electrical systems, an hour-ahead probabilistic transient stability-constrained power dispatching method is proposed. First, to avoid massive transient stability simulations in each dispatching operation, an ML-based model is trained to predict the critical clearing time (CCT) and IM for all preconceived fault scenarios. Next, a set of IM-categorized probabilistic transient stability constraints (PTSCs) are constructed. Based on the predictions, the system operation plan is assessed with respect to the PTSCs. Then, the sensitivity of the probabilistic level of CCT is calculated with respect to the active power generated from the critical generators for each IM category. Accordingly, the implicit PTSCs are converted into explicit dispatching constraints, and the dispatch is rescheduled to ensure the probabilistic stability requirements of the system are met at an economical operating cost. The proposed approach is validated on modified IEEE 68- and 300-bus test systems, wherein the wind power installed capacity accounts for 40% and 50% of the total load, respectively, reporting high computational efficiency and high-quality solutions.

The ML-incorporated transient stability prediction and preventive dispatch methods proposed in this research work can help to maintain the transient stability of the system and avoid the widespread blackouts.

Acknowledgments

My deepest appreciation goes to my supervisors: Prof. C. Y. Chung and Prof. S. O. Faried, for their continuous support of my Ph.D. study and for their patience, guidance, enthusiasm, encouragement and devotion. I have learned invaluable lessons from their expertise, vision, and personality. I could not imagine having better supervisors for my study. One of the greatest blessings I have had in my life is to be their student.

Also, I would like to express my sincere gratitude to Prof. B. C. Pal. Thank you for accepting me as a visiting student; it was a memorable experience to be one of your lab members.

My sincere thanks also go to my advisory committee members, Prof. Xiaodong Liang, Prof. Rajesh Karki, Prof. Seok Bum Ko, Prof. Safa Kasap, Prof. Reza Fotouhi and Prof. Xiaozhe Wang, for their insightful comments, valuable suggestions and hard questions, which helped me to improve the quality of my thesis.

I am highly indebted to the University of Saskatchewan, where I had many spectacular times and met loads of bosom friends. I also owe a deep sense of gratitude to my lab members: Mahdi, Weijia, Joe, Jim, Peiyan, Bo, Bingzhi, Osama, Nima, Alireza, Benyamin and all other SMARTGEN lab members; Please forgive me for not listing all of your names, my appreciation extends deeply and equally to each of you. Thanks for always helping me academically and in daily life. You have made me a better person.

Above all, I am extremely thankful to my parents for giving birth to me, bringing me up, and supporting my decisions. And my wife, Yinfei, who always has on my side and supports me spiritually; there are three things I adore most: the sun, the moon and you—the sun for the day, the moon for the night, and you forever.

Table of Contents

List of Tables

List of Figures

List of Symbols and Abbreviations

Abbreviations

ANN	Artificial neural network
AVG-IWP	Average pre-fault instantaneous wind power penetration
CART	classification and regression tree
CCT	Critical clearing time
DAE	Differential-algebraic equation
DFIG	Doubly-fed induction generator
DT	Decision tree
EEAC	Extended equal area criterion
IM	Instability mode
ML	Machine learning
OMIB	One-machine-infinite-bus
OPF	Optimal power flow
PDF	Probability distribution function
PI	Prediction interval
PMU	Phasor measurement unit
POI	Point of intersection
PTSC	Probabilistic transient stability constraint
RES	Renewable energy sources
RT-I	First robustness test
RT-II	Second robustness test
SG	Synchronous generator
SI	Stability index
SVM	Support vector machine
TDS	Time-domain simulation.
TEF	Transient energy function
TSC-OPF	Transient stability constrained OPF
UEP	Unstable equilibrium point
WD	Wasserstein distance

WG	Wind generator
WIC	Wind power installed capacity ratio
WPP	Wind power plant

Sets/indices

Ω^{B}	Set of buses
Ω^{C}	Set of critical SGs which are responsible for the loss of synchronism
Ω^{R}	Set of remaining SGs, i.e., set of SGs which are not in Ω^{C}
Ω^{G}	Set of WPPs whose POI voltages are heavily influenced by SGs in Ω^{C}
Ω^{H}	Set of WPPs which are not in Ω^{G}
Ω^{IM}	Set of all IMs that may appear in system
Ω^{L}	Set of transmission lines
Ω^{OP}	Set of possible operating points.
Ω^{f}	Set of fault scenarios that are used to generate a database for training the transient stability prediction model
Ω^{SG}	Set of SGs in system
Ω^{w}	Set of wind power generation scenarios considered in a preventive dispatching operation
$\Omega^{\mathcal{L},\mathrm{OP}}$	Set of fault scenarios considered in a preventive dispatching operation
$\Omega^{\mathrm{CCT,IM}}$	Set of data pairs (CCT, IM), where each pair contains the CCT and IM of a fault scenario
Ω_k^{C}	Set of critical SGs of IM k
Ω_k^{R}	Set of remaining SGs of IM k, i.e., set of SGs not in Ω_k^{C}
$\boldsymbol{u}$	Set of control variables in power dispatch.
$\boldsymbol{\varepsilon}$	Set of uncertainties that might change system operating point
g	Index of Ω^{G}
h	Index of Ω^{H}
k	Index of Ω^{IM}
w	Index of WPPs, i.e., index of $(\Omega^{\mathrm{G}} \cup \Omega^{\mathrm{H}})$

Variables:

A_{acc}	"Accelerating area" of equivalent OMIB system

A_{dec}	"Decelerating area" of equivalent OMIB system
$\vec{E}_i$	Complex voltage of the internal node of SG_i
E_i	Magnitude of $\vec{E}_i$
$\vec{I}_i$	Complex current injection of the internal node of SG_i
M_C	Equivalent inertia of Ω^{C}
M_R	Equivalent inertia of Ω^{R}
M_T	Summation of M_T and M_R
M_i	Inertia of SG_i
M	Inertia of equivalent OMIB system
P	Electrical power of equivalent OMIB system
P_i	Active power output of SG_i
P_{mech}	Mechanical power of equivalent OMIB system
$P_{mech,i}$	Mechanical power output of SG_i
P_w	Active power output of WPP_w
P_{Wi}	Active power injection of WPP at bus i
P_k^{C}	Active power generated from Ω_k^{C}
P_k^{R}	Active power generated from Ω_k^{R}
$\Delta P_k^{\mathrm{C,obj}}$	Objective amount of active power to be shifted from Ω_k^{C} to Ω_k^{R} against IM k.
Q_i	Reactive power output of SG_i
Q_w	Reactive power output of WPP_w
Q_{Wi}	Reactive power output of WPP at bus i
t_{cl}	Fault clearance time
t_{cl+}	Moment right after t_{cl}
t_{cl-}	Moment right before t_{cl}
t_{cu}	Time period during t_{cl} to t_u
t_{f}	Fault time
$t_{\mathrm{f}+}$	Moment right after t_{f}
$t_{\mathrm{f}-}$	Moment right before t_{f}
t_u	Moment when system reaches the unstable equilibrium point

$\vec{V}_w$	Complex voltage of POI of WPP_w
V_w	Voltage magnitude of POI of WPP_w
V_{SG}	Terminal voltage of SG
Y'_m	Variable admittance connected at node m
δ	Rotor angle of equivalent OMIB system
δ_C	Equivalent rotor angle of Ω^{C}
δ_R	Equivalent rotor angle of Ω^{R}
δ_i	Rotor angle of SG_i
δ_u	Rotor angle of equivalent OMIB system at t_u
θ_h	Voltage angle of the POI of h
θ_g	Voltage angle of the POI of g
$\psi_{\varkappa}$	Stability status of contingency $\varkappa$
ω	Angular speed
$\varpi_{i,j}$	Weight of sample i for building individual learner $\hbar_j(\cdot)$
$\rho_k(\text{CCT} > \alpha_k)$	Probability of $\text{CCT} > \alpha_k$.
ϱ_j	Weight of the new individual learner $\hbar_j(\cdot)$
ϵ_j	Weighted sum error for misclassified samples of individual learner $\hbar_j(\cdot)$
ς_k	Sensitivity of $\rho_k(\text{CCT} > \alpha_k)$ to the active power generated from Ω_k^C.
$\mathcal{L}$	List of fault lines created by sampling the elements in Ω^{L} according to $\boldsymbol{\zeta}$.

Parameters/ Constants:

α_k	Threshold value of CCT set for IM k.
β_k	Acceptable security level set for $\rho_k(\text{CCT} > \alpha_k)$.
φ	A threshold ratio to compare $V_w(t_{c+})$ to $V_w(t_{\text{f}-})$.
P_{const}	A constant used to calculate A_{acc} and A_{dec}
P_{max}	A constant used to calculate A_{acc} and A_{dec}
γ	A constant used to calculate A_{acc} and A_{dec}
$\underline{\Delta P}$	Threshold value to check the maximum power output change in all SGs between two consecutive iterations
T	Time interval between two consecutive dispatching operations

$\eta_1 - \eta_3$	Coefficients used to calculate A_{dec}
$\xi_1 - \xi_6$	Coefficients used to calculate A_{acc}
$\mathcal{M}$	Maximum allowed number of iterations
N	Number of training samples

Matrices & Vectors

$\boldsymbol{E}_R$	Matrix that includes the magnitudes of each element in $\vec{\boldsymbol{E}}_R$
$\boldsymbol{E}_C$	Matrix that includes the magnitudes of each element in $\vec{\boldsymbol{E}}_C$
$\vec{\boldsymbol{E}}_C$	Complex voltage column vector of internal nodes of SGs in Ω^{C}
$\vec{\boldsymbol{E}}_R$	Complex voltage column vector of internal nodes of SGs in Ω^{R}
$\vec{\boldsymbol{I}}_C$	Complex current column vector of internal nodes of SGs in Ω^{C}
$\vec{\boldsymbol{I}}_R$	Complex current column vector of internal nodes of SGs in Ω^{R}
$\vec{\boldsymbol{I}}_G$	Complex current column vector of POIs of WPPs in Ω^{G}
$\vec{\boldsymbol{I}}_H$	Complex current column vector of POIs of WPPs in Ω^{H}
$\boldsymbol{Q}_G$	Reactive power injection column vector of POIs of WPPs in Ω^{G}
$\boldsymbol{Q}_H$	Reactive power injection column vector of POIs of WPPs in Ω^{H}
$\boldsymbol{SI}$	SI vector, which consists of SI values of all feasible IMs of system
$\boldsymbol{V}_G$	Column vector that includes the magnitudes of each element in $\vec{\boldsymbol{V}}_G$
$\boldsymbol{V}_H$	Column vector that includes the magnitudes of each element in $\vec{\boldsymbol{V}}_H$
$\vec{\boldsymbol{V}}_G$	Complex voltage column vector of POI of WPPs in Ω^{G}
$\vec{\boldsymbol{V}}_H$	Complex voltage column vector of POI of WPPs in Ω^{H}
$\boldsymbol{X}_i$	Column vector of features of sample i
$\boldsymbol{Y}_{CC}$	Admittance matrix of nodes in set Ω^{C}
$\boldsymbol{Y}_{CG}$	Mutual admittance matrix between nodes in sets Ω^{C} and Ω^{G}
$\boldsymbol{Y}_{CH}$	Mutual admittance matrix between nodes in sets Ω^{C} and Ω^{H}
$\boldsymbol{Y}_{CR}$	Mutual admittance matrix between nodes in sets Ω^{C} and Ω^{R}
$\boldsymbol{Y}_{GG}$	Admittance matrix of nodes in set Ω^{G}
$\boldsymbol{Y}_{GC}$	Mutual admittance matrix between nodes in sets Ω^{G} and Ω^{C}
$\boldsymbol{Y}_{GH}$	Mutual admittance matrix between nodes in sets Ω^{G} and Ω^{H}
$\boldsymbol{Y}_{GR}$	Mutual admittances matrix between nodes in sets Ω^{G} and Ω^{R}

$\boldsymbol{Y}_{HH}$	Admittance matrix of WPPs nodes in set Ω^{H}
$\boldsymbol{Y}_{HC}$	Mutual admittance matrix between nodes in sets Ω^{H} and Ω^{C}
$\boldsymbol{Y}_{HG}$	Mutual admittance matrix between nodes in sets Ω^{H} and Ω^{G}
$\boldsymbol{Y}_{HR}$	Mutual admittance matrix between nodes in set Ω^{H} and Ω^{R}
$\boldsymbol{Y}_{RR}$	Admittance matrix of nodes in set Ω^{R}
$\boldsymbol{Y}_{RC}$	Mutual admittance matrix between nodes in sets Ω^{R} and Ω^{C}
$\boldsymbol{Y}_{RG}$	Mutual admittance matrix between nodes in sets Ω^{R} and Ω^{G}
$\boldsymbol{Y}_{RH}$	Mutual admittance matrix between nodes in sets Ω^{R} and Ω^{H}
$\boldsymbol{Y}'_{RR}$	Admittance matrix of nodes in Ω^{R} after eliminating WPP nodes from system
$\boldsymbol{Y}'_{CC}$	Admittance matrix of nodes in Ω^{C} after eliminating WPP nodes from system

Functions:

$\boldsymbol{\zeta}$	Probability distribution function of fault occurrence for each transmission line
$\mathcal{F}(\cdot)$	Function of an ensemble model
$\hbar_j(\cdot)$	Function of individual learner *j*
$\mathcal{H}_k(\cdot)$	Function that describes $\rho_k(\mathrm{CCT} > \alpha_k)$.
$\wp(\cdot)$	Probability distribution function of CCT

1 Introduction

1.1 Motivation

Power systems are usually subjected to various weather conditions and fortuitous events that may lead to incidents causing partial or complete instability of the grid, followed by widespread blackouts. During the last several decades, large-scale blackouts caused by large-disturbances in power systems occurred in many countries, including the United States, Canada, Italy, India, etc. Table 1.1 lists some of the major power outages during the past two decades. These incidents resulted in enormous national economic losses and affected millions of customers.

Table 1.1: List of selected power system blackouts.

Incident	Affected population(millions)	Location	Date
2019 Java blackout	120	Indonesia	August 4 –5
2019 Venezuelan blackout	30	Venezuela	March 7–March 14
2016 Sri Lanka blackout	21	Sri Lanka	March 13
2015 Pakistan blackout	140	Pakistan	January 26
2014 Bangladesh blackout	150	Bangladesh	November 1
2012 India blackout	620	India	July 30–31
2003 Northeast blackout	55	Canada and the United States	August 14–28
2003 Italy blackout	56	Italy and Switzerland	September 28
2001 India blackout	230	India	January 2

Historically, transient stability, also known as large-disturbance rotor angle stability, has been the most severe stability problem in most systems [1]. *Transient stability prediction* and *preventive dispatch* are two important measures against transient instability. *Transient stability prediction* refers to the rapid prediction of system stability in case of a contingency using real-time measurement data. Fast prediction of the potential instabilities allows more time for remedial actions, thus minimizing the impacts of instability on the system. By contrast, *preventive dispatch* is concerned with dispatching the generation in the power system so that the required stability level is obtained. In short, the former predicts the impending stability status of post-fault systems, while the latter enhances the system stability against preconceived contingencies by power dispatch. These two measures are of great significance in improving the system stability level and avoiding widespread blackouts.

Several studies have explored the solutions regarding the two measures and achieved certain results. However, the existing methods may face severe dilemmas as the power systems are keeping evolving. One of the most significant changes in power systems over the last few years is the growing integration of renewable energy sources (RESs) and their related devices. High participation of RESs in power systems, on one hand, helps in reducing carbon emissions; on the other hand, it may significantly affect the operating condition and transient behavior of power systems in unfavorable manner [2]−[9]. Moreover, high penetration of RESs conversion systems may degrade the solution quality, increase computational burden and diminish the applicability of conventional transient stability prediction and preventive dispatch methods. Therefore, it is felt that more research should be done on developing novel countermeasure methods, including new transient stability prediction and preventive dispatch techniques.

1.2 Literature Review

This section presents a thorough review of the current literature, including the changing trend of the power systems in terms of integration of wind energy, transient stability prediction studies, preventive dispatch studies, and the application of Machine Learning (ML) in power systems.

1.2.1 Integration of Wind Energy

With increasing concerns about energy security, fuel diversity, and climate change, many countries worldwide have implemented policies supporting green energy [10]. During the last few years, wind energy has positioned itself as the world's most promising RES. In terms of install capacity, in 2019, 60.4 GW of wind energy capacity was installed globally, increasing 19% over

2018 and bringing the total global capacity over 651 GW [11]. In Canada, 13,413 MW of wind energy capacity are installed until 2019 [12]. Specifically, the province of Saskatchewan has committed to increasing its wind-power capacity from 5% currently to 30% by 2030 [13]. In terms of electricity consumption, wind energy has gone from a niche to a mainstream energy source in recent decades. For example, in China, it constitutes the third largest energy source. In Europe, wind power covered 47% of the electricity demand of Denmark in 2019, followed by Ireland at 32%, and Portugal at 27% [14]. In the United States, wind energy provided the source of 7.3% of the nation's electricity generation [15]. As for Canada, wind power accounted for 5.1% of electricity generation in 2018 [12].

1.2.2 Transient Stability Prediction

1.2.2.1 Stability Issues

Power system stability issues can be broadly classified as: transient stability, small-signal rotor angle stability, voltage stability, and frequency stability [1]. The categorization of power system stability is based on the physical nature of the resulting mode of instability, the size of the disturbance considered, and the devices involved, as well as the time span of interest [1], [16].

In the studies presented in this thesis, attention is focused on transient stability as it has been the most severe stability challenge for most systems. Transient stability is the ability of a power system to maintain synchronism when subjected to a large disturbance (e.g. a system fault, a loss of a major transmission line and the sudden application of a large load). Under any steady-state operating condition, there is an equilibrium between the electromagnetic torque and mechanical torque of each synchronous generator (SG) in the system. This equilibrium is disturbed as faults occur, resulting in a single or multiple SGs temporarily run faster than the rest. In this situation, the relative rotor angle between the "faster" and "slower" SGs increases. Due to the kinetic energy accumulated during the disturbance, this increasing trend generally continues for a short period of time after the disturbance is cleared. If the system can completely absorb the kinetic energy before the relative rotor angle reaches a certain limit, the synchronism of the system is restored; while if the value of the relative rotor angle exceeds a certain limit, the relative rotor angle irreversibly increases and the synchronism of the system will be lost and instability occurs. The time frame of interest in transient stability studies is usually 1 to 5 seconds following the disturbance. Loss of synchronism can occur between one SG and the rest of the system, or between groups of SGs. Transient stability of the system is affected by several factors, including the nature of the system (devices connected, system topology, system scale, etc.), the location, type and duration of the contingency, the original operating point of the system before the contingency, etc.

1.2.2.2 When to and Why Predict

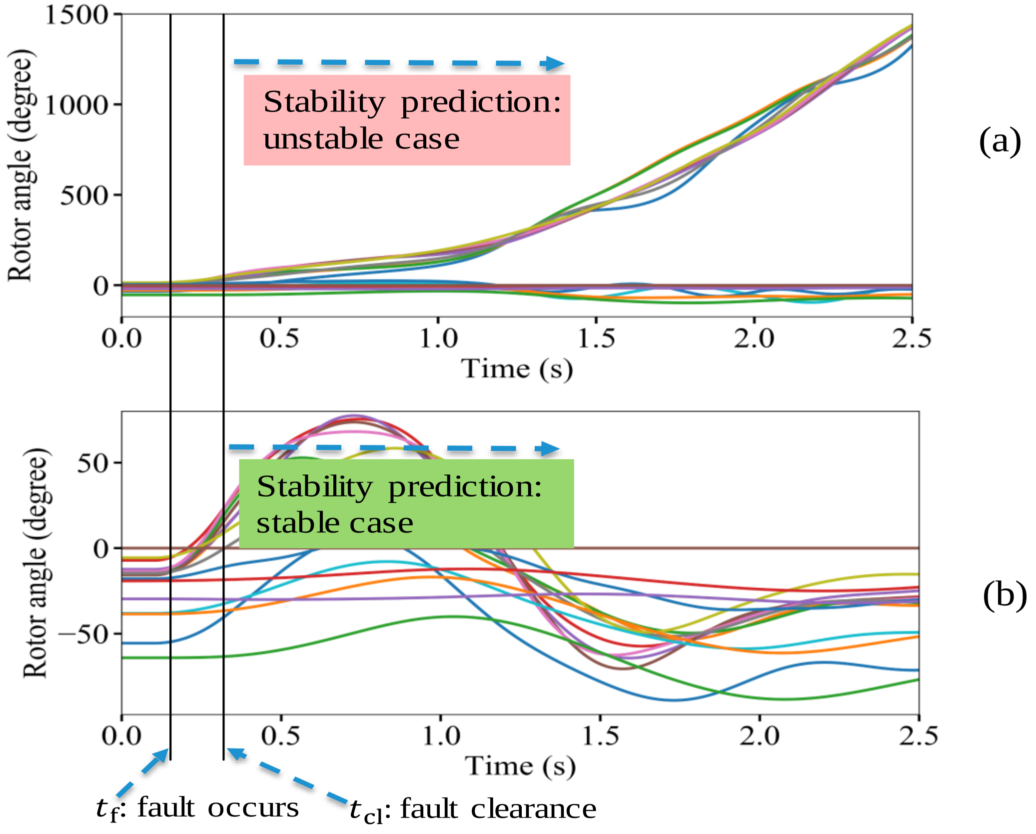

Figure 1.1: Relative generator rotor angles resulting from a system fault.
(a) Unstable case. (b) Stable case.

The loss of synchronism of a power system may occur within seconds after a disturbance. As an illustrative example, Figure 1.1 shows two cases of the rotor angle curves of the SGs when subjected to contingencies. The simulation is conducted on IEEE 16-machine 68-buses system. Figure (a) is an unstable case, as the relative rotor angles of two SG groups are keeping diverging after a contingency, and accordingly, the synchronism of the system is destroyed. In contrast, figure (b) shows a stable case, where all the rotor angles of the “faster” SGs go back to synchronous after oscillations. A prediction method should predict whether the system will be stable accurately as soon as possible right after fault clearance [17]. If the system will remain stable, then no more remedial action is required; thus, unnecessary operations can be avoided. Otherwise, remedial actions, such as islanding, load shedding and generator tripping, should be triggered immediately. Generally, the earlier the actions are triggered, the greater the probability that the synchronism of the system is restored.

1.2.2.3 Current Candidate Methods

Several techniques have been used for transient stability prediction. These techniques can be generally classified into three basic categories:

1) Time-domain simulations,

2) Transient Energy Function (TEF)-based methods, and

3) Machine-Learning (ML) -based prediction techniques [17].

Among these techniques, time-domain simulation is the most accurate option in which power system dynamic models are represented by sets of differential-algebraic equations (DAEs) that are solved in each time step during simulation and the stability of the system can be determined by analyzing the behavior of the SG rotor angles [18], [19]. This approach requires accurate information about the network configuration to conduct the accurate simulation. There are multiple commercial power system simulation packages that are capable of carrying out reliable transient simulations, including but not limited to DSATools [20], DIgSILENT PowerFactory [21], EMTP [22], ETAP [23], Power world [24], PSS/E [25], PSCAD [26], etc. However, this approach is mainly for offline power system studies and may not be suitable for online stability prediction. This is because the system may face transient instability for a short period, ranging from 10 cycles to a few seconds after a severe fault [27]. Hence, it is almost impossible to complete a transient stability simulation for stability prediction in this short period, specifically for a large network.

The family of TEF-based stability assessment methods is another candidate approach for stability prediction [28]–[43]. Utilizing simplified power system models, these methods can rapidly evaluate the kinetic and potential energies of a post-fault system, thus obtaining the stability margin by comparing the two energies. Due to their excellent performance at computation speeds, these methods are mostly used in fast contingency screening and online transient stability assessment, i.e., assess the system operating status by carrying out transient simulation for all preconceived contingencies. Nevertheless, there are still some problems in their application in power system stability prediction [2]. First, the accuracy of these methods may subject to the complexity of power systems. In addition, considering the uncontrollable error, these methods may be more suitable for comparing the relative stability of a system under various faults, other than making stability prediction, which is a ‘Yes’ or ‘No’ question. Besides, these approaches require accurate identification of the instability mode (IM), known as clustering of the critical and remaining generators, during the calculation; yet, the identification process may delay the decision-making [44]–[45].

Last but not least, the ML-based technique is another popular approach for transient stability prediction thanks to the widespread use of phasor measurement units (PMUs) in power systems [46]. PMUs are devices measuring the data of power systems in real-time, such as voltage and current phasors with a reporting frequency of typically 30–60, even 100 samples per second [47]–[53]. Due to the availability of real-time power system data, ML techniques have been received increasing attention for transient stability prediction. Different ML techniques, e.g., decision trees (DTs) [17], [54]−[58] artificial neural networks (ANNs) [59], [60], support vector machines (SVMs) [61], [62], extreme learning machine [63], and core vector machine [64] have been applied so far to process real-time synchronized data and make online transient stability prediction. In most methods, pre- and post-fault data, such as time series voltages and rotor angles, are served as input features. ML-based prediction methods are prominent in calculation speed and are adaptable to bulk power systems. Still, the integration of wind power plants (WPPs) and their controllers are changing the static and dynamic characteristics of power systems, which may affect the performance of the existing ML-based prediction approaches [2]−[9]. First, the output of WPPs can vary both temporally and spatially, which exponentially increases the required training data [65]. Second, as uncertainties and complexity of the system increase, existing features such as bus voltages, which are obtained via PMU measurements, may no longer be so useful [17], [56], [66]. Third, most of the ML-based studies mentioned above utilize post-fault data obtained after fault clearance for stability prediction, which postpones the forecasting phase. As corrective control action should come into effect to preserve the network as quickly as possible, fast and accurate prediction of stability status is a real concern.

1.2.3 Preventive Dispatch

In steady-state operations, power systems are expected to operate economically while maintaining the stability requirements of the grid. Such restrictions ensure avoiding huge economic losses resulted from different contingencies, such as transient instability.

In such a context, optimal power flow (OPF) has been widely studied to address the economic side, followed by exploring various solutions for transient stability constrained OPF (TSC-OPF) problem. In power system simulation, transient stability of a post-fault system is determined by solving a set of DAEs that represent the system transients, while power flow corresponds to the initial point, which significantly affects the DAEs results. However, the TSC-OPF, which is a DAE-constrained optimization problem, cannot be solved directly. One of the most popular solutions is to discretize the DAEs into a set of algebraic constraints in terms of small-time steps then solve the problem by either linear or nonlinear programming techniques [67]–[69]. Another prevalent method is the trajectory sensitivity-based technique, which iteratively adjusts the dispatch based on the sensitivity of the stability index of interest to the control variables with the aid of time-domain simulations (TDSs) [70]–[74]. The evolution algorithm-based technique is another feasible solution that seeks the optimal solution of the TSC-OPF problem uses mechanisms inspired by biological evolution [75]–[76].

Set aside the pros and cons of these approaches, however, they mainly focus on deterministic systems. Given power systems are constantly penetrated with RESs like wind power, which is highly variable even in one hour, it is important to consider stochastic variations of the renewables in power dispatch [77]. The multisource renewables and related high-level uncertainties exponentially increase the possible system pre-fault operation points. As a result, extensive operation points need to be considered for dispatch, which entails an excessive computation burden that may be computationally intractable by these approaches. In view of OPF may need to be solved hour-ahead for most systems, the high-efficiency methods are required [78], [79].

In addition, as the stochastic factors in power systems affect the transient stability level of the systems, it is necessary to analyze the effects from the probabilistic perspective instead of deterministic. An early probabilistic transient stability study is reported in [80], which considered the uncertainties of loads, fault occurrence, location, type and clearing time, and of wind generation afterward in [81]. Both studies carried out a large number of Monte Carlo TDS. Later, a point estimate method and Kalman filter are respectively applied in [82] and [83] to estimate the uncertainty of the system stability margin caused by the wind power uncertainties, which help to eliminate the excessive testing scenarios, thus reduce the computation time in TSC-OPF problem. Taguchi's orthogonal array testing is utilized in [84] to decompose the probabilistic problem into several deterministic problems, thus reduce the testing scenarios. However, these methods may lack sufficient statistics. In other words, the estimated probabilistic stability index may not contain enough uncertainty information from wind power generations. Besides, the accuracy of the estimation may degrade if the wind generation does not follow the predetermined probability distribution type, e.g., Weibull [82] and Gaussian [84]. Yet, the assumed probability distribution type cannot be valid all the time since the dynamic characteristics of wind power are highly complex.

Moreover, existing TSC-OPF studies generally cope with merely one or a few specific fault locations. However, a particular dispatching scheme made against specific fault scenarios may, in turn, deteriorate the system stability against other scenarios. Given the probabilistic nature of different contingency events, a dispatch method that reasonably allocates "stability resources" against the various potential faults can benefit the overall stability of systems. Therefore, more works are required in this regard.

1.2.4 Applications of ML in Power Systems

Over the last few decades, the power industry is moving rapidly towards digitalization and intelligence, and an impressive number of ML-related methodologies have been proposed in the power system community to facilitate this transformation.

From a technical perspective, ML techniques can be classified into (1) Supervised learning, (2) Unsupervised learning and (3) Reinforcement learning. Supervised learning is to infer a function that maps an input to an output based on example input-output pairs [85]. In academia, supervised learning techniques have been widely applied to different areas of study in power systems, including forecasting of renewable energy generation [86], stability prediction [54]–[64], stability assessment [87], [88], fault detection [89], dynamic security assessment [90], [91], system operation [92], etc. By contrast, unsupervised learning is a type of algorithm used to draw inferences from datasets consisting of input data without labelled responses. It is commonly used for cluster analysis. In [93]–[95], unsupervised learning methods are applied in forecasting and pattern recognition of residential load. Unlike supervised and unsupervised learning, reinforcement learning is concerned with how intelligent agents ought to take actions in an environment to maximize the notion of cumulative reward. In power system areas, reinforcement learning techniques have been applied in energy management [96], [97], demand response [98], [99], electricity market [100], [101], operational control [102], [103], etc.

1.3 Research Objectives

The first objective of this thesis is to develop an ML-incorporated transient stability prediction method for power systems with high wind power penetration. Based on the literature review, most of the existing methods directly borrow ML algorithms to perform stability prediction. This may lead to a lack of innovation in feature selection and algorithmic design and restrict a further improvement in prediction performance. In fact, by including the physical characteristics of the power system into the ML algorithms, the reliability and accuracy of the prediction may be considerably increased. In this context, the nature of the problem will be carefully analyzed, and a new method will be developed in this research work. Compared to existing published research, the proposed method has the following advantages: (1) More stable information is included in features. Unlike other features used in state-of-the-art methods, the features used for prediction are derived considering the physical characteristics of the power system. Therefore, the developed feature is highly recognizable and thus can lead to a more accurate and reliable prediction. (2) Reduce the post-fault data collection timeframe. Given most of the ML-based methods require long post-fault observation windows, which postpones the stability prediction phase, the proposed method reduces the dependence of post-fault data, thus increase the speed of decision-making. (3) More robust to changes in system topology and penetration level of wind power.

The second objective of the thesis is to develop a preventive transient stability dispatching approach for high wind power-integrated electrical systems. One of the difficulties in this research work is the unacceptable computational burden due to the uncertainty of wind energy. To solve this problem, an ML-based model is trained to estimate the stability level for all preconceived fault scenarios rapidly. In addition, a set of IM-categorized probabilistic transient stability constraints (PTSCs) are constructed, which enables operators to set flexible stability requirements for the system. A method to convert the PTSCs into a set of linear inequality constraints is also explored. Finally, a computationally efficient dispatching framework considering the economic operation and stability of the system is proposed.

1.4 Organization of the Thesis

There are five chapters in this thesis. The main topics of each chapter are as follows:

Chapter 1 introduces the fundamental concepts of power system transient stability. Brief introductions to stability prediction techniques, preventive dispatch approaches, and application of ML in power systems are also discussed. The objective of the research is also presented in this chapter.

Chapter 2 develops a novel stability index (*SI*). Inspired by EEAC-related studies, the developed index calculates the transient stability margin of power systems considering wind power dynamics. For this purpose, WPPs in this study are represented as a set of variable admittances, and the impacts of WPPs on the electromagnetic power of SGs are analyzed. Then the calculation of the variable admittances is introduced. Finally, a novel *SI* considering the dynamics of SGs and WPPs is put forward. The concept of instability mode (IM) will also be introduced in this chapter.

Chapter 3 elaborates the framework of transient stability prediction. First, an *SI* vector is proposed, which is built based on the *SI* developed in chapter 2. The *SI* vector is selected as the feature and applied to an ML-based classifier algorithm for transient stability prediction. Specifically, the construction of the *SI* vector, the structure of the framework, the database generation, and training and testing of the proposed framework are expounded in this chapter. The proposed method is tested on an IEEE 68- and 300- bus system, and its performances are compared with previous methods. In addition, the sensitivity of the proposed framework is analyzed with respect to practical problems.

Chapter 4 puts forward an hour-ahead probabilistic transient stability-constrained power dispatching method for power systems under a high inclusion of wind power. In this chapter, the difficulties in this topic are analyzed, followed by the solving ideas. First, an ML-based model is trained to predict the critical clearing time (CCT) and instability mode (IM) for all preconceived fault scenarios. The training and testing process of the model is also illustrated. In addition, a set of IM-categorized probabilistic transient stability constraints (PTSCs) are constructed. Based on the predictions, the system operation plan is assessed with respect to the PTSCs. Next, the method to transform the implicit PTSCs into explicit dispatching constraints is expounded. By this means, the dispatch is rescheduled to ensure the required system stability is met at an economical operating cost. The proposed approach is validated on IEEE 68- and 300-bus test systems with a high level of wind power penetration, and compared to a newly developed method.

Finally, the conclusions and the suggestions for future works are presented in Chapter 5.

2 A Novel Transient Stability Index

2.1 Introduction

The development of the ML techniques makes online transient stability prediction using real-time synchronized data obtained by PMU possible [17], [56], [60], [66]. Generally, ML-based techniques require a large set of labelled data obtained by offline simulations for model training, during which the diverse scenarios that can take place in power systems are enumerated. Notably, these prediction methods have advantages in terms of calculation speed and are more adaptable to bulk power systems in this respect.

However, most of the existing ML applications in this area directly borrow ML algorithms and use the data directly obtained from PMU to perform stability prediction. There is a lack of innovation in feature selection and problem modelling. In the presence of the high penetration of wind powers, these prediction approaches may be confronted with severe dilemmas, as explored below.

First, the output of wind power plants (WPPs) can vary both temporally and spatially [65], which exponentially increases the possible system pre-fault operation scenarios and imposes multisource uncertainties to the overall system dynamics [58]. Consequently, extensive training data may be required to cope with the combination of all possible uncertainties in power systems, and as such, the computation time explodes [58]. Handling a high volume of data entails more sophisticated prediction models and a larger number of features. In addition, it may boost the dimensionality of the input space and further increases the chance of overfitting and affects the overall performance [104]. However, an algorithm that demands massive offline data restricts the updating process of the prediction models. Consequently, the generalization ability of such prediction models is restricted, and the deficiencies noted may impede the application of ML-based methods in real-life projects.

In addition, exploring informative and discriminative features is crucial for ML-based methods to reach reliable prediction models. As uncertainties of the system increase, existing features such as bus voltages [17], [56], [60], [66], which are obtained via PMU measurements, may no longer be so useful. A few post-fault samples of these raw data may be unable to intuitively reflect the effects of dispersed WPPs and their uncertainties on system dynamics, as several possible combinations of uncertainties may lead to similar values. Interpreting these raw data into derived features that better represent the underlying problem can help improve model accuracy on test data.

Moreover, most of the ML-based studies mentioned above utilize post-fault data obtained after fault clearance for stability prediction, which postpones the decision-making time. Considering new advancements in PMU development, measurement data are now reliable and consistent during transients [58]. Therefore, the reduction of these data might be of interest when considering the importance of quick action against instability.

In fact, by including the physical characteristics of the power system into the ML algorithms, the reliability and accuracy of the prediction can be increased. To this end, a novel transient stability index (*SI*) is developed, in which WPPs are represented as variable admittances to be integrated into an equivalent network model during the transients. To calculate the potential and kinetic energies of a power system without integral operation, a short-term terminal voltage recovery trajectory is derived for each WPP. In this way, the effects of WPPs on the kinetic and potential energies of a system are calculated after disturbances. The derivation and validation of the *SI* is introduced in this chapter. It is worth noting that the *SI* will be extended to an *SI* vector that will be used as a feature for stability prediction in Chapter 3.

2.2 Extended Equal Area Criterion (EEAC)

The novel *SI* algorithm is inspired by the EEAC and further explored for power systems with WPPs. EEAC is one of the multiple TEF-related transient stability assessment methods. Unlike time-domain simulations (TDSs), these methods can rapidly estimate the stability margin of a conventional power system under a series of preconceived faults. Therefore, they are prevailing in fast contingency screening and comparing the relative stability of a system under various contingencies. These methods have been widely discussed since 1980s and have played an important role in transient stability assessment [28]–[42], [105], [106].

The EEAC is developed for a system with n synchronous generators (SGs) [32], [106]. In case of a contingency, the SGs are grouped into two complementary sets by IM identification: the critical SGs that cause loss of synchronism and the remaining SGs, denoted as Ω^{C} and Ω^{R}, respectively. The system is then reduced at the generator internal nodes to a network equivalent, as shown in Figure 2.1 (a), and the SGs in Ω^{C} and Ω^{R} are modelled by two equivalent machines so that each represents the dynamics of the corresponding machines within a partial center of angles. The system is further reduced to a one-machine-infinite-bus (OMIB) system, as shown in Figure 2.1 (b). The mapping of the equivalent OMIB under such clustering is given by [32], [106]:

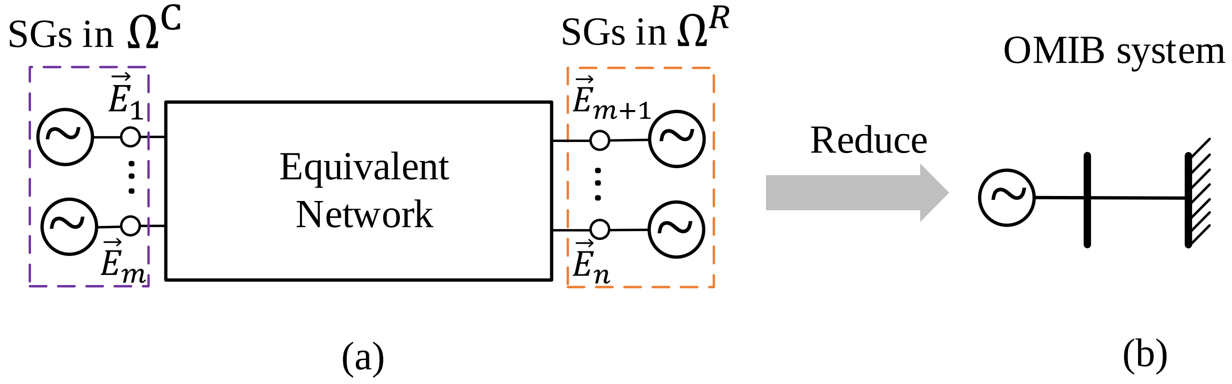

Figure 2.1: An equivalent network of an n-machine power system during a loss of synchronism.

$$\delta = \delta_C - \delta_R \tag{2.1}$$

$$\frac{d\delta}{dt} = \omega - \omega_0 \tag{2.2}$$

$$\frac{M}{\omega_0}\frac{d(\omega - \omega_0)}{dt} = P_{mech} - P \tag{2.3}$$

$$\delta_C = \frac{1}{M_C}\sum_{i\in\Omega^{\mathrm{C}}} \delta_i\, M_i \tag{2.4}$$

$$\delta_R = \frac{1}{M_R}\sum_{j\in\Omega^{\mathrm{R}}} \delta_j\, M_j \tag{2.5}$$

$$M = \frac{M_C M_R}{M_T} \tag{2.6}$$

$$M_T = M_C + M_R \tag{2.7}$$

$$M_C = \sum_{i \in \Omega^{\mathrm{C}}} M_i \tag{2.8}$$

$$M_R = \sum_{j \in \Omega^{\mathrm{R}}} M_j \tag{2.9}$$

$$P_{mech} = \frac{1}{M_T}\left(M_R \sum_{i \in \Omega^{\mathrm{C}}} P_{mech,i} - M_C \sum_{j \in \Omega^{\mathrm{R}}} P_{mech,j} \right) \tag{2.10}$$

$$P = \frac{1}{M_T}\left(M_R \sum_{i \in \Omega^{\mathrm{C}}} P_i - M_C \sum_{j \in \Omega^{\mathrm{R}}} P_j \right) \tag{2.11}$$

where

δ_i: rotor angle of SG$_i$,

M_i: inertia constant of SG$_i$,

P_i: electric power of SG$_i$,

$P_{mech,i}$: mechanical power of SG$_i$,

δ_C: rotor angle of the equivalent SG in Ω^{C},

M_C: inertia constant of the equivalent SG in Ω^{C},

δ_R: rotor angle of the equivalent SG in Ω^{R},

M_R: inertia constant of the equivalent SG in Ω^{R},

δ: rotor angle of the equivalent OMIB system,

M: inertia constant of the equivalent OMIB system,

P: electric power of the equivalent OMIB system,

P_{mech}: mechanical power of the equivalent OMIB system,

ω: angular speed of rotor,

ω_0: synchronous speed.

With an additional simplification for machines within Ω^{C} and Ω^{R} [32]:

$$\delta_i \approx \delta_C \mid \forall i \in \Omega^{\mathrm{C}}, \qquad \delta_j \approx \delta_R \mid \forall j \in \Omega^{\mathrm{R}} \tag{2.12}$$

The active power output of SG_i can be expressed by [106]:

$$P_i = \mathrm{Re}\left(\vec{E}_i \vec{I}_i^*\right) = E_i \boldsymbol{\varepsilon}_i^{\mathrm{T}} \mathrm{Re}(\boldsymbol{Y}_{\mathrm{CC}}) \boldsymbol{E}_{\mathrm{C}} + E_i \boldsymbol{\varepsilon}_i^{\mathrm{T}} [\sin\delta \, \mathrm{Im}(\boldsymbol{Y}_{CR}) + \cos\delta \, \mathrm{Re}(\boldsymbol{Y}_{CR})] \boldsymbol{E}_R \tag{2.13}$$

where

$\vec{E}_i$: complex voltage of the internal node of SG_i,

$\vec{I}_i$: complex current injections at the internal node of SG_i,

E_i: magnitude of $\vec{E}_i$,

superscript $*$: conjugate transpose,

$\boldsymbol{\varepsilon}_i$: standard basis in $\mathbb{R}^{|\Omega^{\mathrm{C}}|}$,

$\boldsymbol{Y}_{CC}$: admittance matrix of nodes in Ω^{C},

$\boldsymbol{Y}_{CR}$: mutual admittance matrix between nodes in Ω^{C} and Ω^{R},

$\vec{\boldsymbol{E}}_C$: complex voltage column vector of internal nodes of SGs in Ω^{C},

$\vec{\boldsymbol{E}}_R$: complex voltage column vector of internal nodes of SGs in Ω^{R},

$\boldsymbol{E}_C$: column vector that includes the magnitudes of each element in $\vec{\boldsymbol{E}}_C$,

$\boldsymbol{E}_R$: column vector that includes the magnitudes of each element in $\vec{\boldsymbol{E}}_R$,

Note both $\boldsymbol{Y}_{CC}$ and $\boldsymbol{Y}_{CR}$ are extracted from the equivalent network shown in Figure 2.1 (a). Likewise, P_j can be expressed similarly. For simplicity, $\boldsymbol{E}_C$, $\boldsymbol{E}_R$, and P_{mech} are assumed to maintain their steady-state values during transients [32]. Thus, P in (2.11) can be obtained by (2.14)–(2.17) [106]:

$$P = P_{\mathrm{const}} + P_{max} \sin(\delta - \gamma) \tag{2.14}$$

$$P_{\mathrm{const}} = \frac{M_R}{M_T} \boldsymbol{E}_C{}^{\mathrm{T}} \mathrm{Re}(\boldsymbol{Y}_{\mathrm{CC}}) \boldsymbol{E}_C + \frac{M_C}{M_T} \boldsymbol{E}_R{}^{\mathrm{T}} \mathrm{Re}(\boldsymbol{Y}_{RR}) \boldsymbol{E}_R \tag{2.15}$$

$$P_{max} = \sqrt{\left(\frac{M_R - M_C}{M_T} \boldsymbol{E}_C{}^{\mathrm{T}} \mathrm{Re}(\boldsymbol{Y}_{CR}) \boldsymbol{E}_R\right)^2 + \left(\boldsymbol{E}_R{}^{\mathrm{T}} \mathrm{Im}(\boldsymbol{Y}_{RC}) \boldsymbol{E}_C\right)^2} \tag{2.16}$$

$$\gamma = -\arctan \frac{\frac{M_R - M_C}{M_T} \boldsymbol{E}_C{}^{\mathrm{T}} \mathrm{Re}(\,\boldsymbol{Y}_{CR}) \boldsymbol{E}_R}{\boldsymbol{E}_R{}^{\mathrm{T}} \mathrm{Im}(\boldsymbol{Y}_{RC}) \boldsymbol{E}_C} \tag{2.17}$$

where

P_{const}, P_{max} and γ: constants, and the derivations are introduced in [106],

$\boldsymbol{Y}_{RR}$: admittance matrix of nodes in Ω^{R},

$\boldsymbol{Y}_{RC}$: mutual admittance matrix between nodes in Ω^{R} and Ω^{C}.

Then, the "accelerating area" and "decelerating area" of the equivalent OMIB system, which respectively correspond to the kinetic and potential energies of the system, are calculated by:

$$\begin{aligned} A_{acc} &= \int_{\delta(t_{\mathrm{f}})}^{\delta(t_{\mathrm{cl}})} (P_{mech} - P_{\mathcal{D}}) d\delta \\ &= \left(P_{mech} - P_{\mathrm{const}_{\mathcal{D}}}\right)(\delta(t_{\mathrm{cl}}) - \delta(t_{\mathrm{f}})) + P_{\mathrm{max}_{\mathcal{D}}}(\cos(\delta(t_{\mathrm{cl}}) - \gamma_D) - \cos(\delta(t_{\mathrm{cl}}) - \gamma_{\mathcal{D}})) \end{aligned} \tag{2.18}$$

$$\begin{aligned} A_{dec} &= \int_{\delta(t_{cl})}^{\delta(t_u)} (P_{\mathcal{S}} - P_{mech}) d\delta \\ &= \left(P_{\mathrm{const}_{\mathcal{S}}} - P_{mech}\right)\left(\delta(t_u) - \delta(t_{\mathrm{cl}})\right) + P_{\mathrm{max}_{\mathcal{S}}} \cos(\delta(t_{\mathrm{cl}}) - \gamma_{\mathcal{S}}) - P_{\mathrm{max}_{\mathcal{S}}} \cos(\delta(t_{\mathrm{u}}) - \gamma_{\mathcal{S}}) \end{aligned} \tag{2.19}$$

where

t_{f}: fault inception time,

t_{cl}: fault clearance time,

t_{u}: time instant when the system reaches the unstable equilibrium point.

Subscripts $\mathcal{D}$ and $\mathcal{S}$ represent the system electric quantities during the fault and after the fault clearance, respectively. In this case, the stability of the system can be judged by comparing the difference between kinetic and potential energy against a predefined threshold value.

It is worth noting that these stability assessment methods [28]–[42], including EEAC, were initially developed for rapid contingency screening instead of transient stability prediction. With the availability of the PMUs, some of these methods have great potential to play a key role in stability prediction. For example, in previous studies, $\delta(t_{\mathrm{cl}})$ used in (2.18) and (2.19) was calculated using algorithms like higher-order Taylor series. With the advancements in PMU-relate techniques, measurement data are now reliable and consistent during transients. Therefore, real time rotor angles of the equivalent OMIB system, including $\delta(t_{\mathrm{f}})$ and $\delta(t_{\mathrm{cl}})$, can be obtained or estimated from PMU data. Beyond these, $\delta(t_{\mathrm{u}})$ can be calculated immediately based on system information at $t_{\mathrm{cl}+}$, as introduced in [106]. As a result, (2.18) and (2.19) can be calculated immediately after fault clearance without integral operation, thus providing valuable information for stability prediction. In the next section, the study will be further explored for power systems with WPPs.

2.3 Derivation of a Novel Stability Index

To address the challenges faced by *SI* calculations caused by WPP dynamics, a novel algorithm inspired by the EEAC for calculating *SI* is introduced in this section. First, the calculation of a set of virtual variable admittances that reshape the system and model the dynamic behavior of WPPs is introduced in Section 2.3.1. Impacts of WPPs on the electromagnetic power of SGs are then analyzed. Next, the short-term terminal voltage recovery of WPPs is derived in Section 2.3.2, and, consequently, a novel *SI* considering the dynamics of WPPs is put forward.

2.3.1 Equivalence of WPPs

The principle of variable admittances is used to eliminate WPP nodes while retaining their transient effects on SGs. Consider a network with two SGs and one WPP, as shown in Figure 2.2, which is reduced at the SG internal nodes and point of intersection (POI) of the WPP in the equivalent network model. Because $\vec{I}_1$ and $\vec{I}_2$ should be consistent with the corresponding values after WPP elimination, the equivalent admittances Y_1' and Y_2' are obtained as:

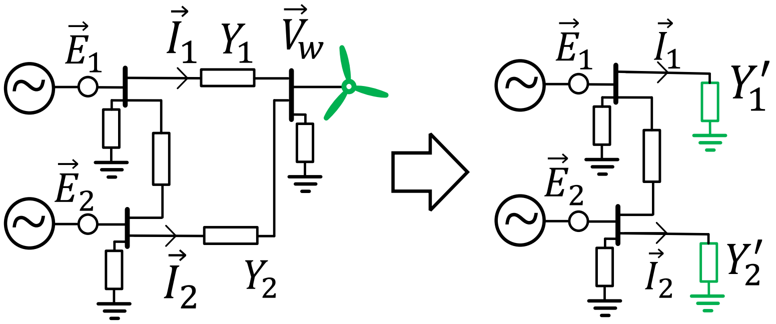

Figure 2.2: The principle of variable admittances.

$$Y_1' = \left(1 - \frac{\vec{V}_w}{\vec{E}_1}\right) Y_1 \tag{2.20}$$

$$Y_2' = \left(1 - \frac{\vec{V}_w}{\vec{E}_2}\right) Y_2 \tag{2.21}$$

Similarly, consider a system with n SGs and n' WPPs; an electrical equivalent of the system is constructed, as shown in Figure 2.3 (a). Generally, the wind generators (WGs) in WPPs are not synchronously connected to the grid, and thus do not face rotor angle instability. However, the power output from these WPPs during transient conditions is affected by network voltage, which in turn affects the transient stability of the system [58]. In dynamic coherency determination studies [107], [108], each non-SG bus, including POIs [108], is appended to an associated SG coherent group to form a coherent area following a disturbance. This is determined by the rate of change of voltage angle or frequency-deviation signals of each bus [108]. Accordingly, the POIs with connected WPPs are divided into two complementary clusters—the critical subset Ω^{G} and the remaining subset Ω^{H}, which are appended to the Ω^{C} and Ω^{R} groups, respectively—as shown in Figure 2.3 (a).

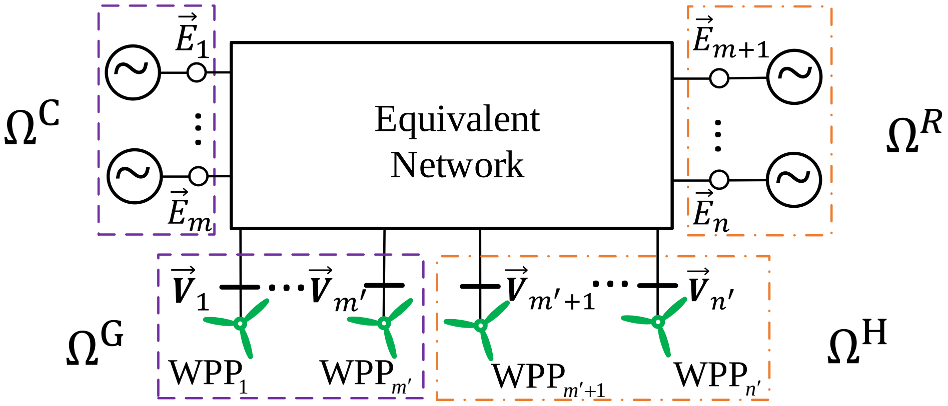

(a)

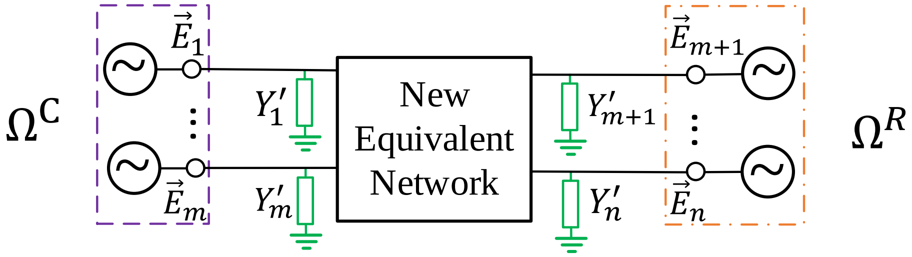

(b)

Figure 2.3: Equivalence a power system incorporating WPPs.

The equivalent network shown in Figure 2.3 (a) is given by:

$$\begin{bmatrix}\vec{\boldsymbol{I}}_C\\ \vec{\boldsymbol{I}}_G\\ \vec{\boldsymbol{I}}_R\\ \vec{\boldsymbol{I}}_H\end{bmatrix}=\begin{bmatrix}\boldsymbol{Y}_{CC} & \boldsymbol{Y}_{CG} & \boldsymbol{Y}_{CR} & \boldsymbol{Y}_{CH}\\ \boldsymbol{Y}_{GC} & \boldsymbol{Y}_{GG} & \boldsymbol{Y}_{GR} & \boldsymbol{Y}_{GH}\\ \boldsymbol{Y}_{RC} & \boldsymbol{Y}_{RG} & \boldsymbol{Y}_{RR} & \boldsymbol{Y}_{RH}\\ \boldsymbol{Y}_{HC} & \boldsymbol{Y}_{HG} & \boldsymbol{Y}_{HR} & \boldsymbol{Y}_{HH}\end{bmatrix}\begin{bmatrix}\vec{\boldsymbol{E}}_C\\ \vec{\boldsymbol{V}}_G\\ \vec{\boldsymbol{E}}_R\\ \vec{\boldsymbol{V}}_H\end{bmatrix} \tag{2.22}$$

where

$\vec{\boldsymbol{I}}_C$: complex current column vector of SG internal nodes in Ω^{C},

$\vec{\boldsymbol{I}}_R$: complex current injection column vector of SG internal nodes in Ω^{R},

$\vec{\boldsymbol{V}}_G$: complex voltage column vector of POIs of WPPs in Ω^{G},

$\vec{\boldsymbol{I}}_G$: complex current injection column vector of POIs of WPPs in Ω^{G},

$\vec{\boldsymbol{V}}_H$: complex voltage column vector of POIs of WPPs in and Ω^{H},

$\vec{\boldsymbol{I}}_H$: complex current injection column vector of POIs of WPPs in Ω^{H},

$\boldsymbol{Y}_{CH}$ and $\boldsymbol{Y}_{HC}$: the mutual admittance matrix between nodes in sets Ω^{C} and Ω^{H};

$\boldsymbol{Y}_{GG}$: admittance matrix of nodes in Ω^{G},

$\boldsymbol{Y}_{GC}$ and $\boldsymbol{Y}_{CG}$: mutual admittance matrix between nodes in sets Ω^{G} and Ω^{C},

$\boldsymbol{Y}_{GR}$ and $\boldsymbol{Y}_{RG}$: mutual admittance matrix between nodes in sets Ω^{G} and Ω^{R},

$\boldsymbol{Y}_{HH}$: admittance matrix of WPPs nodes in Ω^{H},

$\boldsymbol{Y}_{HG}$ and $\boldsymbol{Y}_{GH}$: mutual admittance matrix between nodes in sets Ω^{H} and Ω^{G};

$\boldsymbol{Y}_{HR}$ and $\boldsymbol{Y}_{RH}$: mutual admittance matrix between nodes in sets Ω^{R} and Ω^{H}.

Similar to Figure 2.2, a series of variable admittances that act as additional self-impedance of each internal node can be built to simulate the transient behavior of WPPs, as shown in Figure 2.3 (b), during which the network in Figure 2.3 (a) is first reduced at the generator internal nodes and POIs, and the principle of variable admittance introduced in Figure 2.2 is then applied. Thus, the equivalent network of Figure 2.3 (a) is rebuilt; the WPP nodes are eliminated and the connections between each SG remain the same. The current-injection model of the system in Figure 2.3 (b) is given by:

$$\begin{bmatrix}\vec{\boldsymbol{I}}_C\\ \vec{\boldsymbol{I}}_R\end{bmatrix}=\begin{bmatrix}\boldsymbol{Y}'_{CC} & \boldsymbol{Y}_{CR}\\ \boldsymbol{Y}_{RC} & \boldsymbol{Y}'_{RR}\end{bmatrix}\begin{bmatrix}\vec{\boldsymbol{E}}_C\\ \vec{\boldsymbol{E}}_R\end{bmatrix} \tag{2.23}$$

where $\boldsymbol{Y}'_{CC}$ and $\boldsymbol{Y}'_{RR}$ are the admittance matrices of nodes in Ω^{C} and in Ω^{R} after eliminating WPP nodes from the equivalent OMIB system, respectively, and they are calculated by:

$$\boldsymbol{Y}'_{CC} = \boldsymbol{Y}_{CC} + \mathrm{diag}[Y'_1, \ldots, Y'_m] \tag{2.24}$$

$$\boldsymbol{Y}'_{RR} = \boldsymbol{Y}_{RR} + \mathrm{diag}[Y'_{m+1}, \ldots, Y'_n] \tag{2.25}$$

and $Y'_1, \ldots, Y'_m, Y'_{m+1}, \ldots, Y'_n$ are variable admittances. Similar to (2.20)–(2.21), these admittances can be calculated by:

$$Y'_i = \sum_{g \in \Omega^{\mathrm{G}}} \left[\left(1 - \frac{\vec{V}_g}{\vec{E}_i} \right) Y_{ig} \right] + \sum_{h \in \Omega^{\mathrm{H}}} \left[\left(1 - \frac{\vec{V}_h}{\vec{E}_i} \right) Y_{ih} \right], \quad \mathrm{i} = 1, 2 \ldots, n \in (\Omega^{\mathrm{C}} \cup \Omega^{\mathrm{R}}) \tag{2.26}$$

where

Y_{ig}: mutual admittance between i and g,

Y_{ih}: mutual admittance between i and h.

It can be seen from (2.26) that the variable admittances can reflect the effect of uncertainties of wind power; as the voltages of SG internal nodes and POIs fluctuate with wind power generation, the admittances change accordingly.

Therefore, during fault-free conditions, the values of the variable admittances vary at all times due to the wind speed uncertainties. During transients, the wind speeds of each WPP are assumed to remain constant [109] (assuming they start when a fault occurs t_{f} and end at 1–5s after fault clearance t_{cl}); thus, the values these variable admittances are determined by the pre-fault conditions and the transient process of the system, including the fault-related change of system states, variables, and topology, the controls on WPPs, etc.

After the inclusion of the variable admittances shown in Figure 2.3 (b), P_i in (2.13) and P in (2.14)−(2.17) are re-written in which $\boldsymbol{Y}_{CC}$, $\boldsymbol{Y}_{RR}$ are replaced by $\boldsymbol{Y}'_{CC}$ and $\boldsymbol{Y}'_{RR}$, respectively. Notably, P is expressed by:

$$P = P_{\mathrm{variable}} + P_{max} \sin(\delta - \gamma) \tag{2.27}$$

$$P_{\mathrm{variable}} = \frac{M_R}{M_T} \boldsymbol{E}_C{}^{\mathrm{T}} \mathrm{Re}(\boldsymbol{Y}'_{CC}) \boldsymbol{E}_C + \frac{M_C}{M_T} \boldsymbol{E}_R{}^{\mathrm{T}} \mathrm{Re}(\boldsymbol{Y}'_{RR}) \boldsymbol{E}_R \tag{2.28}$$

$$P_{max} = \sqrt{(\frac{M_R - M_C}{M_T}\boldsymbol{E}_C{}^{\mathrm{T}}\mathrm{Re}(\,\boldsymbol{Y}_{CR})\boldsymbol{E}_R)^2 + (\boldsymbol{E}_R{}^{\mathrm{T}}\mathrm{Im}(\boldsymbol{Y}_{RC})\boldsymbol{E}_C)^2} \tag{2.29}$$

$$\gamma = -\arctan\frac{\frac{M_R - M_C}{M_T}\boldsymbol{E}_C{}^{\mathrm{T}}\mathrm{Re}(\,\boldsymbol{Y}_{CR})\boldsymbol{E}_R}{\boldsymbol{E}_R{}^{\mathrm{T}}\mathrm{Im}(\boldsymbol{Y}_{RC})\boldsymbol{E}_C} \tag{2.30}$$

where P_{variable} is the counterpart of P_{const} in (2.15), while the P_{variable} is a variable here due to the variability of $\boldsymbol{Y}'_{CC}$ and $\boldsymbol{Y}'_{RR}$.

From (2.24)–(2.25), $\boldsymbol{Y}'_{CC}$ and $\boldsymbol{Y}'_{RR}$ are composed of self and mutual admittances of the SGs and the variable admittances; hence, for the WPP-integrated power system, the electromagnetic power of each SG includes the amount exchanged among the SGs as well as among the SGs and the WPPs. Similar to (2.12), because the dynamics of the voltage angles of buses within one coherent group are similar [108], an assumption is made for the unstable cases: during the period after t_{cl}, it has,

$$\theta_g \approx \delta_C \mid \forall g \in \Omega^{\mathrm{G}}\,, \qquad \theta_h \approx \delta_R \mid \forall h \in \Omega^{\mathrm{H}} \tag{2.31}$$

where θ_g and θ_h represent the voltage angle of POIs of g and h, respectively; thus, (2.26) can be further simplified. Therefore, the variables left in P are δ and $\boldsymbol{V}$, where $\boldsymbol{V} = \begin{bmatrix}\boldsymbol{V}_G \\ \boldsymbol{V}_H\end{bmatrix}$, and $\boldsymbol{V}_G$ and $\boldsymbol{V}_H$ are matrices that include the magnitudes of each element in $\vec{\boldsymbol{V}}_G$ and $\vec{\boldsymbol{V}}_H$, respectively. Because δ is the integration variable of the integration of (2.18)–(2.19), if the δ–$\boldsymbol{V}$ relationship of the post-fault function is obtained, then the antiderivative of (2.18) and (2.19) can be derived, which leads to the calculation of kinetic and potential energies without integral operation.

2.3.2 Post-Fault Recovery of the Voltages of the POIs

During the fault period, t_{f} to t_{cl}, the dip value of $\boldsymbol{V}$ is obtainable from PMUs and can be directly used for kinetic energy calculation. Thereby, the remaining challenge to calculate potential energy is to derive the potential $\boldsymbol{V}$ - δ relationship during t_{cl} to t_u, defined as t_{cu}. Because the WPP control strategy affects the $\boldsymbol{V}$ - δ relationship in t_{cu}, calculations are conducted with respect to the control scheme.

In this study, all WGs are considered to be doubly-fed induction generators (DFIGs) due to their popularity among current WPPs. All WGs are assumed to have fault ride-through capability and remain connected during faults, and are involved in Volt/VAR control to regulate the voltage of their respective POIs; this is the most prevalent output control in recent North American and European WPPs [109]. The methodology introduced below can be modified for application to DFIGs under other output control situations.

Faster-acting local controls implemented in the WG converters can provide a dynamic response to voltage dips. The introduction of a generator/converter model of DFIG that regulates real and reactive power output is reported in [25]. Denote V_w as the voltage magnitude of the POI of the WPP_w. During the V_w drop period, the delivery of reactive power of this WPP, Q_w, is given priority by the Volt/VAR control. In other words, the active power P_w remains limited while Q_w increases to support V_w recovery. This control mode is generally triggered from t_f and continues after fault clearance if $V_w(t_{\mathrm{cl}+})$ fails to recover immediately; Q_w then increases and remains at its maximum output until V_w recovers. This process is illustrated in Figure 2.4, in which the WPP is in rated output (100 MW) before the contingency. Similar simulation results are also reported in [110] and [111].

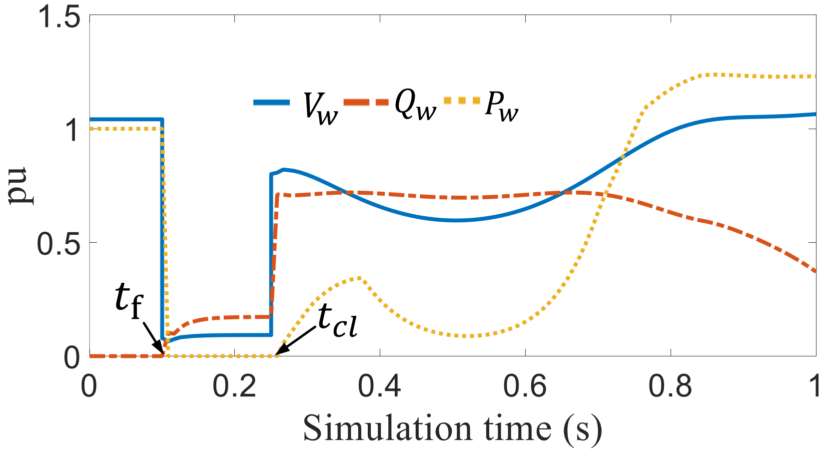

Figure 2.4: Real power, reactive power, and terminal voltage of a Volt/VAR controlled WPP during and after a fault.

The control strategy of WGs affects their regulated voltages $\boldsymbol{V}$ and reactive power outputs $\boldsymbol{Q}$, which consequently influence the dynamics of the system. In light of this structure, a $\boldsymbol{V}$ - δ

relationship can be obtained by a derivative operator by having an idea about the transient characteristics of $\boldsymbol{Q}$. To this end, denote:

$$V_w(t_{\mathrm{cu}}) = V_w(t_{\mathrm{f-}}) \quad | \ \forall\, w \in (\Omega^{\mathrm{G}} \cup \Omega^{\mathrm{H}}) \text{ and } V_w(t_{\mathrm{cl+}}) \geq \varphi V_w(t_{\mathrm{f-}}) \tag{2.32}$$

where $V_w(t_{\mathrm{cu}})$ represents V_w during t_{cu}, $V_w(t_{\mathrm{f-}})$ is equal to V_w at steady state, and φ is a threshold ratio of $V_w(t_{\mathrm{cl+}})$ to $V_w(t_{\mathrm{f-}})$. Equation (2.32) means that V_w is considered recovered immediately after fault clearance if $V_w(t_{\mathrm{cl+}})$ is close to its pre-fault value. Specifically, φ is set to 0.9 because this is the typical value to trigger the low voltage condition of Volt/VAR control in WPPs.

Alternatively, for those $V_w(t_{\mathrm{cl+}})$ that fail to reach $\alpha V_w(t_{\mathrm{f-}})$, according to the Volt/VAR control in DFIGs, the corresponding WPP would increase its reactive power output and remain at its maximum limitation until the voltage is restored. Hence, during t_{cu}, the reactive outputs of those WPPs can be considered as:

$$Q_w = \overline{Q}_w \quad | \ \forall\ w \in (\Omega^{\mathrm{G}} \cup \Omega^{\mathrm{H}}) \text{ and } V_w(t_{\mathrm{cl+}}) < \varphi V_w(t_{\mathrm{f-}}) \tag{2.33}$$

where $\bar{Q}_w$ is the maximum reactive output of the wth WPP, which is considered as a constant and determined by the controllers of the WGs in the WPP [109].

The reactive power outputs of each WPP are constructed by:

$$\boldsymbol{Q} = \left[\boldsymbol{Q}_G^{\mathrm{T}} \ \ \boldsymbol{Q}_H^{\mathrm{T}}\right]^{\mathrm{T}} \tag{2.34}$$

where $\boldsymbol{Q}_G$ and $\boldsymbol{Q}_H$ represent reactive power injection column vectors of WPPs of sets Ω^{G} and Ω^{H}, respectively. Given (2.22), (2.26) and (2.33), $\boldsymbol{Q}_G$ can be derived as (2.35), where ⊗ is pointwise multiplication; and $\boldsymbol{Q}_H$ is expressed in a similar way.

$$\boldsymbol{Q}_G = \mathrm{Im}\left(\vec{\boldsymbol{V}}_G \otimes \vec{\boldsymbol{I}}_G^*\right) = -\boldsymbol{V}_G \otimes \begin{pmatrix} \mathrm{Im}(\boldsymbol{Y}_{GG})\boldsymbol{V}_G + \cos\delta\,(\mathrm{Im}(\boldsymbol{Y}_{GH})\boldsymbol{V}_H + \mathrm{Im}(\boldsymbol{Y}_{GR})\boldsymbol{E}_R) \\ +\mathrm{Im}(\,\boldsymbol{Y}_{GC})\boldsymbol{E}_C - \sin\delta(\mathrm{Re}(\boldsymbol{Y}_{GH})\boldsymbol{V}_H + \mathrm{Re}(\boldsymbol{Y}_{GR})\boldsymbol{E}_R) \end{pmatrix} \tag{2.35}$$

It can be seen from (2.35) that $\boldsymbol{Q}$ is functions of $\boldsymbol{V}$ and δ.

From (2.32), V_w can be considered a constant value after t_{c} if $V_w(t_{\mathrm{cl}+}) \geq \varphi V_w(t_{\mathrm{f}-})$; so, attention is only focus on those $\{V_w, Q_w \mid \forall\ w \in (\Omega^{\mathrm{G}} \cup \Omega^{\mathrm{H}})$ and $V_w(t_{\mathrm{cl}+}) < \varphi V_w(t_{\mathrm{f}-})\}$ for the derivation of the $\boldsymbol{V}$ - δ relationship during t_{cu}. These voltages and reactive are constructed by:

$$\boldsymbol{V}' = [V_1 \cdots V_w \cdots V_{n'}]^{\mathrm{T}} \qquad \mid \forall\, w \in (\Omega^{\mathrm{G}} \cup \Omega^{\mathrm{H}}) \text{ and } V_w(t_{\mathrm{cl}+}) < \varphi V_w(t_{\mathrm{f}-}) \tag{2.36}$$

$$\boldsymbol{Q}'(\boldsymbol{V}, \delta) = [Q_1 \cdots Q_w \cdots Q_{n'}]^{\mathrm{T}} \quad \mid \forall\, w \in (\Omega^{\mathrm{G}} \cup \Omega^{\mathrm{H}}) \text{ and } V_w(t_{\mathrm{cl}+}) < \varphi V_w(t_{\mathrm{f}-}) \tag{2.37}$$

During t_{cu}, (2.32) shows that:

$$\Delta V_w = 0 \quad |\forall\, w \in G \cup H \quad \text{and} \quad V_w(t_{\mathrm{cl}+}) \geq \varphi V_w(t_{\mathrm{f}-}) \tag{2.38}$$

and ,thus, during t_{cu}, the $\boldsymbol{Q}'$ in (2.37) can be re-written as $\boldsymbol{Q}'(\boldsymbol{V}', \delta)$, where

$$\boldsymbol{Q}'(\boldsymbol{V}', \delta) = [\bar{Q}_1 \cdots \bar{Q}_w \cdots \bar{Q}_{n'}]^{\mathrm{T}} \mid \forall\, w \in (\Omega^{\mathrm{G}} \cup \Omega^{\mathrm{H}}) \text{ and } V_w(t_{\mathrm{cl}+}) < \varphi V_w(t_{\mathrm{f}-}) \tag{2.39}$$

Further, (2.33) shows that $\boldsymbol{Q}'$ in (2.36) is a constant column vector during t_{cu} and, thus, ignoring higher order terms during t_{cu} leads to:

$$\left[\frac{\partial \boldsymbol{Q}'(\boldsymbol{V}', \delta)}{\partial(\boldsymbol{V}', \delta)}\right]\Bigg|_{\boldsymbol{V}'=\boldsymbol{V}'(t_{\mathrm{cl}+}),\ \ \delta=\delta(t_{\mathrm{cl}})} \begin{bmatrix} \Delta \boldsymbol{V}' \\ \Delta\delta \end{bmatrix} = \boldsymbol{0} \tag{2.40}$$

where $\left[\frac{\partial \boldsymbol{Q}'(\boldsymbol{V}', \delta)}{\partial(\boldsymbol{V}', \delta)}\right]$ is a Jacobian matrix. Thus, from (2.40), a linear relation between $\boldsymbol{V}'$ and δ can be obtained by (2.41) during t_{cu}.

$$\Delta \boldsymbol{V}' = \boldsymbol{K}' \Delta\delta \tag{2.41}$$

where $\boldsymbol{K}'$ is linear coefficient between $\Delta \boldsymbol{V}'$ and $\Delta\delta$ during t_{cu}**:**

$$\boldsymbol{K}' = -\left[\frac{\partial(\boldsymbol{Q}')}{\partial(\boldsymbol{V}')}\right]^{-1} \left[\frac{\partial(\boldsymbol{Q}')}{\partial\delta}\right]\Bigg|_{\boldsymbol{V}'=\boldsymbol{V}'(t_{\mathrm{cl}+}),\ \ \delta=\delta(t_{\mathrm{cl}})} \tag{2.42}$$

For generalization, $\boldsymbol{V}(t_{cu})$ can be written as:

$$\boldsymbol{V}(t_{cu}) = \left[\boldsymbol{V}_G^{\mathrm{T}}(t_{\mathrm{cl+}})\ \ \boldsymbol{V}_H^{\mathrm{T}}(t_{\mathrm{cl+}})\right]^{\mathrm{T}} + \left[\boldsymbol{K}_G^{\mathrm{T}}\ \ \boldsymbol{K}_H^{\mathrm{T}}\right]^{\mathrm{T}}(\delta - \delta_{\mathrm{cl}}) \tag{2.43}$$

where $\left[\boldsymbol{K}_G^{\mathrm{T}}\ \ \boldsymbol{K}_H^{\mathrm{T}}\right]^{\mathrm{T}}$ is the linear coefficient between $\Delta\boldsymbol{V}$ and $\Delta\delta$ during t_{cu}. In particular:

$$V_w(t_{\mathrm{cl+}})\ = V_w(t_{\mathrm{f-}}),\ K_w = 0 \quad |\ \forall\, w \in (\Omega^{\mathrm{G}} \cup \Omega^{\mathrm{H}}), V_w(t_{\mathrm{cl+}}) \geq \varphi V_w(t_{\mathrm{f-}}) \tag{2.44}$$

and other K_w in $\left[\boldsymbol{K}_G^{\mathrm{T}}\ \ \boldsymbol{K}_H^{\mathrm{T}}\right]^{\mathrm{T}}$ are calculated from (2.42). Relying on (2.42), the $\boldsymbol{V}$ - δ relationship is obtained. A novel *SI*, derived from that, is proposed next.

2.3.3 The Proposed *SI*

Given (2.14), (2.15), (2.24)–(2.31), and (2.43), the integrals in (2.45) and (2.46), which respectively correspond to the kinetic and potential energies of a system after fault clearance considering WPPs, can be obtained:

$$A_{acc} = \int_{\delta(t_{\mathrm{f}})}^{\delta(t_{\mathrm{cl}})}(P_{mech} - P_{\mathcal{D}}(\delta))d\delta = A_{acc1} + A_{acc2} \tag{2.45}$$

$$A_{dec} = \int_{\delta(t_{\mathrm{cl}})}^{\delta(t_{\mathrm{u}})}(P_{\mathcal{S}}(\delta) - P_{mech})d\delta = A_{dec1} + A_{dec2} \tag{2.46}$$

where

$$\begin{aligned} A_{acc1} = {} & \left(P_{mech} - P_{const_{\mathcal{D}}}\right)(\delta(t_{\mathrm{cl}}) - \delta(t_{\mathrm{f}})) \\ & + P_{\mathrm{max}_{\mathcal{D}}}(\cos(\delta(t_{\mathrm{cl}}) - \gamma_{\mathcal{D}}) - \cos(\delta(t_{\mathrm{cl}}) - \gamma_{\mathcal{D}})) \end{aligned} \tag{2.47}$$

$$A_{acc2} = \xi_1(\delta(t_{\mathrm{cl}}) - \delta(t_{\mathrm{f}})) + \xi_2(\sin\delta(t_{\mathrm{cl}}) - \sin\delta(t_{\mathrm{f}})) - \xi_3(\cos\delta(t_{\mathrm{cl}}) - \cos\delta(t_{\mathrm{f}})) \tag{2.48}$$

$$\begin{aligned} A_{dec1} = {} & \left(P_{const_{\mathcal{S}}} - P_{mech}\right)\left(\delta(t_u) - \delta(t_{\mathrm{cl}})\right) + P_{\mathrm{max}_{\mathcal{S}}}\cos(\delta(t_{\mathrm{cl}}) - \gamma_{\mathcal{S}}) \\ & - P_{\mathrm{max}_{\mathcal{S}}}\cos(\delta(t_{\mathrm{u}}) - \gamma_{\mathcal{S}}) \end{aligned} \tag{2.49}$$

$$\begin{aligned} A_{dec2} = {} & \eta_1\left(\delta(t_{\mathrm{u}}) - \delta(t_{\mathrm{cl}})\right) + \eta_2\left(\delta^2(t_{\mathrm{u}}) - \delta^2(t_{\mathrm{cl}})\right) \\ & + (\eta_3 + \eta_6)(\sin\delta(t_{\mathrm{u}}) - \sin\delta(t_{\mathrm{cl}})) \\ & + (\eta_4 + \eta_5)(\cos\delta(t_{\mathrm{u}}) - \cos\delta(t_{\mathrm{cl}})) \\ & + \eta_5(\delta(t_{\mathrm{u}})\sin\delta(t_{\mathrm{u}}) - \delta(t_{\mathrm{cl}})\sin\delta(t_{\mathrm{cl}})) \\ & - \eta_6(\delta(t_{\mathrm{u}})\cos\delta(t_{\mathrm{u}}) - \delta(t_{\mathrm{cl}})\cos\delta(t_{\mathrm{cl}})) \end{aligned} \tag{2.50}$$

where the subscripts $\mathcal{D}$ and $\mathcal{S}$, γ, P_{const}, P_{max} have been defined in Section 2.2; ξ_1— ξ_3 and η_1— η_6 in (2.48) and (2.50) are constants, with detailed equations given in Appendix A. The *SI*, which considers the dynamics of WPPs on the transient stability, is then given as:

$$SI = \frac{A_{dec} - A_{acc}}{A_{acc}} \tag{2.51}$$

To calculate ξ_1— ξ_3 and η_1— η_6, and subsequently (2.47)–(2.51), the following data are required:

(1) System admittance matrix at $t_{\mathrm{f}+}$ and $t_{\mathrm{cl}+}$,

(2) Rotor angles of each SG at t_{f} and t_{cl},

(3) Pre-fault internal voltage magnitudes of each SG, and

(4) Voltages of each POI at $t_{\mathrm{f}+}$ and $t_{\mathrm{cl}+}$.

In the studies conducted in this thesis, the required information in (1)–(4) is assumed to be obtainable from PMU measurements. In fact, the real-time system admittance is fairly available to operators, and PMU-based fault location detection is introduced in [112]−[114], and online event and fault type detection are reported in [115], [116]. These methods are determining factors to obtain values of (1). In addition, the pre-fault internal voltage of the SGs, the voltages of the POIs, and the rotor angles during and after the clearance of faults can be estimated from PMU measurements [51], [117]. Therefore, the *SI* can be calculated immediately after $t_{\mathrm{cl}+}$. Based on (2.51), the value of the *SI* correlates with the stability margin of the post-fault wind power-connected network.

2.4 Numerical Simulations

This section aims to assess the proposed *SI*. To this end, two assessment tests are carried out:

(1) the validity of the virtual variable admittances developed in Section 2.3.

(2) The effect of online misidentification of the IM on the accuracy of the *SI*.

The reason to set (2) is that the derivation in Section 2.3 is on a prerequisite that IM is correctly identified in real-time for each contingency. Therefore it is also essential to check the effects of misidentification of IM on the calculation of *SI*.

2.4.1 Test System Description

A modified version of IEEE 16-machine 68-bus system with 9 DFIG-based WPPs, shown in Figure 2.5, is used to evaluate the effectiveness of the proposed *SI*.. The 9 WPPs are installed at buses 18, 22, 25, 29, 31, 32, 36, 41, and 42 in the modified 68-bus system. All SGs in the system are detailed 6th-order models and equipped with DC4B excitation systems. IEEEST stabilizers and IEESGO governors are installed for each SG. Therefore, the internal voltage magnitude and mechanical power of SGs vary during the transient simulations. It might be helpful to mention that these values are assumed to remain constant for simplifying the derivations in Sections 2.2 and 2.3. Such a simplification is considered inside the developed method, but not the stability simulations. In addition, each WPP is modeled by an aggregated 1.5 MW DFIG model. All of these dynamic models are available in [25] and their parameters are given in [118] and Appendix B. The computer used in the simulations featured an Intel 3.4-GHz CPU with 16 GB of RAM.

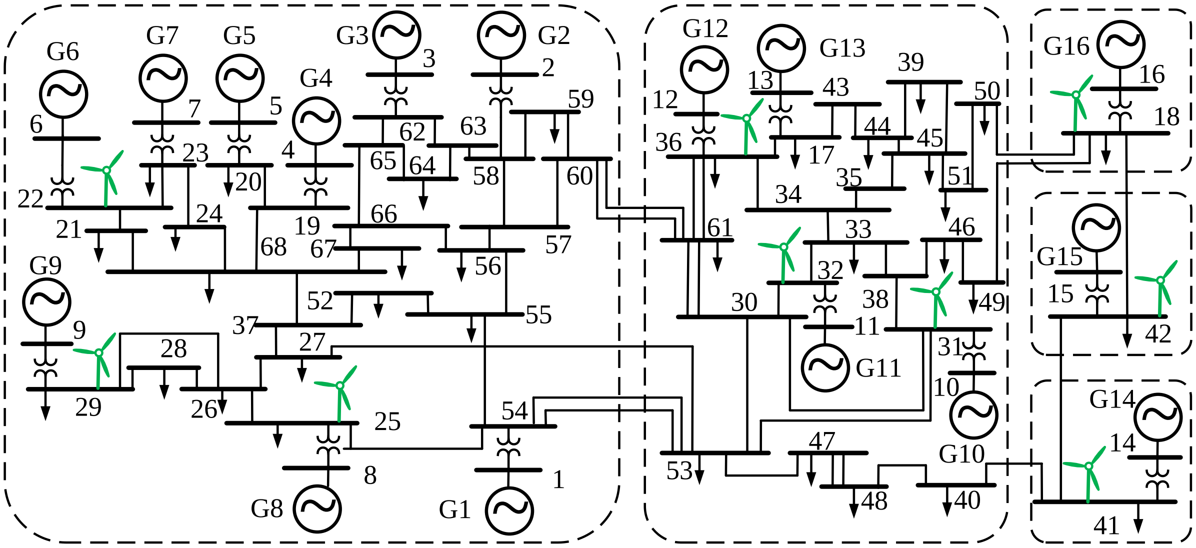

Figure 2.5: Modified IEEE 68-bus test system.

2.4.2 Generation of the Test Cases

A variety of test cases are required to assess the proposed *SI*. The test cases are obtained from Monte Carlo TDSs. In each simulation, the system admittance matrix at $t_{\mathrm{f}+}$ and $t_{\mathrm{cl}+}$, rotor angles of each SG at t_{f} and t_{cl}, pre-fault internal voltage magnitudes of each SG, and voltages of each POI at $t_{\mathrm{f}+}$ and $t_{\mathrm{cl}+}$, as discussed in Subsection 2.3.3, are used to calculate the *SI*. To carry out the

Monte Carlo TDSs, reasonable uncertainty models, including outputs of WPPs, load levels, and fault locations and durations, are essential.

In practice, these uncertainty models can be statistically estimated from the corresponding historical observations. In this study, the generation of each WPP, represented by 24 probability density functions (PDFs) that correspond to 24 hours of a day, are estimated using Gaussian kernels in a non-parametric way using hourly historical data from [119]. The same method is applied to each load where the historical data are retrieved from [120]. Thus, before running a dynamic simulation for a specific scenario, the hour of the day is sampled randomly, and then each load and WPP outputs are sampled from its PDF of the sampled hour, and optimal power flow is then solved to balance the load and determine the output of each SG. Further, because SGs in the test systems are considered to be conventional power plants with aggregated units, the parameters of each SG are then adjusted based on their updated output. In brief, by increasing wind power penetration, some units in each conventional power plant are turned off, so the electrical parameters of each SG are adjusted accordingly, as discussed in [58]. Fault duration is randomly selected to be between 6 and 15 cycles [17]. The faults are assumed to be permanent and are cleared by switching off the faulted line. Moreover, faults are randomly applied to transmission lines for each simulation. Only three-phase faults are considered in this study, though the proposed method is capable of handling other fault types as well. The above procedures are realized by a Python-based interface and the Monte Carlo simulations are carried out in PSS/E software, which provides the Python application programming interface (API).

Different wind power penetrations are also set for the system for testing. Wind power installed capacity ratio (WIC) in the system is set to 10, 30 and 50% of the total available capacity of SGs. These scenarios are denoted as WIC0, WIC30, and WIC50%. Finally, for each WIC scenario, 7000 simulations are carried out in the system, as show in Table 2.1.

Table 2.1: Simulation data of the test system for different WIC scenarios.

Wind scenarios	Number of the simulated cases
WIC10%	7000
WIC30%	7000
WIC50%	7000

2.4.3 Assessment of the Proposed *SI*

Two assessment tests are carried out in this Section: (1) the validity of the virtual variable admittances developed in Section 2.3 and (2) the effect of online misidentification of the IM on the accuracy of the *SI*.

For (1), the accuracy of the SI calculated with the variable admittances is compared to the accuracy calculated with static pre-fault WPP-equivalent admittances. It is worth noting that, in the static admittance scenario, the WPPs are equivalent to static admittances whose values are calculated by (2.26) using the pre-fault conditions. During transients, the dynamics of the WPPs are ignored, i.e., the values of the WPP-equivalent admittances remain unchanged. Thus, in case of a contingency, the EEAC as listed in (2.1)–(2.19) and (2.51) can be directly applied to calculate the SI.

For (2), two different IM online identification settings are made for the two tests in (1): the IM is either assumed correctly identified for each case, or randomly selected from a set of patterns that may appear due to the fault line.

Therefore, four settings are designed for the *SI* calculation, as listed in Table 2.2. The accuracy of the *SI*s obtained under the four settings is then assessed and compared with respect to different threshold values and WICs. For this purpose, the cases simulated on the test system for the different WIC scenarios are employed for the validation. For each WIC scenario, the SI value is calculated for the 7000 cases under the four different settings in Table 2.2. For the sake of assessment, the threshold value for stability prediction is increased from -1 to 1 in increments of 0.1, and cases with an *SI* value smaller (larger) than the threshold value will be predicted as unstable (stable). The accuracy is the ratio of the number of correctly predicted cases to the total number of cases (7000). The results are presented in Figure 2.6.

It can be seen from Figure 2.6 that increasing the WIC results in a decrease in the overall prediction accuracy. With the proposed *SI*, the average stability prediction accuracy is 91.38% with WIC=50%, which is 2.81% lower than the case with WIC=10%. Even so, the prediction accuracy of the proposed *SI* is markedly better than those in which the variable admittances are replaced by static ones in the *SI* calculation process; the average accuracy improvement for WIC10, 30, and 50% is 2.18, 5.17, and 8.71%, respectively. Such outcomes demonstrate the efficacy of the variable admittances on modelling the dynamics of WPPs, and validate the effectiveness of the proposed *SI* for cases with high penetration of wind power. Moreover, Figure 2.6 shows that the accuracy is susceptible to the settings of the threshold value and, last but not least, that the misidentification of IM can degrade the overall accuracy. Hence, to further improve the accuracy, the novel framework is introduced and tested in Chapter 3.

Table 2.2: Different settings for *SI* calculation.

Settings	Modelling of WPPs	IM identification
S1	Static admittances	Randomly selected
S2	Static admittances	Correctly identified
S3	Variable admittance	Randomly selected
S4	Variable admittance	Correctly identified

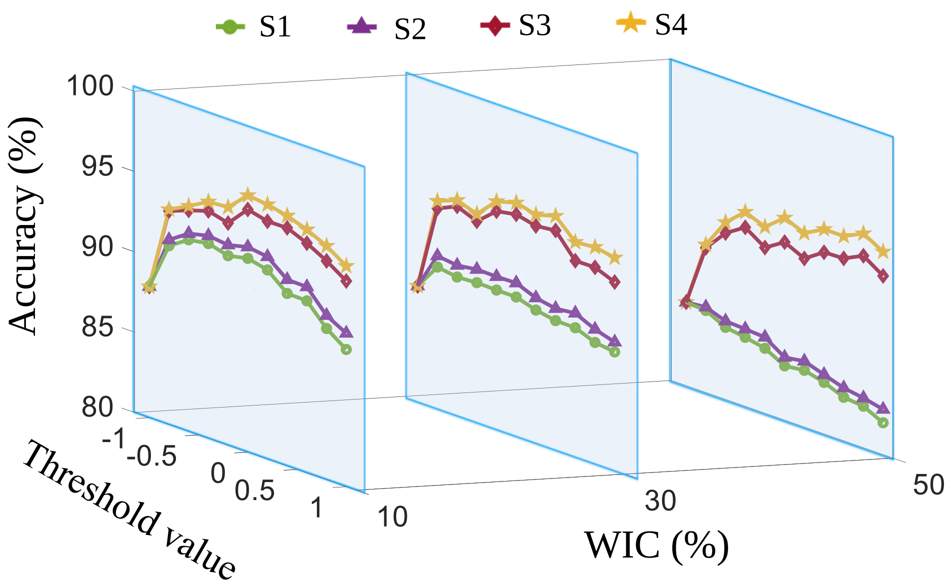

Figure 2.6: The stability prediction accuracy of different techniques with respect to WICs for different threshold values.

2.5 Summary

In this chapter, a novel transient *SI* inspired by EEAC- and PMU-based techniques is presented, in which the dynamic behavior of wind power plants is taken into account. The proposed *SI* algorithm can be calculated right after fault clearance without differential/integral operations and be applied to large-scaled WPP-connected power systems. The simulation results validated the effectiveness of the proposed *SI*, which advances the development of a novel transient stability prediction framework for wind energy-connected power systems. The framework is introduced in the next chapter.

3 Transient Stability Prediction of Power Systems with High Wind Power Penetration

3.1 Introduction

Taking advantage of the *SI* developed in Chapter 2, an *SI* vector, which consists of the *SI* values of an overall set of instability modes (IMs) of a certain system, is developed in this chapter. The *SI* vector is then used as a feature and applied to an ensemble classifier algorithm, which demonstrates a superior prediction performance. This chapter starts by discussing the definition and identification of IM and its importance to *SI* calculation. This is followed by the construction of the *SI* vector and the introduction of the selected ML-technique, ensemble DT. Finally, the proposed solution for stability prediction is presented followed by several study cases.

3.2 Construction of an *SI* Vector

3.2.1 Instability Modes (IM)

Instability mode (IM) is a generator grouping structure that separates SGs into two groups when the synchronism of the system is disturbed; the critical SGs and the remaining ones [74]. To visualize the concept of IM, Figure 3.1 shows the rotor angle trajectories of an unstable case simulated from the IEEE 68-bus system, where the critical and remaining SGs are clustered based on their rotor angle trajectories, whereby the IM is identified. Note that IMs are similar to coherent groups of generators with the main exception that they only contain two clusters of generators [32], [74], [106].

It can be seen from Chapter 2 that the IM is the "reference coordinate" for calculations of *SI*s; therefore, correct IM identification is essential to *SI* calculation. In fact, different types of IM can be triggered from a specific power system under different fault conditions, and the pattern that may occur is determined by system structure, fault location, fault duration, system operating conditions, etc. A misidentification of IM would result in erroneous SI values. However, the existing real-time IM identification methods require a long observation window of post-fault data, which may greatly delay the stability prediction time [45].

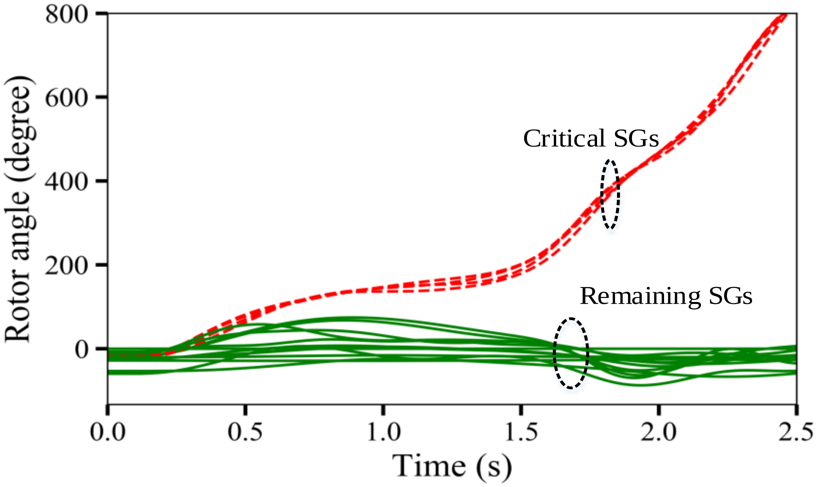

Figure 3.1: An example of IM in a power system.

3.2.2 *SI* Vector

Fortunately, although it may be unfeasible to identify the IM precisely at $t_{\mathrm{cl}+}$, the finite set of all feasible IM layouts of a certain system, Ω^{IM}, can be easily collected from a specific power system either through adequate offline simulations or historical contingency records [6], [58]. Having Ω^{IM} for a specific system, an SI vector, designated as $\boldsymbol{SI}$, which consists of the SI values of all finite sets of feasible IMs of a certain system, is constructed as

$$\boldsymbol{SI} = \left[SI_1 \;\; SI_2 \;\; \dots \;\; SI_{|\Omega^{\mathrm{IM}}|} \right]^{\mathrm{T}} \tag{3.1}$$

This SI vector can further be used as a feature (also called a predictor) and applied to a classifier algorithm for transient stability prediction. This hybrid method is one of the contributions of this research work.

Hence, with a pre-identified Ω^{IM}, an SI vector can be calculated at $t_{\mathrm{cl}+}$ by the proposed SI algorithm. Taking advantage of a set of SI vectors, an ML classifier algorithm is then applied for the training of a transient stability prediction model. The advantages of using the SI vectors as features include the following:

(1) *Features are more informative and discriminative*. Each element in the column vector correlates with the stability margin of each IM. Therefore, the proposed method has sufficient potential to outperform the existing ML-based stability prediction methods in which the features are the unprocessed data directly obtained from PMUs [56], [60], [17], [66].

(2) *No online IM identification procedure is needed.* The IM identification, known as clustering of the critical and remaining SGs, provides the “reference coordinate” for calculations of SIs, as an inaccurate online IM identification may lead to erroneous prediction results [32], [106]. However, the existing online IM identification methods require long post-fault observation windows, which may be impractical for real-life power systems that demand an extremely short time to trigger the emergency control action [44], [45]. Despite this, the Ω^{IM} of a real-life system can be pre-identified by analyzing offline simulations of various disturbances during which each WPP can also be clustered into an associated SG coherent group as mentioned in Section 2.3.1. Having Ω^{IM} for a specific system, in case of a contingency, the *SI*s for all possible IMs are calculated using the developed algorithm in a parallel manner. Thus, an SI vector is formed, and no online IM identification is needed.

(3) *More reliable prediction results are achieved.* In the proposed approach, each element in the SI vector is projected into a high dimensional space to search a hypersurface that separates the stable and unstable cases via an ML technique. Therefore, compared with identifying the instability either from a conservative or optimistic SI threshold value, the classifier hypersurface trained from the SI vector provides a more reliable prediction [32], [42], [106].

3.3 Ensemble DT

3.3.1 Ensemble Learning

An ensemble learning technique is selected to train the stability prediction model. Ensemble learning combines the predictions of several individual learners to obtain better predictive performance over a single learner. Figure 3.2 illustrates a general structure of ensemble learning.

The individual learners of an ensemble model can be either trained by the same or different ML algorithms (e.g., SVM, ANN, DT, K-means). The former is known as a homogeneous ensemble model, and the latter is heterogeneous. Since this research focuses more on feature selection instead of ML algorithms themselves, the homogeneous type is utilized in this research.

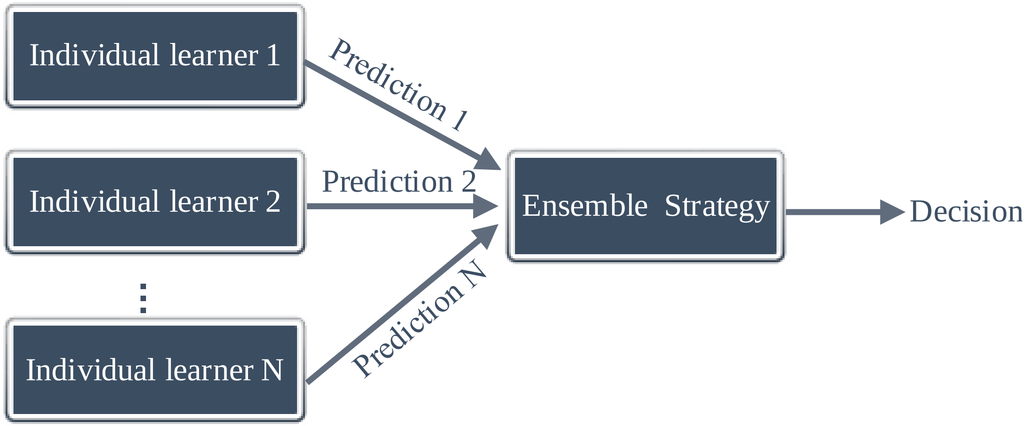

Figure 3.2: Ensemble learning.

In a homogeneous ensemble model, individual learners are also called weaker learners or base estimators. To improve the prediction performance of the ensemble model, each individual learner should be "good and independent," i.e., each of them is designed differently and works for the same goal. For this reason, the training and combination strategy of each individual learner should be carefully designed. The commonly used methods for training are introduced below.

3.3.2 Ensemble Methods

Two families of ensemble methods are usually distinguished: bagging and boosting.

In bagging methods, the driving principle is to build several learners (estimators) independently and then to average their predictions. On average, the combined learner is usually better than any of the single base learner because its variance is reduced. The famous random forest algorithm is an extension of the bagging method.

By contrast, in boosting methods, base learners are constructed sequentially and one tries to reduce the bias of the combined learner. The aim is to combine multiple individual learners to produce a powerful ensemble model. Adaptive boosting (AdaBoost) is one of the most successful and commonly used boosting algorithms developed among the boosting methods [118].

In this study, an ensemble DT trained by Adaboost is employed to process the SI vectors and find the optimal classifiers. DT is amongst the most prevalent non-parametric supervised classification techniques, and an ensemble DT is a collection of multiple weighted DTs [121]. It might be helpful to mention that bagging or other classification techniques such as deep learning may also be applied to train the prediction model without loss of generality.

The Adaboost [122] for binary classification is introduced below. Assumed we have N labelled examples $((\boldsymbol{X}_1, y_1)$, $(\boldsymbol{X}_2, y_2)$..., $((\boldsymbol{X}_N, y_N))$, where $\boldsymbol{X}_i$ $(i = 1,2, \dots, N)$ is the column vector of features of each sample, and y_i is the label for each sample, where $y_i \in \{-1,1\}$. The aim is to construct an ensemble model, $\mathcal{F}(\boldsymbol{X})$, which maximizes the prediction accuracy. Assume $\varGamma$ individual learners $h_j(\boldsymbol{X})$ $(j = 1,2, \dots, \varGamma)$ will be built at the end of the training.

(1) Initial $\mathcal{F}(\boldsymbol{X})$ as none, $i = 1$, $j = 1$, and the weights of each sample equally as:

$$\varpi_{i,j} = \frac{1}{N} \tag{3.2}$$

(2) Build a new individual learner $h_j(\boldsymbol{X})$ that minimizes ϵ_j, the weighted sum error for misclassified points, where

$$h_j(\cdot)\colon \boldsymbol{X} \rightarrow \{-1,1\} \tag{3.3}$$

$$\epsilon_j = \sum_{\substack{i=1 \\ h_j(X_i) \neq y_i}}^{N} \varpi_{i,j} \tag{3.4}$$

and set ϱ_j, the weight of the new individual learner,

$$\varrho_j = \frac{1}{2} \ln \left(\frac{1 - \epsilon_j}{\epsilon_j}\right) \tag{3.5}$$

(3) Update the ensemble model $\mathcal{F}(\boldsymbol{X})$ and

$$\mathcal{F}(\boldsymbol{X}) = \mathcal{F}(\boldsymbol{X}) + \varrho_j h_j(\boldsymbol{X}) \tag{3.6}$$

(4) Update weights of each sample $\varpi_{i,j+1}$:

$$\varpi_{i,j+1} = \varpi_{i,j} \exp\left(-y_i \varrho_j h_j(\boldsymbol{X}_i)\right) \ \forall\, i = 1,2, \dots, N \tag{3.7}$$

Then renormalized $\varpi_{i,j+1}$ such that $\sum_i^N \varpi_{i,j+1}$=1. Then set $j = j + 1$, go back to step (2) until $j = \Gamma$.

The four steps above are the basic steps for training a binary ensemble classification model by Adaboost [122]. An illustrative explanation of Adaboost is shown in Figure 3.3. The training process involves incrementally building an individual learner to emphasize the instances that were previously misclassified. It can be seen from (3.7) that the weight of each sample is updated in each training iteration. In other words, according to the prediction of the latest learner, the weights of the mispredicted instances increased, otherwise decreased. Thus, each new learner is made by taking the previous learner's mistake into account.

The prediction of a trained ensemble model will be a weighted combination of each learner, $\mathcal{F}(\boldsymbol{X}) = \sum_i^{\Gamma} \varrho_j h_j(\boldsymbol{X})$. i.e., each learner has a different voting weight during the prediction, and the value of weight ϱ_j is depends on the performance of the learner during the training stage, as shown in step (2).

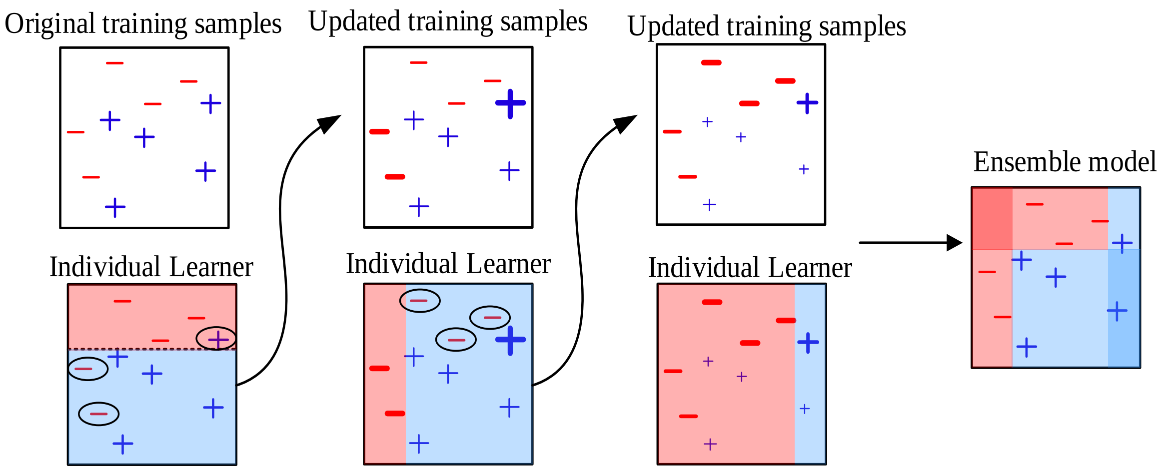

Figure 3.3: An illustrative explanation of Adaboost.

3.4 The Proposed Solution Framework

This section presents the structure of the proposed framework, in which an ensemble DT will be used to train the prediction model, and *SI* vector will be used as a feature. The framework is trained offline and be applied online.

A database, i.e., the collection of training samples, is required for the training of the prediction model. In this study, the training data are generated from the offline simulations. In practice, it can be either generated from offline simulations or obtained from historical contingency records. As for the target label (correspond to y_i in section 3.3.2), the final transient stability status of each sample is selected. It is calculated at the end of each dynamic simulation as follows [17]:

$$\lambda_{\varkappa} = \frac{2\pi - \Delta\delta_{max}}{2\pi + \Delta\delta_{max}}, \;\; \varkappa = 1, 2\,, 3, \dots, \left|\Omega^{\mathrm{f}}\right| \tag{3.8}$$

where $\Delta\delta_{max}$ is the maximum rotor angle deviation between any pair of SGs at the end of the simulation. Ω^{f} shows the set of all fault scenarios considered during the generation of that training data, and $\lambda_{\varkappa}$ indicates the final stability status of the fault scenario $\varkappa$, in which positive values indicate a stable system and negative otherwise.

The overall process of the proposed framework is shown in Figure 3.4. The generation process of the proposed framework consists of pre-identifying all possible IMs as the initial stage, followed by the databased generation as the second stage, and a model training process as the third stage.

Note as the grey area in this flowchart highlights, the formation of an SI vector can be solved in parallel, which substantially reduces the computational complexity. Once the generation of the training database is finished, the model training is conducted, and next, the trained model is tested and saved for online application.

3.5 Test and Results

The described framework is realized by a Python-based interface that calls PSS/E software [17] to carry out simulations, saves the database generated, and creates the prediction model to solve the stability prediction problem.

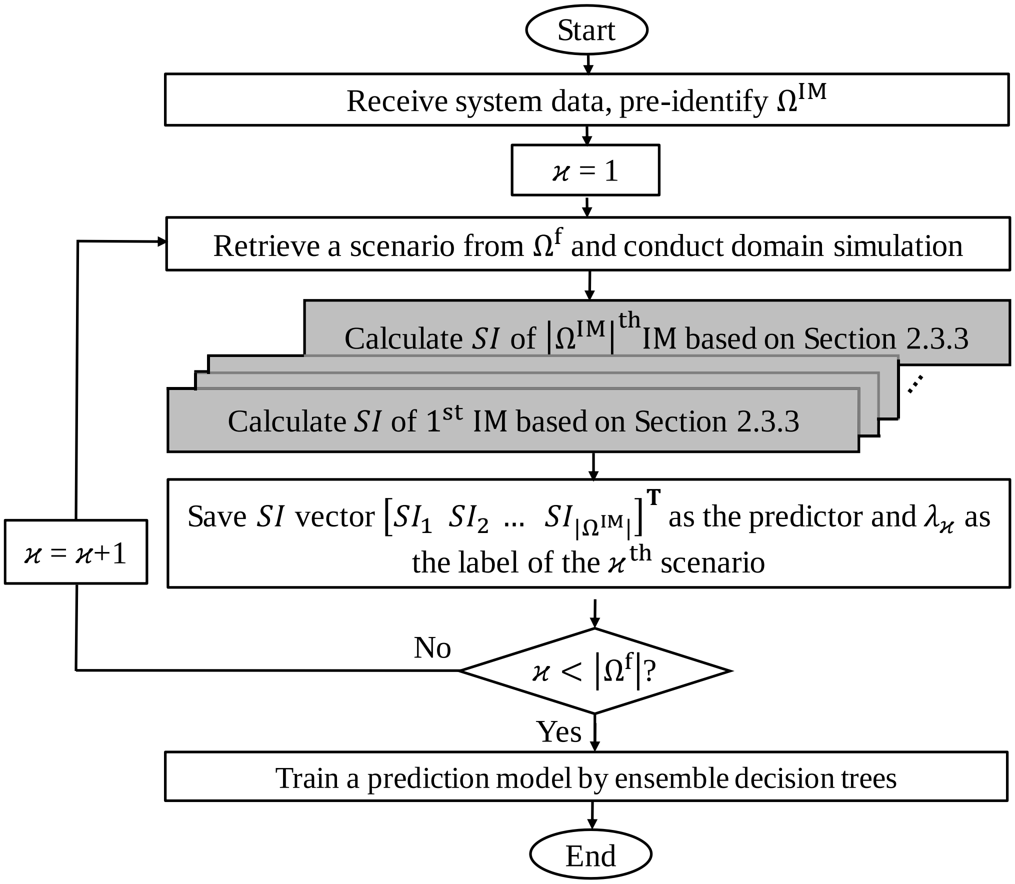

Figure 3.4: The proposed framework.

3.5.1 Test System Description

Modified versions of that IEEE 16-machine, 68-bus and 69-machine, 300-bus systems are used to perform the simulations. The data of the two systems are given in [118] and [123]. The details of the first system have been introduced in Section 2.4.1. The configuration of the modified 69-machine, 300-bus system is shown in Figure 3.5, in which 15 WPPs are installed at buses 84, 143, 150, 190, 236, 241, 7002, 7003, 7012, 7017, 7024, 7039, 7061, 7139, and 7166. All SGs in the system are WECC Type J model (GENTPJU1) and equipped with IEEET1 excitation systems. Also, PSS2A stabilizers and TGOV1 governors are installed for each SG. In addition, each WPP is modelled by an aggregated 1.5 MW DFIG model. All of these dynamic models are available in [25]. The computer used in simulations featured an Intel 3.4-GHz CPU with 16 GB of RAM.

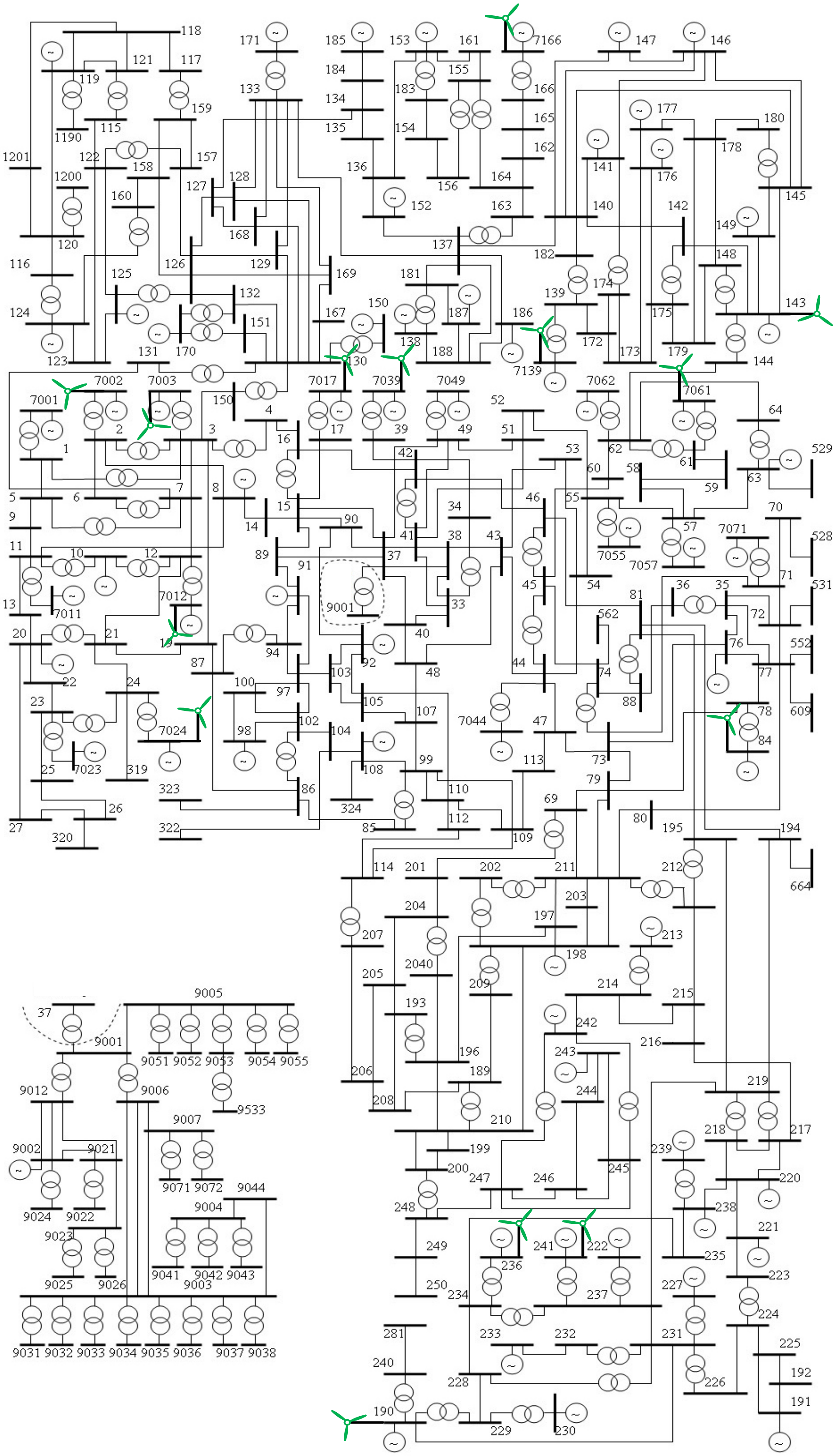

Figure 3.5: Modified IEEE 300-bus test system.

3.5.2 Database Generation

Database generation is required to validate the proposed framework. The training database is obtained from Monte Carlo TDSs. To this end, reasonable uncertainty models, including outputs of WPPs, load levels, and fault locations and durations, are essential.

The settings and process of the database generation are the same as those in Section 2.4.2. Specifically, different wind power penetrations are also set for the two systems for testing. Wind power installed capacity ratio (WIC) in both test systems is increased from 0 to 50% of the total available capacity of SGs in increments of 10%; these scenarios are denoted as WIC0 to WIC50%, respectively. Finally, for each WIC scenario, 7000 and 35000 simulations are carried out in the two modified IEEE 68- and 300-bus systems, respectively.

The data simulated for offline analysis are shown in Table 3.1, where the average pre-fault instantaneous wind power penetrations (AVG-IWP) of each WIC scenario are also given. The database is employed to perform the analyses in Sections 3.5.3 and 3.5.4 for different validation purposes.

Table 3.1: Simulation data of the two systems for different scenarios.

Wind scenarios	Modified 68-bus system		Modified 300-bus system	
	Instability ratio	AVG-IWP	Instability ratio	AVG-IWP
WIC 0%	16.53%	-	12.91%	-
WIC 10%	11.84%	4.53%	12.13%	4.95%
WIC 20%	11.71%	9.17%	10.69%	9.77%
WIC 30%	12.80%	14.22%	11.51%	14.78%
WIC 40%	14.16%	18.37%	12.54%	19.40%
WIC 50%	14.81%	23.84%	14.27%	24.30%

3.5.3 Performance of the Proposed Stability Prediction Framework

To investigate the performance of the proposed framework with respect to different levels of wind power penetration and related uncertainties, the database shown in Table 3.1 is employed for testing. In each WIC scenario, 70% of the simulation cases are randomly chosen for training while the remainder are used in testing; this process is repeated ten times and the average prediction accuracy is recorded. The training process explained in Section 3.4 is conducted, and the results obtained are reported in Table 3.2.

The performance of the SI vector in stability prediction is also compared to the features used in other state-of-the-art techniques, as shown in Table 3.2. The most prevalent features, e.g., rotor angles δ_{SG} [58], [56], [66], speeds ω_{SG} [66], and terminal voltages V_{SG} [60], [66] of each generator for before-, during-, and post-fault (at $t_{\mathrm{f}-}$, $t_{\mathrm{f}+}$, $t_{\mathrm{cl}-}$ and continuous sampling for five cycles after t_{cl}), are respectively employed to train the models for comparison purposes. For the sake of better comparison, all of the features are solved with an ensemble DT trained by the Adaboost technique. Comparing the results obtained from the proposed framework with those using δ_{SG} , ω_{SG}, or V_{SG} clearly reveals the superiority of the SI vector for stability prediction; for the two test systems, the prediction accuracies of the proposed method averaged across the six WICs are 98.53 and 97.30%, which are better than those of using δ_{SG} , ω_{SG}, or V_{SG}. With increasing wind power penetration, the proposed method has a distinct advantage in terms of accuracy. This is because, compared to other features, each SI vector correlates with a set of stability margin indices considering the influences of WPPs on system dynamics. Notably, δ_{SG} , ω_{SG}, and V_{SG} in this test require five cycles of post-fault data, which means they respond 83.3 ms later than the proposed method.

Table 3.2: Comparison of the prediction accuracy for different features using an ensemble DT.

WIC	Modified 68-bus system				Modified 300-bus system			
	δ_{SG}	ω_{SG}	V_{SG}	$\boldsymbol{SI}$	δ_{SG}	ω_{SG}	V_{SG}	$\boldsymbol{SI}$
0%	95.74%	97.96%	98.09%	**99.03%**	89.86%	93.27%	95.08%	**98.04%**
10%	93.61%	97.05%	96.88%	**98.98%**	88.24%	92.24%	93.84%	**97.87%**
20%	92.59%	95.38%	95.79%	**98.59%**	84.97%	89.52%	90.81%	**97.61%**
30%	92.18%	94.82%	94.42%	**98.46%**	83.49%	86.84%	89.26%	**97.26%**
40%	91.14%	92.06%	92.29%	**98.17%**	81.29%	84.19%	87.79%	**96.83%**
50%	89.56%	91.24%	91.35%	**97.96%**	78.34%	83.14%	85.35%	**96.17%**

In addition, the prediction accuracy is evaluated for different combinations of the existing features and the results obtained are reported in Table 3.3. Comparing Tables 3.3 and 3.2 shows that combining the features, generally, improves the prediction accuracy, while a noticeable gap still exists compared to utilizing the SI vector, especially in high wind power-integrated scenarios.

The results show that interpreting these raw data into derived features effectively improves the accuracy of the ML-based prediction model. It should be noted that an increase in the number of features could lead to an overfitting issue, which may subsequently lead to a degradation in overall performance [17], [104]. This is verified in Table 3.3 that shows the accuracy may worsen when using all three features compared to only using ω_{SG} and V_{SG}. Considering the number of features can be relatively high for large-scale networks by simply combining all available features, it is necessary to reduce the dimensionality of the input space and consequently improve the generalization performance of the classifier [17].

Table 3.3: Comparison of the prediction accuracy for different sets of input features using an ensemble DT.

WIC	Modified 68-bus system				Modified 300-bus system			
	δ_{SG}+ω_{SG}	δ_{SG}+V_{SG}	ω_{SG}+V_{SG}	δ_{SG}+ω_{SG}+V_{SG}	δ_{SG}+ω_{SG}	δ_{SG}+V_{SG}	ω_{SG}+V_{SG}	δ_{SG}+ω_{SG}+V_{SG}
0%	98.02%	98.10%	99.11%	99.10%	93.21%	95.01%	97.06%	96.99%
10%	96.69%	96.51%	97.36%	97.11%	92.27%	93.57%	94.02%	94.22%
20%	94.96%	95.98%	96.03%	96.01%	89.42%	89.54%	91.45%	91.39%
30%	94.65%	95.00%	95.13%	95.25%	86.52%	88.33%	90.63%	90.71%
40%	92.32%	92.25%	93.51%	93.26%	85.85%	87.50%	89.54%	89.30%
50%	91.15%	91.03%	92.34%	92.36%	85.11%	87.02%	88.99%	88.86%

Besides the boosting technique-trained ensemble DT, different prediction engines, including neural network (NN), support vector machine (SVM), and random forest (RF) are also applied to test the performance of each feature. In this comparison, the two networks for WIC50% are employed and all prediction engines are trained using the *scikit-learn* 0.20.4 package in Python [124]. The results noted in Table 3.4 show that the SI vector still outperforms the others while the accuracies of each features vary somewhat compared to corresponding results in Table 3.2. Specifically, the tree-based algorithms (boosting technique-trained ensemble DT, RF) show advantages in transient stability prediction, which corroborates the simulation results in [56].

Furthermore, to better illustrate the advantages of using SI vectors as features, the distribution of simulation samples in SI space and the performance of the proposed method with respect to dimensions of each SI vector are shown in Figures 3.6 and 3.7, respectively. The samples are simulated from the aforesaid IEEE 68-bus system for WIC50%, during which 18 IMs are identified, as listed in Table 3.5 in the order of the most to least prominent, based on the database. Similarly, the values in each SI vector are also sorted in the same order, and thus SI_1 ~ SI_3 is calculated based on the three most prominent IMs, respectively, in which the Ω^C/Ω^R sets is No. 1 ~ 3 in Table 3.5, respectively. Figure 3.6 indicates that samples with lower SI values are more prone to instability, and Figure 3.7 shows that the prediction accuracy improves by developing the dimension of the SI vector. Moreover, Figure 3.7 shows that as the dimension of each SI vector develops to a certain level (e.g., 16), an increase in dimension of each SI vector does not significantly affect the prediction accuracy. This indicates that, in practice, the proposed method has enough potential to accurately predict stability status in cases where IMs rarely appear in the training phase.

Table 3.4: Comparison of the prediction accuracy for different sets of input features using different ML techniques.

Algorithm	Modified 68-bus system (WIC50%)				Modified 300-bus system (WIC50%)			
	δ_{SG}	ω_{SG}	V_{SG}	$\boldsymbol{SI}$	δ_{SG}	ω_{SG}	V_{SG}	$\boldsymbol{SI}$
NN	91.03%	91.60%	91.02%	96.13%	77.30%	84.36%	85.66%	95.56%
SVM	90.04%	91.36%	91.12%	95.93%	78.34%	82.81%	84.05%	94.75%
RF	90.46%	92.30%	91.33%	97.52%	79.51%	85.15%	87.63%	96.68%

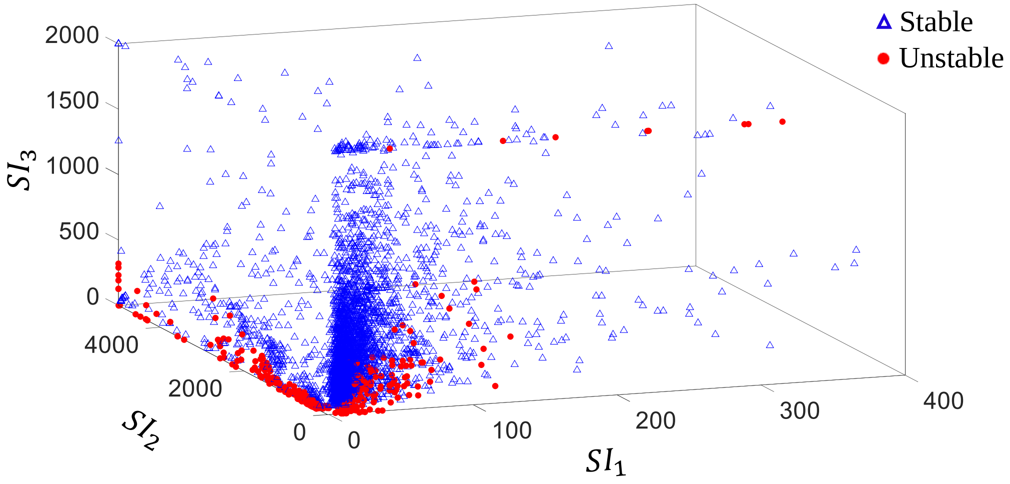

Figure 3.6: Distribution of simulation samples in the SI_1, SI_2, and SI_3 planes.

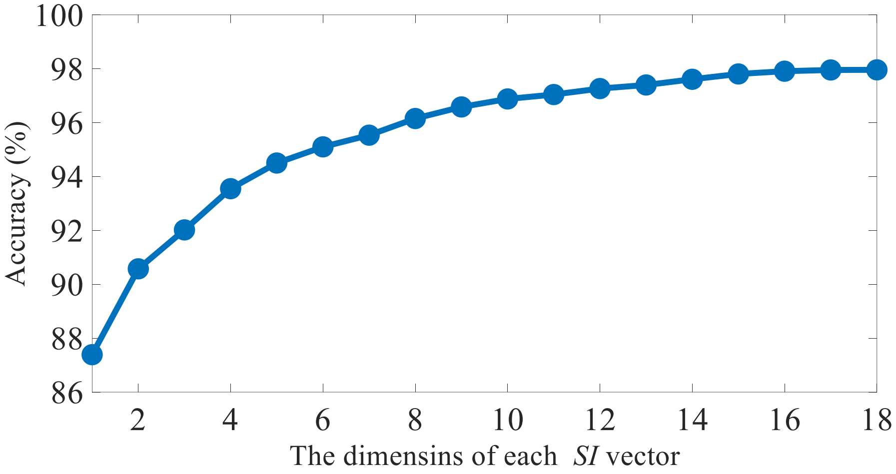

Figure 3.7: Performance of the proposed method with respect to dimensions of each SI vector.

Table 3.5: IMs identified in training database for the IEEE 68-bus test system for WIC50%.

No.	Clustering of SGs (Ω^C/Ω^R)	No.	Clustering of SGs (Ω^C/Ω^R)
1	(SG9)/(SG1–9, SG10–16)	10	(SG1–12)/(SG13–16)
2	(SG14–16)/(SG1–13)	11	(SG8)/(SG1–7, SG9–16)
3	(SG1–12, SG14–16)/(SG13)	12	(SG1–9)/(SG10–16)
4	(SG6–7)/(SG1–5, SG8–16)	13	(SG4–7)/(SG1–3, SG8–16)
5	(SG16)/(SG1–15)	14	(SG1–11)/(SG12–16)
6	(SG11)/(SG1-10, SG12–16)	15	(SG2–7)/(SG1, SG8–16)
7	(SG8–9)/(SG1–7, SG10–16)	16	(SG3)/(SG1–2, SG4–16)
8	(SG14)/(SG1-13, SG15-16)	17	(SG2–9)/(SG1, SG10–16)
9	(SG2–3)/(SG1, SG4–16)	18	(SG1–10)/(SG11–16)

3.5.4 Sensitivity Analysis with Respect to Practical Issues

The robustness of an algorithm should be assessed by its sensitivity to discrepancies among the assumed scenarios and reality. In practice, the behavior of some uncertainties may differ from those considered in the training process, e.g., when WPPs are exposed to abnormal weather. In addition, the topology of the networks may vary in real scenarios for different operations. These uncontrollable factors may interfere with the prediction results from a trained model. For this reason, two prediction models that are already trained by ensemble DT from the aforesaid two systems for WIC50% are employed for the robustness test.

In the first robustness test (RT-I), the two trained models are tested using data simulated from the corresponding system while the PDFs for each WPP are trained from another data source from [125]. In this study, the Wasserstein Distance (WD) is used to measure the difference between the original and modified PDFs of each WPP. This distance function can be defined between probability distributions μ and υ, as follows [126]:

$$\mathrm{W}(\mu,\upsilon\,) = \inf_{\pi\in\Phi(\mu,\upsilon\,)} \int_{\mathbb{R}\times\mathbb{R}} |x-y|\, d\pi(x,y) \tag{3.9}$$

where $\Phi(\mu,\upsilon\,)$is the set of probability distributions on $\mathbb{R}\times\mathbb{R}$ whose marginals are μ and υ on the first and second factors, respectively. The WDs between new PDFs of each WPP and corresponding originals of the modified 68-bus system are listed in Table 3.6. Similar settings are also implemented for the WPPs in the 300-bus system.

Table 3.6: WD between new PDFs of each WPP and corresponding originals.

WPP Connected Bus	18	22	25	29	31	32	36	41	42
WD	0.32	0.33	0.31	0.09	0.33	0.40	0.29	0.25	0.39

In the second robustness test (RT-II), the two trained models are tested using data simulated from the corresponding system under randomly $N-1$ conditions, i.e., one of the elements of the system is randomly switched out before each dynamic simulation.

7000 and 35000 cases are respectively simulated from the two systems based on the database generation method introduced in Section 3.5.2 for both RT-I and RT-II. The two trained models applied to test these data and their performance is compared with accuracies predicted by V_{SG}, which performs relatively better than δ_{SG} or ω_{SG} with respect to prediction accuracy according to Table 3.2. The results are illustrated in Figure 3.8.

Figure 3.8 shows that the prediction accuracies based on V_{SG} are vulnerable to the profile of probability distributions used to represent the system uncertainties and susceptible to changes in the system typology, while the proposed method demonstrates better robustness. This is because the calculation of SI vectors takes system operating points such as real-time topology and wind power penetration into consideration. This validates the robustness of the proposed method with respect to abnormal weather and variations in network typology.

The performance of the proposed method is also assessed in the presence of PMU measurement errors. According to the IEEE C37.118 standard, the PMU measurements should have a total vector error of less than 1% [47]. To this end, following the approach in [60], white noise is generated and imposed on all post-fault offline data listed in Table 3.1, and the training and testing process is repeated. The results are reported in Table 3.7. Compared to the results when PMU measurement errors are ignored, the average accuracies of the two systems in all WICs decrease by 0.74 and 0.98%, respectively. To conclude, the proposed method can make high-quality predictions considering noisy PMU measurements.

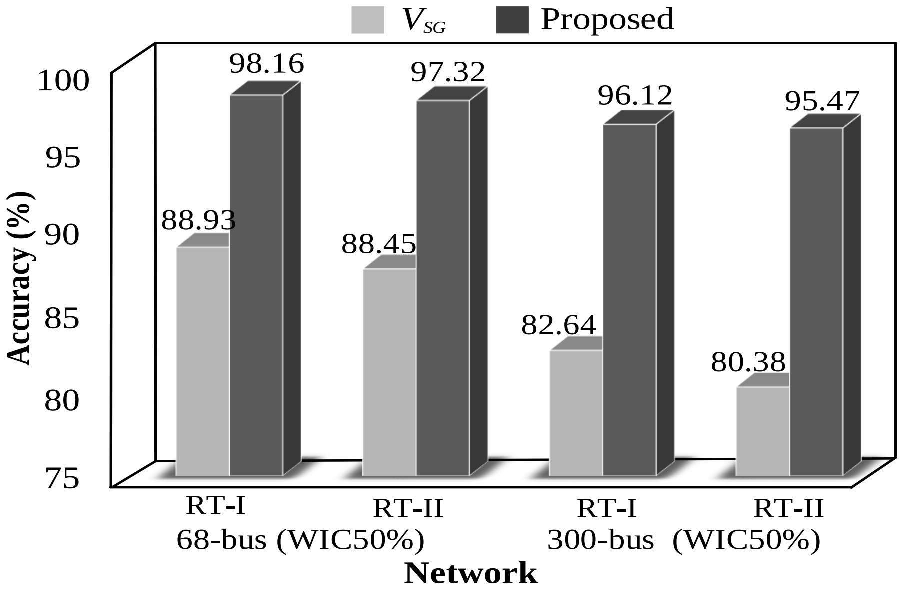

Figure 3.8: Performance of the proposed framework in robustness tests.

Table 3.7: Prediction accuracy of the proposed method considering PMU measurement errors.

WIC	0%	10%	20%	30%	40%	50%
Modified 68-bus system	98.21%	97.86%	97.73%	97.62%	97.32%	97.13%
Modified 300-bus system	97.16%	96.91%	96.48%	96.23%	95.86%	95.24%

Moreover, the performance of the proposed method is investigated with respect to the size of the training database. To do so, an ensemble DT is employed to train the prediction model with different sizes of training database. For each size, this training and testing process mentioned in Section 3.5.3 are repeated and the average prediction accuracies are illustrated in Figure 3.9. This figure shows that an adequate database is essential to train an accurate prediction model, and the performance changes slightly when the database reaches a certain level. Based on Figure 3.9, the sizes of the databases used for the two systems (7000 and 35000, respectively) in this study are adequate.

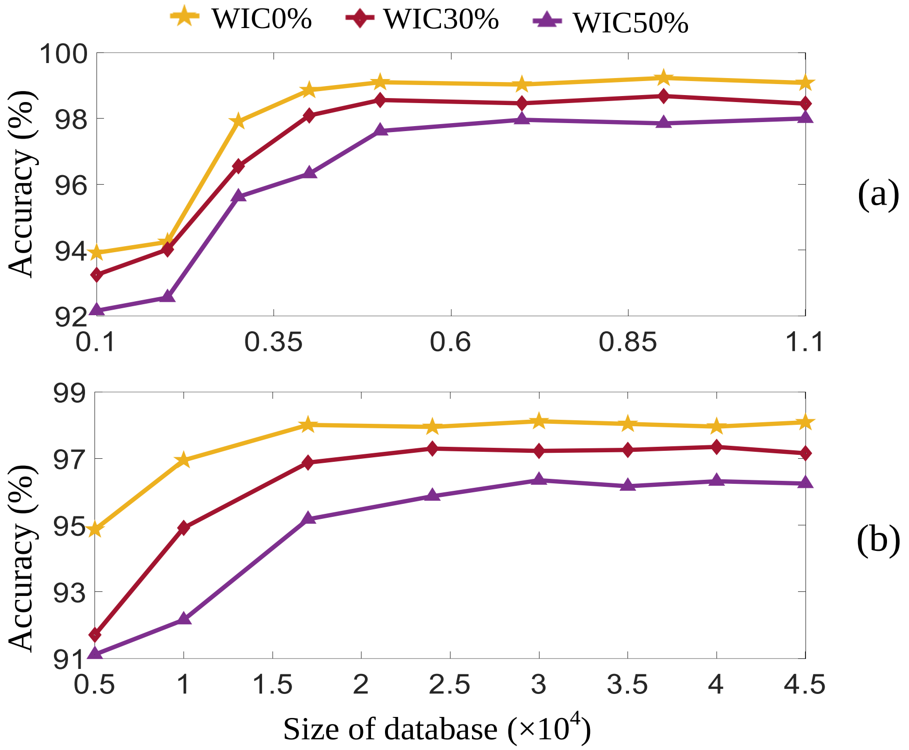

Figure 3.9: Performance of the proposed framework to the size of the training database. Tests are conducted on the (a) 68- and (b) 300-bus systems.

3.6 Summary

This chapter proposes a novel approach for transient stability prediction of power systems in the presence of high penetration of wind power. Inspired by EEAC- and PMU-related studies, and taking advantages of the new stability index developed in Chapter 2, an approach is then put forward in which the developed algorithm is employed in parallel to find *SI*s for all possible IMs layouts; *SI* vectors are then constructed and selected as features for transient stability prediction.

The effectiveness of the proposed approach is validated by an ensemble DT on two IEEE test systems at different wind power penetration levels. The results obtained and comparisons reported reveal the superiority of the proposed approach in terms of accuracy, speed, and robustness.

4 Preventive Dispatch for Power Systems with High Wind Power Penetration

4.1 Introduction

From a preventive dispatch perspective, this chapter explores a method that improves the stability of power systems with high wind power penetration. This study not only focuses on how to increase the system stability by power dispatch, but also how to achieve it “wisely”. That is because the preventive dispatch, if not carefully planned, can significantly increase the system operating cost. Power systems should be operated at a reasonable operating cost while meeting the stability requirements. This chapter aims to offer a computationally efficient dispatching method with a satisfactory trade-off between economics and stability.

In previous research, different solutions for transient stability constrained OPF (TSC-OPF) have been proposed [67]–[76]. Nevertheless, these approaches mainly focus on deterministic systems and face challenges when applied to high renewable energy-integrated systems. Multisource renewables such as wind power are highly variable even within a single hour [77]. Therefore, numerous possible system operating points need to be considered in each power dispatch given that OPF is frequently solved for the hour-ahead system [78], [79]. This results in an unacceptable computational burden for deterministic approaches. In addition, as stochastic factors in power systems affect transient stability, it is necessary to analyze transient stability from a probabilistic point of view. In previous studies, a point estimate method and Kalman filter are respectively applied in to estimate the uncertainty of the system stability margin caused by the wind power uncertainties [82], [83]. In [84], Taguchi’s orthogonal array testing is utilized to solve the TSC-OPF problem considering wind power variations. Although these methods dramatically reduce the test scenarios, the influence of wind power uncertainty on stability indices may not be fully considered, and the accuracy of the estimations may degrade if the wind generation does not follow the predetermined probability distribution density function. Moreover, the existing TSC-OPF studies mainly handle a limited set of fault scenarios. However, a particular dispatching scheme made against specific fault scenarios may, in turn, deteriorate the system stability against other scenarios. Given the probabilistic nature of different contingencies, a dispatching method that sets flexible probabilistic stability standards against various contingencies can be beneficial to the overall stability of systems.

To unravel the above-mentioned restrictions, a novel power dispatching method is introduced. To eliminate the need to run excessive time-consuming TDSs in each dispatching operation, an ML-based model is trained offline to predict CCT and IM. Then, IM-categorized probabilistic transient stability constraints (PTSCs) are formulated for all transmission lines that potentially trigger instability. Based on the predictions, the current system operation plan is evaluated with respect to the PTSCs, and the sensitivity of the probabilistic level of CCT to the active power generated from the critical generators is calculated for each IM category. Accordingly, a set of dispatching constraints are generated and embedded into the conventional OPF formulation, and then the dispatching is rescheduled. The checking-and-rescheduling procedures are conducted iteratively until the optimal operation state is found.

4.2 Mathematical Formulation

In this section, the mathematical formulation of the problem is introduced. In this regard, the proposed method should minimize the objective function and, at the same time, satisfy all the constraints.

4.2.1 Objective Function

The objective of generation scheduling is to minimize the total operating cost of all SGs in the system.

$$\min \sum_{i \in \Omega^{\mathrm{SG}}} \left(a_{2i} P_i^2 + a_{1i} P_i + a_{0i}\right) \tag{4.1}$$

where

a_{2i}, a_{1i}, and a_{0i} are the generation cost coefficients of the SG connected at bus i,

Ω^{SG}: set of SGs in the system.

4.2.2 Static Constraints

The AC power flow equations are described by(4.2):

$$\begin{cases} P_i + P_{\mathrm{W}i} - P_{Load.i} - V_i \sum\limits_{j\in\Omega^B} V_j\left(G_{ij}\cos\theta_{ij} + B_{ij}\sin\theta_{ij}\right) = 0 \\ Q_i + Q_{\mathrm{W}i} - Q_{Load,i} - V_i \sum\limits_{j\in\Omega^B} V_j\left(G_{ij}\sin\theta_{ij} - B_{ij}\cos\theta_{ij}\right) = 0 \end{cases} \quad i \in \Omega^{\mathrm{B}} \tag{4.2}$$

where

Ω^{B}: set of all buses in a power system;

P_i: active power injection of SG at bus i,

Q_i: reactive power injection of SG at bus i,

V_i: voltage magnitude of bus i,

$P_{\mathrm{W}i}$: active power injection of WPP at bus i,

$Q_{\mathrm{W}i}$: reactive power injection of WPP at bus i,

θ_{ij}: voltage angle difference between bus i and j;

$P_{Load.i}$: active load at bus i;

$Q_{Load,i}$: reactive load at bus i;

G_{ij}: conductance between buses i and j,

B_{ij}: susceptance between buses i and j.

Equation (4.3) denotes the constraints of bus power injection, bus voltage magnitudes, and line current magnitudes,

$$\begin{cases} \underline{P_i} \le P_i \le \overline{P_i}, i \in \Omega^{\mathrm{SG}} \\ \underline{Q_i} \le Q_i \le \overline{Q_i}, i \in \Omega^{\mathrm{SG}} \\ \underline{V_i} \le V_i \le \overline{V_i}, i \in \Omega^{\mathrm{B}} \\ \underline{I_i} \le I_i \le \overline{I_i}, i \in \Omega^{\mathrm{L}} \end{cases} \tag{4.3}$$

where

$\underline{P_i}$ and $\overline{P_i}$: lower and upper active power limits of SG_i, respectively;

$\underline{Q_i}$ and $\overline{Q_i}$: lower and upper reactive power limits of SG_i, respectively;

$\underline{V_i}$ and $\overline{V_i}$: lower and upper voltage limits of bus i;

$\underline{I_i}$ and $\overline{I_i}$: lower and upper current limits of transmission line i;

I_i: current on line i,

Ω^{L}: set of transmission lines.

4.2.3 Dynamic Constraints

The dynamic equations are listed as,

$$\begin{cases} \dot{\boldsymbol{x}}(t) = \mathbf{D}(\boldsymbol{x}(t), \boldsymbol{y}(t), \boldsymbol{u}, \boldsymbol{\varepsilon}) & \\ \mathbf{E}(\boldsymbol{x}(t), \boldsymbol{y}(t), \boldsymbol{u}, \boldsymbol{\varepsilon}) = 0 & t \in [t_0, t_{end}] \\ \boldsymbol{x}(t_0) = \boldsymbol{x}_0 \, , \boldsymbol{y}(t_0) = \boldsymbol{y}_0 & \end{cases} \tag{4.4}$$

where

t_0: initial time of transients,

t_{end}: end time of transients,

$\boldsymbol{x}(t)$ and $\boldsymbol{y}(t)$: state and algebraic variables in the transient period $[t_0, t_{end}]$, respectively,

$\boldsymbol{x}_0$ and $\boldsymbol{y}_0$: initial values of $\boldsymbol{x}(t)$ and $\boldsymbol{y}(t)$ at t_0,

$\boldsymbol{u}$: control variables such as the active power output of each SG,

$\boldsymbol{\varepsilon}$: uncertainties that affect the system operating point, e.g., variations of the power generated from each wind power plant (WPP), uncertainty of load, etc.,

$\mathbf{D}(\cdot)$: differential equations representing system transients,

$\mathbf{E}(\cdot)$: power balance equations to be satisfied at each instant of time.

In this study, SGs in the system are round rotor generator model GENROU equipped with IEEEX1 excitation systems. IEEEST stabilizers and IEESGO governors are installed for each SG. Each WPP is modeled by an aggregated 1.5 MW DFIG model. These dynamic models and their parameters are given in [25]. Other dynamic models for each device can be used without loss of generality.

Note that the dynamic constraints given by (4.4) are not directly formulated in the power dispatching formulation. Instead, they are considered inside the dynamic simulations during the database generation stage. Thus, the dynamics of the system can be learned by the prediction model, which is then applied to online dispatching operations. More details about the prediction model are discussed in Section 4.3.

4.2.4 Probabilistic Transient Stability Constraints

Generally, the PTSC of a power system can be formulated as [82]:

$$\rho\left(\tau\Big((\boldsymbol{x}_{sol},\boldsymbol{y}_{sol}),\Omega^{\mathrm{L}},\boldsymbol{\zeta},\boldsymbol{u},\boldsymbol{\varepsilon},T\Big)>\alpha\right)\ \geq\beta \tag{4.5}$$

where

$\rho(\cdot)$ represents the probability;

τ: stability index of interest, which is CCT in this study but can also represent other stability indices;

$(\boldsymbol{x}_{sol},\boldsymbol{y}_{sol})$: dispatching solution, i.e., the system state and algebraic variables after a certain dispatch;

$\boldsymbol{\zeta}$: PDF of fault occurrence for each transmission line in Ω^{L};

T: time interval between two consecutive dispatching operations. T is set to one hour in this research given that OPF is frequently solved for hour-ahead operation [78], [79].

α: user-defined threshold value of CCT.

Constraint (4.5) states that if a random fault occurs at lines in Ω^{L} between two consecutive dispatching operations, considering $\boldsymbol{\zeta}$ and $\boldsymbol{\varepsilon}$ during this period, the probability of $\mathrm{CCT}>\alpha$ must not be less than the security level β.

Figures 4.1 and 4.2 are illustrative examples showing the idea of incorporating PTSCs into the power dispatch problem using a two-machine power system. Figure 4.1 shows two dispatching solutions and their corresponding possible operating points in an interval T, in which the two solutions are calculated from OPF with and without PTSCs. Figure 4.2 depicts the PDF of CCT of the two solutions with respect to a set of potential faults, in which the violation area corresponds to the possibility that CCT below the threshold value α. The two figures convey the idea that by incorporating PTSCs into power dispatch, the stability level of the system is expected to satisfy the security requirement.

However, it is cumbersome to analyze each potential fault individually after considering $\boldsymbol{\varepsilon}$, and therefore dealing with (4.5) in the OPF problem can be very complicated. In this regard, given that a certain dispatching solution may have a similar effect on system vulnerability to multiple faults that trigger the same IM [74], PTSCs are formed in a more generic and tractable manner by:

$$\rho\left(\mathrm{CCT}\left((\boldsymbol{x}_{sol},\boldsymbol{y}_{sol}),\Omega^{\mathrm{L}},\boldsymbol{\zeta},\boldsymbol{u},\boldsymbol{\varepsilon},T\right)>\alpha_k\right)\geq\beta_k \qquad \forall\, k\in\Omega^{\mathrm{IM}} \tag{4.6}$$

where Ω^{IM} is the set of all IMs that may appear in the network. This manner also helps to set flexible probabilistic stability standards for each IM to be prevented. Note that the definition of IM has been introduced in Section 3.2.1. In the following, $\rho\left(\mathrm{CCT}\left((\boldsymbol{x}_{sol},\boldsymbol{y}_{sol}),\Omega^{\mathrm{L}},\boldsymbol{\zeta},\boldsymbol{u},\boldsymbol{\varepsilon},T\right)>\alpha_k\right)$ is represented as $\rho_k(\mathrm{CCT}>\alpha_k)$ for simplicity.

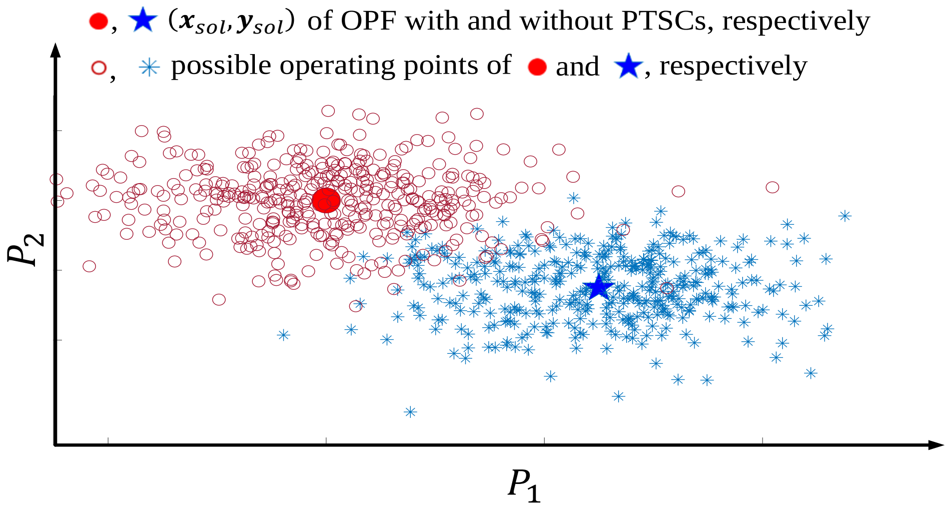

Figure 4.1: Illustration of the power dispatch with and without PTSCs.

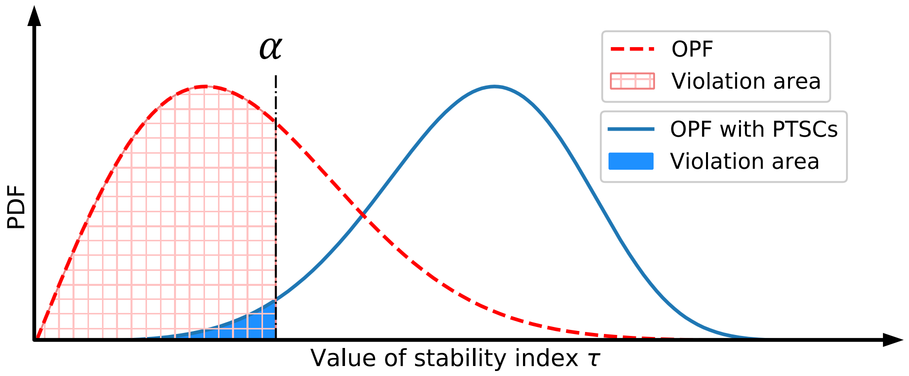

Figure 4.2: PDF of stability index with and without PTSCs.

As the system operating cost may increase after considering the PTSCs, this study aims to offer a computationally efficient dispatching method with a satisfactory trade-off between economics and stability.

4.3 Difficulties and the Proposed Solution

4.3.1 Difficulties

The difficulty of this problem lies in how to find the optimal dispatching solution after considering the PTSCs. It can be decomposed into three the sub-difficulties:

(1) How to rapidly collect the stability status of the system against a massive of preconceived fault scenarios.
(2) After obtaining the stability status, how to check it with respect to PTSCs.
(3) How to dispatch the system based on the results from (2).

To solve the above problems, a solution is proposed and elaborated through Sections 4.3.2.–4.3.5.

4.3.2 Training of the (CCT, IM) Prediction Model

The CCT and IM are two key indices in power system transient stability analysis. The value of CCT correlates the system stability level against a specific fault, and the IM indicates the critical SGs that lose synchronism caused by the fault.

Denote $\Omega^{\mathrm{CCT,IM}}$ as a set of data pair (CCT, IM), which contains the CCTs and IMs of a specific system under all possible fault scenarios. For a deterministic system under a set of preconceived faults, the $\Omega^{\mathrm{CCT,IM}}$ can be collected by conducting TDSs for all possible fault scenarios. The $\Omega^{\mathrm{CCT,IM}}$ reflects the overall stability level of a system and identifies the vulnerable SGs; This information provides system operators with the basis for preventive dispatch. However, for a high wind power-integrated system, collecting $\Omega^{\mathrm{CCT,IM}}$ by TDSs may be computationally intractable as the potential operating points increase exponentially. As a result, the power dispatching methods assisted by TDSs may face challenges in this situation.

To address this issue, a prediction model is trained offline using an ML technique to rapidly predict the CCT and IM for a large number of possible fault scenarios without TDSs. To this end, a training database is required. In this study, it is obtained from using Monte Carlo TDSs. During the simulations, system pre-fault variables and fault locations, as listed in Table 4.1, are saved as input features for model training [127]. The data pair $(\mathrm{CCT}, \mathrm{IM})$ of each case is saved as target labels. It might be helpful to mention that the training database generation and model training are performed offline, so they do not increase the computational time during the online dispatching operations.

The training process of the ML-based model is illustrated in the left part of Figure 4.3. Note that an ML-based model is trained on and applied to the same system. To obtain an adequate and reasonable training database, the statistical models of uncertainties, including outputs of each WPP, load levels, and fault locations, are required. In practice, these uncertainties can be estimated from their corresponding historical observations. Next, Monte Carlo TDSs are conducted: in each simulation, the uncertain variables in the system are sampled from the corresponding statistical models. Then, the selected features and target labels (CCT and IM) are extracted from the simulation outputs and saved in the database. After the database is generated, a prediction model is trained and saved for online applications.

Table 4.1: Selected features and labels for prediction model training.

Features	Description
1	Rotor angles of each SG
2	Active power output of each SG and WPP
3	Reactive power output of each SG
4	Fault location (categorical feature)
Labels	Description
1	$(\mathrm{CCT}, \mathrm{IM})$

Specifically, the prediction model consists of a regression model (to predict CCT) and a multi-class classification model (to predict IM). In this research, an ensemble technique that combines multiple classification and regression trees [121] trained by the AdaBoost method [122] is applied. An introduction of AdaBoost for binary classification has been introduced in Section 3.3.2. Beyond that, AdaBoost was further explored and can be applied to multi-class classification and regression problems [128], [129].

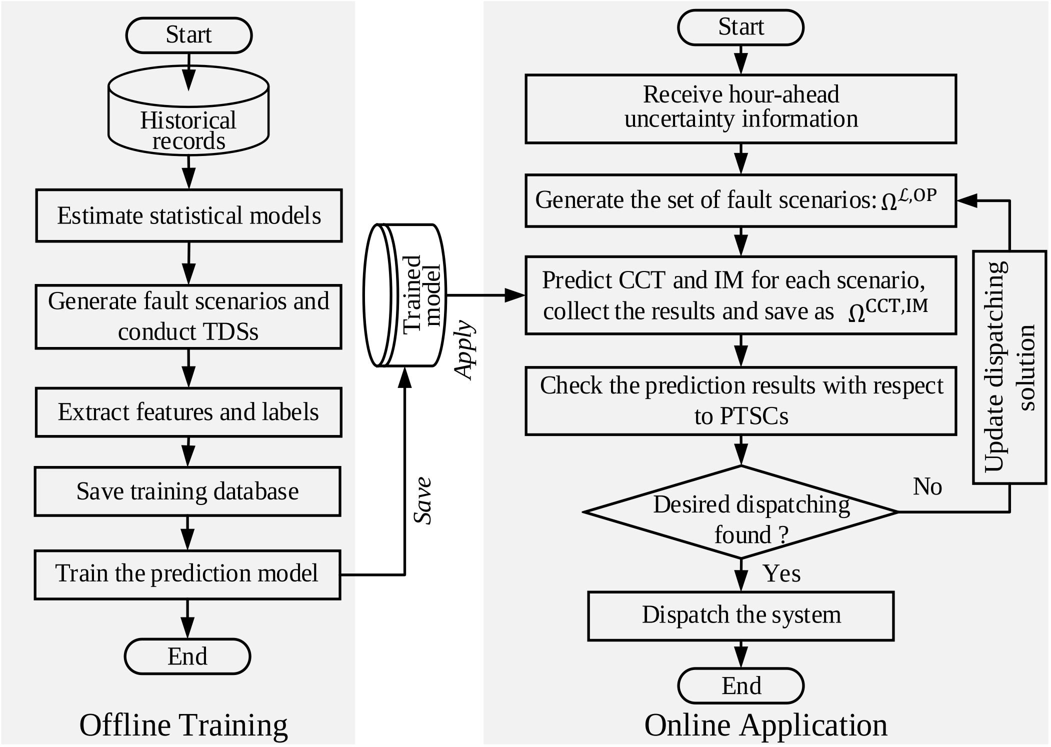

Figure 4.3: Offline training and online application of the ML-based model.

The training process using Adaboost for binary and multiple classification are similar. The process for multiple is discussed only in brief here since it is not the contribution of this research work. For the multi-class classification problem, the AdaBoost technique fits a sequence of weak classifiers on repeatedly modified versions of the data. The data modifications at each so-called boosting iteration apply weights $\varpi_1, \varpi_2, \dots, \varpi_N$ to each of the total training samples, where N is the number of total training samples. Initially, those weights are all set to $1/N$ so that the first step simply trains a weak learner on the original data. At each step, misclassified training data have their weights boosted, or decreased otherwise. As iterations proceed, examples that are difficult to predict receive ever-increasing influence. Each subsequent weak classifier is thereby forced to concentrate on the samples that are missed by the previous ones in the sequence. The final classifier is defined as the linear combination of the classifiers from each step.

Similarly, for the regression problem, regressors are trained sequentially. At each boosting iteration, a new regressor is fitted on a modified version of the original database; based on the prediction results of the newly constructed regressor, the weights of those samples most in error are adjusted. As such, subsequent regressors focus more on difficult cases. All trained regressors are combined using the weighted median at the end of the training.

Detailed descriptions of AdaBoost for classification and regression are reported in [128], [129], respectively. Other regression and classification techniques such as deep learning can also be applied without loss of generality.

4.3.3 Online Application of the Prediction Model

The online application of the trained model is illustrated in the right part of Figure 4.3. The purpose of the prediction model is to rapidly assess the transient stability of a large number of possible fault scenarios in the online application stage. To generate the scenarios, hour-ahead uncertainty information of the system, including wind power uncertainty and PDFs of fault locations, is required. Such information is fairly available to operators in practice. Notably, the hour-ahead wind power uncertainty of each WPP can be represented by a prediction interval (PI), which is prevalent in short-term wind power prediction and can provide ample uncertainty information [130]. The PDF of fault locations, $\boldsymbol{\zeta}$, can be set by system operators based on historical records. Thus, a set of feasible wind power generation scenarios, Ω^{w}, and the lists of fault lines $\mathcal{L}$, can be generated by sampling from the PIs and $\boldsymbol{\zeta}$, respectively. Next, the set of possible operating points Ω^{OP} is generated based on Ω^{w}, where $\left|\Omega^{\mathrm{OP}}\right| = |\Omega^{\mathrm{w}}|$. Further, the set of fault scenarios, $\Omega^{\mathcal{L},\mathrm{op}}$, which consider each fault at $\mathcal{L}$ for all operating points in Ω^{op}, are generated, where $\left|\Omega^{\mathcal{L},\mathrm{op}}\right| = |\mathcal{L}| \times \left|\Omega^{\mathrm{OP}}\right|$. As a result, $\Omega^{\mathrm{CCT,IM}}$ is predicted for $\Omega^{\mathcal{L},op}$ by the trained model. An illustrative explanation of predicting $\Omega^{\mathrm{CCT,IM}}$ using the trained model is shown in Figure 4.4.

The predicted $\Omega^{\mathrm{CCT,IM}}$ contains the information of CCTs and corresponding IMs for all preconceived fault scenarios. Once the $\Omega^{\mathrm{CCT,IM}}$ is collected, it will be checked with respect to PTSCs, i.e., the values of $\rho_k(\mathrm{CCT} > \alpha_k)\ \forall\ k \in \Omega^{\mathrm{IM}}$ are calculated based on the $\Omega^{\mathrm{CCT,IM}}$ and then compared to the PTSCs. To do this, the CCTs in $\Omega^{\mathrm{CCT,IM}}$ are clustered into different groups based on their related IM. Thus, $\forall\ k \in \Omega^{\mathrm{IM}}$, the PDF of the CCT, $\wp_k(\mathrm{CCT})$, can be estimated based on the statistical data of the corresponding group. In this research, it is estimated using Gaussian kernels in a non-parametric way [131]. Then, the $\rho_k(\mathrm{CCT} > \alpha_k)\ \ \forall\ k \in \Omega^{\mathrm{IM}}$ can be calculated by:

$$\rho_k(\mathrm{CCT} > \alpha_k) \ = 1 - \int_0^{\alpha_k} \wp_k(\mathrm{CCT})\, d(\mathrm{CCT}) \tag{4.7}$$

In this way, the stability status is checked with respect to PTSCs, i.e., whether $\rho_k(\mathrm{CCT} > \alpha_k) > \beta_k \ \forall\, k \in \Omega^{\mathrm{IM}}$. Then the power is dispatched based on the checking results, as discussed in the section below.

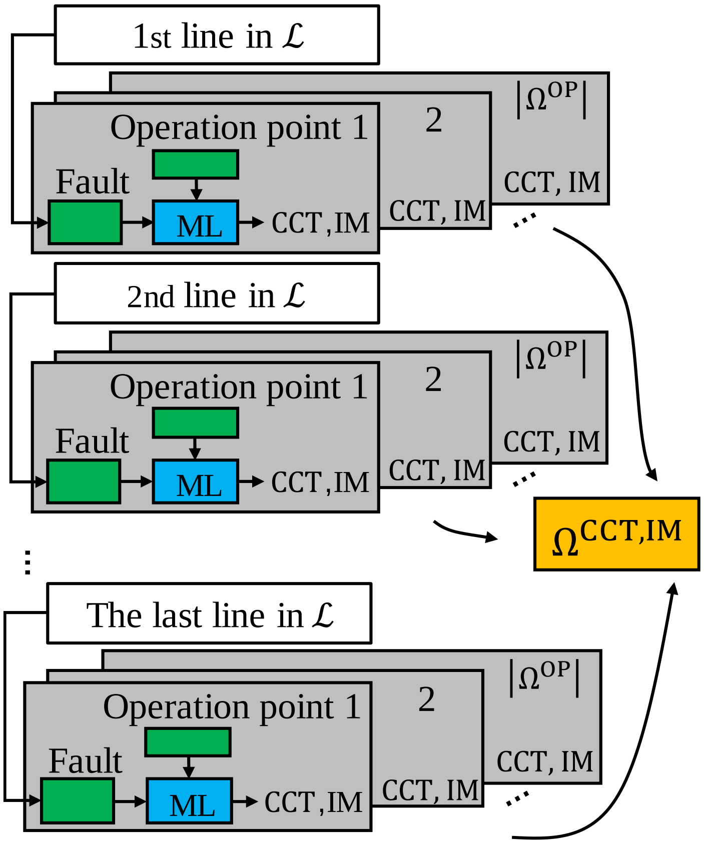

Figure 4.4: Predict $\Omega^{\mathrm{CCT,IM}}$ using the trained model.

4.3.4 Converting PTSCs into Linear Algebraic Form

This section discusses the dispatching method. In TSC-OPF studies, trajectory sensitivity has been utilized to transform the implicit transient stability constraints into explicit dispatching constraints [70]–[73]. However, the calculation of the trajectory sensitivities can be computationally expensive even for a deterministic system [70], [82].

Notably, these works established that the transient stability level has a quasi-linear relationship with many key factors, such as the generation output from critical SGs [84]. The transient stability level of the system against a specific k can be improved by shifting the active power generated from Ω_k^{C} to Ω_k^{R} where Ω_k^{C} and Ω_k^{R} are the set of critical and remaining SGs in regard to IM k, respectively [72]–[74]. The physical interpretation of this active power shift can be explained via the EEAC, which has been introduced in Section 2.2. Based on the EEAC, Ω_k^{C} and Ω_k^{R} can be modeled by two equivalent SGs, and then be reduced to a one-machine-infinite-bus (OMIB) system, as shown in Figure 2.1. The dynamic mapping of the equivalent OMIB under such an IM is given by (4.8)–(4.10), where ω, P_i, P, $P_{mech,i}$, P_{mech}, ω_0, M_C and M_R have been introduced in Section 2.2.

$$\frac{M_C M_R}{\omega_0(M_C+M_R)}\frac{d\omega}{dt} = P_{mech} - P \tag{4.8}$$

$$P_{mech} = \frac{1}{M_C+M_R}\left(M_C\sum_{i\in\Omega_{\mathrm{k}}^{\mathrm{C}}} P_{mech,i} - M_R \sum_{j\in\Omega_{\mathrm{k}}^{\mathrm{R}}} P_{mech,j}\right) \tag{4.9}$$

$$P = \frac{1}{M_C+M_R}\left(M_C\sum_{i\in\Omega_{\mathrm{k}}^{\mathrm{C}}} P_i - M_R \sum_{j\in\Omega_{\mathrm{k}}^{\mathrm{R}}} P_j\right) \tag{4.10}$$

Equations (4.8)–(4.10) show that shifting the power from Ω_k^{C} to Ω_k^{R} functionally reduces P and P_{mech} of the OMIB without changing the total power supply, thus, helping to reduce the angular acceleration of the OMIB during a fault. Accordingly, the transient stability is reinforced for a specific IM. The same procedure can be applied to all IMs of interest in a straightforward manner.

In this research, it is assumed a local quasi-linear relationship exists between the probabilistic transient stability level and the active power generated from Ω_k^{C}. According to this relationship, to satisfy the PTSCs as shown in (4.6), the amount of active power generation to be shifted from Ω_k^{C} to Ω_k^{R} can be calculated.

To show the relationship, $\forall\ k \in \Omega^{\mathrm{IM}}$, it is assumed that :

$$\rho_k(\mathrm{CCT} > \alpha_k) \;=\; \mathcal{H}_k\Big((\boldsymbol{x}_{sol}, \boldsymbol{y}_{sol}), \Omega^{\mathrm{L}}, \boldsymbol{\zeta}, \widetilde{\boldsymbol{u}}, \boldsymbol{\varepsilon}, T, u\Big) \tag{4.11}$$

where $\widetilde{\boldsymbol{u}}$ includes all of the control variables except u. $\mathcal{H}_k(\cdot)$ is the implicit expression of $\rho_k(\mathrm{CCT} > \alpha_k)$, and it reveals the variables that affect the value of $\rho_k(\mathrm{CCT} > \alpha_k)$. Linearizing the function with respect to u, and ignoring the high-order terms of the Taylor series expansion given the local quasi-linear relationship, gives:

$$\Delta\rho_k(\mathrm{CCT} > \alpha_k) \approx \frac{\partial\mathcal{H}_k\Big((\boldsymbol{x}_{sol},\boldsymbol{y}_{sol}),\Omega^{\mathrm{L}},\boldsymbol{\zeta},\widetilde{\boldsymbol{u}},\boldsymbol{\varepsilon},T,u\Big)}{\partial u}\Delta u \tag{4.12}$$

where $\frac{\partial\mathcal{H}_k}{\partial u}$ is the sensitivity of $\rho_k(\mathrm{CCT} > \alpha_k)$ to u. Now, taking the P_k^{C} as u, and ΔP_k^{C} as Δu, gives:

$$\Delta\rho_k(\mathrm{CCT} > \alpha_k) \approx \frac{\partial\mathcal{H}_k\left((\boldsymbol{x}_{sol},\boldsymbol{y}_{sol}),\Omega^{\mathrm{L}},\boldsymbol{\zeta},\widetilde{\boldsymbol{u}},\boldsymbol{\varepsilon},T,P_k^{\mathrm{C}}\right)}{\partial P_k^{\mathrm{C}}}\Delta P_k^{\mathrm{C}} \tag{4.13}$$

where P_k^{C} is the power generated from Ω_k^{C}

$$P_k^{\mathrm{C}} = \sum_{i\in\Omega_k^{\mathrm{C}}} P_i \tag{4.14}$$

And since the change of P_k^{C}, i.e., ΔP_k^{C}, is shifted from Ω_k^{C} to Ω_k^{R}, ignoring the variation of transmission loss after power shifting, there is

$$\Delta P_k^{\mathrm{C}} = \sum_{i\in\Omega_k^{\mathrm{C}}} P_i' - \sum_{i\in\Omega_k^{\mathrm{C}}} P_i \approx \sum_{j\in\Omega_k^{\mathrm{R}}} P_j - \sum_{j\in\Omega_k^{\mathrm{R}}} P_j' \tag{4.15}$$

where $\bullet'$ represents the corresponding variables before the power shifting.

After shifting the power, the change of $\rho_k(\mathrm{CCT} > \alpha_k)$ can be calculated from:

$$\Delta\rho_k(\mathrm{CCT} > \alpha_k) = \rho_k(\mathrm{CCT} > \alpha_k) - \rho_k'(\mathrm{CCT} > \alpha_k) \tag{4.16}$$

Thus, based on (4.12), the sensitivity of $\rho_k(\mathrm{CCT} > \alpha_k)$ to the active power shift from Ω_k^{C} to Ω_k^{R} can be estimated by:

$$\mathfrak{s}_k = \frac{\partial\mathcal{H}_k\left((\boldsymbol{x}_{sol},\boldsymbol{y}_{sol}),\Omega^{\mathrm{L}},\boldsymbol{\zeta},\widetilde{\boldsymbol{u}},\boldsymbol{\varepsilon},T,P_k^{\mathrm{C}}\right)}{\partial P_k^{\mathrm{C}}} \approx \frac{\Delta\rho_k(\mathrm{CCT} > \alpha_k)}{\Delta P_k^{\mathrm{C}}} \tag{4.17}$$

Based on the assumed local quasi-linear relationship, to achieve the stability level required (4.6), $\forall\, k \in \Omega^{\mathrm{IM}}$, the objective amount of active power $\Delta P_k^{\mathrm{C,obj}}$ to be shifted from Ω_k^{C} to Ω_k^{R} is calculated by:

$$\Delta P_k^{\mathrm{C,obj}} = \frac{\beta_k - \rho_k(\mathrm{CCT} > \alpha_k)}{\mathfrak{s}_k} \tag{4.18}$$

and then the dispatching plan against the faults is:

$$\forall\, k \in \Omega^{\mathrm{IM}}, \qquad \sum_{i\in\Omega_k^{\mathrm{C}}} P_i' - \sum_{i\in\Omega_k^{\mathrm{C}}} P_i \geq \Delta P_k^{\mathrm{C,obj}} \tag{4.19}$$

Thus, the probabilistic stability constraints are transformed from (4.6) to (4.19), and are added to the conventional OPF formulations, as shown in (4.1)–(4.4). Finally, the OPF with PTSCs is solved, and the dispatching solution is updated. In this way, the power adjustment demand $\Delta P_k^{\mathrm{C,obj}}$ $\forall\, k \in \Omega^{\mathrm{IM}}$ can be satisfied at the lowest total increment of the operating cost.

To correct the error from the quasi-linear relationship and avoid unnecessary over-stabilized situations (i.e., unnecessary cost increases due to excessive compliance with the PTSCs), the calculation and the shifting of $\Delta P_k^{\mathrm{C,obj}}$ are executed iteratively. The checking-and-rescheduling procedures are conducted until the expected dispatching solution is found.

4.3.5 The Overall Process of the Proposed Solution Algorithm

The overall process of the proposed solution framework is illustrated in Figure 4.5, where m is the iteration number, and $\mathcal{M}$ is the maximum allowed number of iterations. Before starting the iteration loop, the parameters for dispatching should be first set (step ① in the figure), followed by the generation of the Ω^{w} according to the hour-ahead PIs of each WPP (step ②). At each iteration, the dispatching solution $(\boldsymbol{x}_{sol}, \boldsymbol{y}_{sol})$ is first updated, followed by the generation of the Ω^{OP} and $\Omega^{\mathcal{L},\mathrm{op}}$ (step ④). Next, the $\Omega^{\mathrm{CCT,IM}}$ is predicted for $\Omega^{\mathcal{L},\mathrm{op}}$ by the trained model, and the values of $\rho_k(\mathrm{CCT} > \alpha_k)$ $\forall\, k \in \Omega^{\mathrm{IM}}$ are calculated (step ⑤), as introduced in Section 4.3.3. Then, the constraints in (4.6) are checked (step ⑥). If all of the constraints in (4.6) are satisfied at the first iteration, i.e., the conventional OPF solution already meets the PTSCs, then no further action is needed (steps ⑦ to ⑨). Otherwise, the current plan needs to be rescheduled against instabilities or to avoid unnecessary over-stabilized situations. In this regard, $\forall\, k \in \Omega^{\mathrm{IM}}$, (4.14)–(4.19) are carried out to convert the PTSCs into a set of linear inequality constraints (step ⑫), during which the $\mathfrak{s}_k$ in (4.17) can be easily calculated from two successive iterations. Specifically, at the first iteration, no power has been shifted from Ω_k^{C} to Ω_k^{R}; so, (4.14)–(4.18) are inexecutable. Thus, $\Delta P_k^{\mathrm{C,obj}}$ $\forall\, k \in \Omega^{\mathrm{IM}}$ can be initialized to $\varphi \sum_{i\in\Omega_k^{\mathrm{C}}} P_i$ (step ③)., where φ is a value between 0 and 1. The transformed linear inequality constraints (4.19) are then created (if $m = 2$) or updated (if $m > 2$), and added to the OPF formulation.

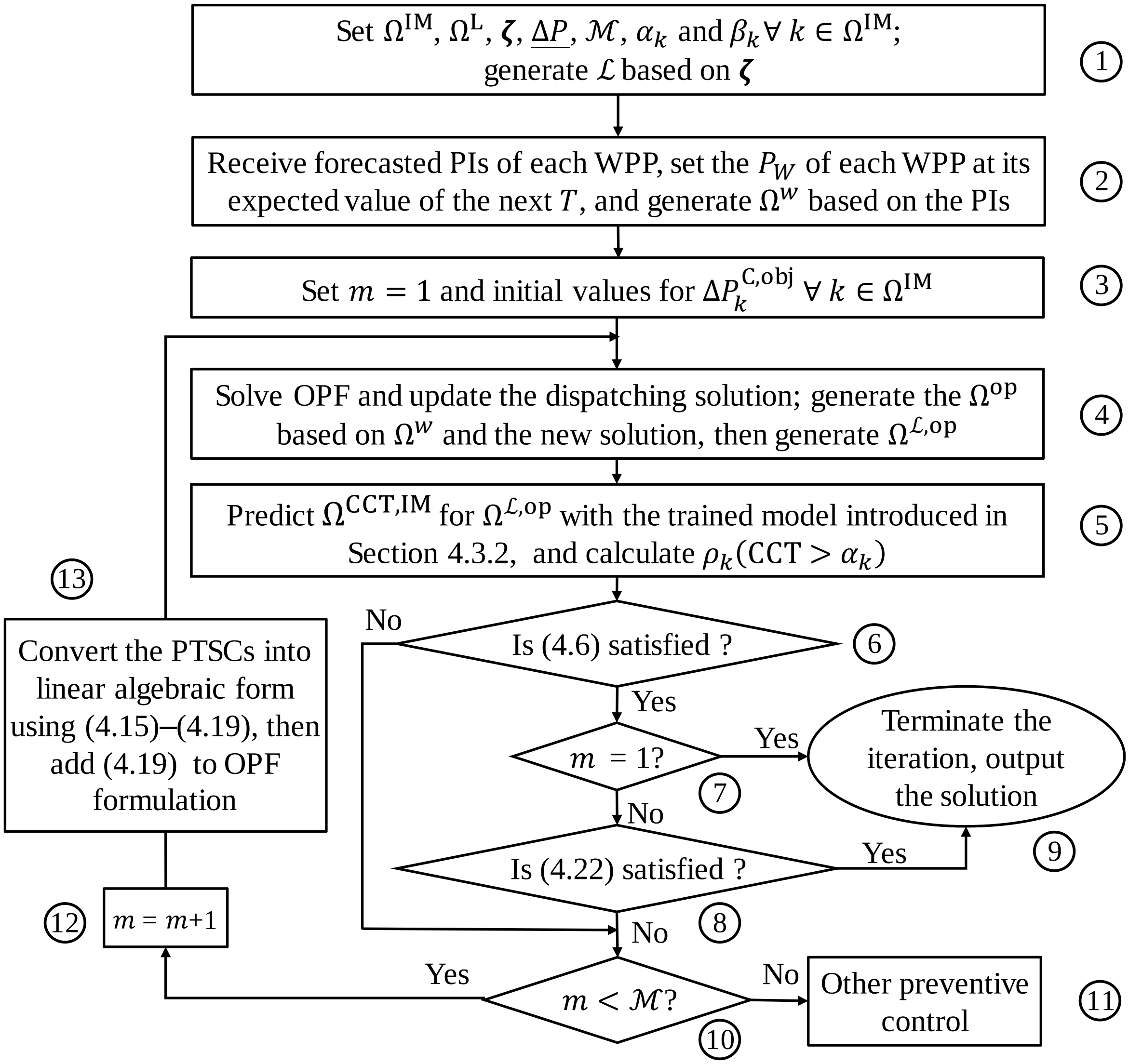

Figure 4.5: Flowchart of the proposed framework.

Notably, for over-stabilized situations, which may happen during iterations:

$$\exists\ \rho_k(\text{CCT} > \alpha_k)\ > \beta_k\ \ \forall k \in \Omega^{\text{IM}} \tag{4.20}$$

a negative $\Delta P_k^{\text{C,obj}}$ would be obtained from (4.18) for corresponding k. Then, according to (4.19), the power output constraints for the SGs in Ω_k^{C} can be relaxed to allow some active power shift from Ω_k^{R} back to Ω_k^{C}; thus, a more cost-saving dispatching result can possibly be found.

The iteration is terminated when all constraints in (4.6) are satisfied and, at the same time, the maximum power output change in all SGs between the current and last iteration is less than a threshold value $\underline{\Delta P}$:

$$\Delta P_i^{\max} \leq \underline{\Delta P} \tag{4.21}$$

where

$$\Delta P_i^{\max} = \max| P_i' - P_i \ | , \forall i \in \Omega^{\text{gen}} \tag{4.22}$$

Therefore, the dispatching plan is finalized when both (4.6) and (4.21) are satisfied. Otherwise, the flowchart enters the next iteration, the dispatching solution is updated, and the new iteration proceeds, as shown in Figure 4.5.

4.4 Test and Results

The described framework is realized by a Python-based interface that calls PSS/E software to conduct dynamic simulations, save the data for training and testing of the prediction model; the prediction model is trained using the *scikit-learn* 0.20.4 package [124] in Python 2.7.15. Next, the interface implements the proposed procedure, during which MATPOWER [123] is called to solve the OPF with PTSCs at each iteration.

The modified IEEE 16-machine 68-bus system introduced in Section 2.4.1 is used to perform the simulations. The cost function coefficients of each generator in the system are given in [132] and Appendix C. Each installed capacity of the nine WPPs in this system is 800 MW; thus, the wind power installed capacity accounts for 40% of the total load. The computer used in the simulations featured an Intel 3.4-GHz CPU with 16 GB of RAM.

4.4.1 Training and testing of the (CCT, IM) Prediction Model

4.4.1.1 Databased generation

Database generation is required to train the prediction models. The training database is obtained from Monte Carlo TDSs. In this regard, reasonable uncertainty models, including outputs of WPPs and load levels, are essential. In practice, these uncertainty models can be statistically estimated from the corresponding historical observations. In this study, the PDFs of the generation of each WPP are estimated using Gaussian kernels in a non-parametric way using hourly historical data from [77]. The same method is applied to load where the historical data are retrieved from [120]. Thus, before running a dynamic simulation for a specific scenario, the hour of a day is sampled randomly, and then load level and WPP outputs are sampled from their respective PDFs for the sampled hour. Then, the SG powers are randomly dispatched in their respective output limits, such that the total demand and generation are balanced. The faults are assumed to be permanent and are cleared by switching off the faulted lines. Moreover, faults are randomly applied to transmission lines for each simulation. Only three-phase faults are considered in this study, though the proposed method is also capable of handling other fault types.

In addition, 60,000 cases are generated by running TDSs. Given the fault clearing time of a breaker is typically less than 0.2 s [133], the range of CCT considered in the simulation is between 0 and 0.25 s; i.e., a fault with a CCT that is larger than 0.25 s can be considered safe as it can be cleared by a breaker before the system reaches a critical condition. This setting can help save simulation time during the database generation; any other ranges can be used without loss of generality. For each case, 58 features as introduced in Table 4.1 are used for model training, and the (CCT, IM) of the case is used as the target labels.

It is worth noting that, as a by-product of the model training stage, eight prominent IMs of the system are detected and listed in Table 4.2. Thus, the set of IMs, $\Omega^{\mathrm{IM}} := \{k = 1, 2, \dots, 8\}$, and the system will be dispatched against these IMs in the following subsection. To keep dispatch more focused on critical lines, only fault lines with instability-triggering records during the TDSs are selected to recompose the Ω^{L}, as listed in Table 4.2.

4.4.1.2 Training and Testing

To adequately assess the performance of the model, 5-fold cross-validation is applied. N-fold cross-validation (N= 2, 3, 4, 5…) is widely used in the assessment of the ML-based models. The process of 5-fold cross-validation is illustrated in Figure 4.6: first, the database is shuffled then partitioned into five equal-sized subsamples, and a single subsample is retained as the validation data for testing the model, and the remaining four subsamples are used as training data. The cross-validation process is then repeated five times. Thus, the performance of the model is tested on the test data that are completely separate from the training set, and the average accuracy of the 5-fold cross-validation is reported in Table 4.3.

Table 4.2: IMs to be prevented and the fault lines considered in dispatching.

k	IM details ($\Omega_k^{\mathrm{C}}/\Omega_k^{\mathrm{R}}$)	Ω^{L}
1	(SG16)/(SG1-15)	(lines between bus-bus) 18-42, 18-49, 18-50, 21-22, 21-68, 25-26, 25-54, 26-27, 26-28, 26-29, 27-37, 27-53, 28-29, 32-33, 37-52, 37-68, 40-41, 41-42, 45-51, 50-51
2	(SG14-16)/(SG1-13)	
3	(SG6-7)/(SG1-5, SG8-16)	
4	(SG9)/(SG1-8,SG10-16)	
5	(SG8-9)/(SG1-7, SG10-16)	
6	(SG11)/(SG1-10, SG12-16)	
7	(SG4-7)/(SG1-3, SG8-16)	
8	(SG14)/(SG1-13, SG15-16)	

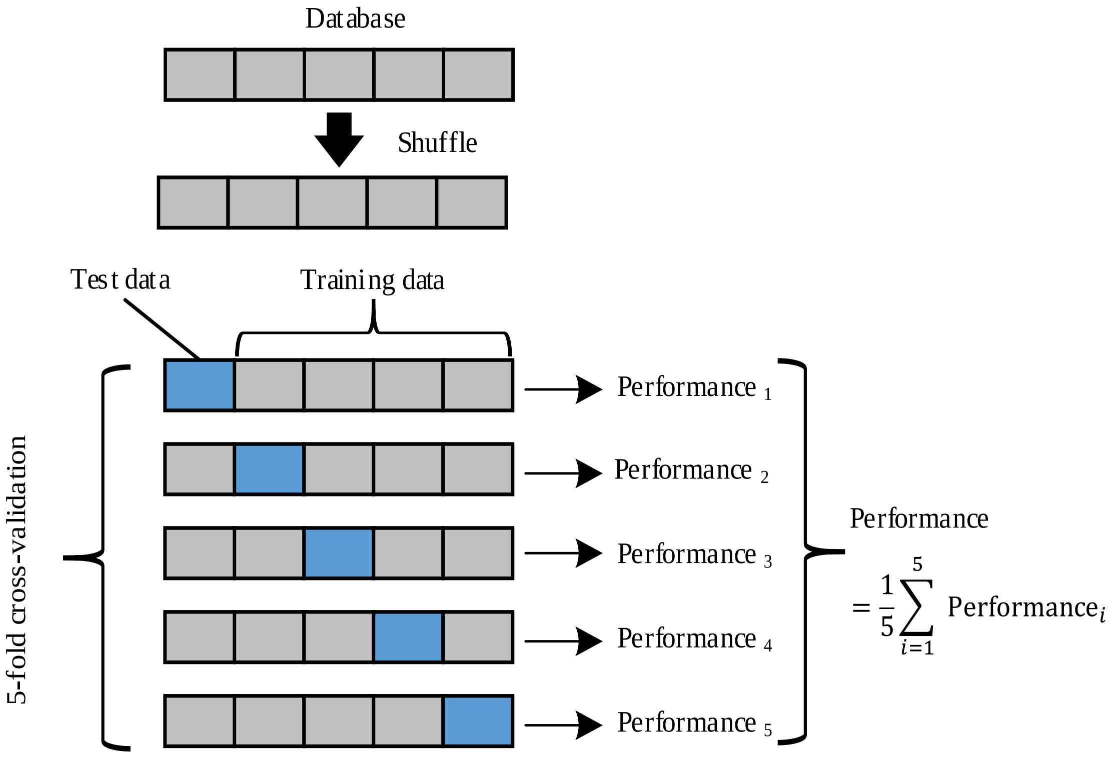

Figure 4.6: Assess the performance of the model by 5-fold cross-validation.

The time consumption for database generation and test accuracy of the prediction model are reported in Table 4.3, where the test accuracy includes the mean squared error (MSE) of CCT prediction and the classification accuracy of IM prediction. The results validate the high accuracy of the trained model with respect to predictions of CCT and IM.

Table 4.3: Time consumption and performance of the prediction model.

Database generation	Prediction for CCT	Prediction for IM
66406 s	MSE: 1.3440×10^{-4}	Accuracy: 99.17%

In addition, to reveal the influences of each feature on prediction, Tables 4.4 and 4.5 report the importance scores of each feature for predicting CCT and IM for the IEEE 68-bus system, respectively. The importance score refers to the usefulness of a specific feature at predicting the target; the calculation method of the scores can be found in [124]. The features investigated include pre-fault rotor angles, the active and reactive power output of each SG, active power output of each WPP, and fault location. The two tables show that all the selected features contribute to the prediction in different degrees. Note the 20 fault lines in the two tables correspond to the 20 fault lines in Table 4.2. For a better illustration, the feature importance is summed by type and illustrated in Figures 4.7 (a) and (b). Figure 4.7 (a) shows that the fault location makes most of the contribution to the training of the CCT prediction model, followed by pre-fault rotor angles, active power output from each SG and each WPP, and reactive power output from each SG. This makes sense because, in addition to the fault location, the value of CCT largely depends on system operating conditions and fault conditions. Figure 4.7 (b) shows that fault locations dominate the contribution for IM prediction, while other features also make noteworthy contributions. That is because the type of the triggered IM largely depends on fault conditions; at the same time, a specific location may trigger different IMs under different system operating conditions. It might be helpful to mention that other features such as terminal voltage magnitudes of each SG are tested as well; however, it is empirically seen in simulations that their contribution to the prediction is limited compared to the features selected. The trained model will be applied to dispatching operations in the next section.

Table 4.4: Normalized importance scores of each feature for predicting CCT.

δ_1	δ_2	δ_3	δ_4	δ_5	δ_6	δ_7	δ_8
0.00624	0.00451	0.0031	0.00257	0.00186	0.00676	0.00483	0.00645
δ_9	δ_{10}	δ_{11}	δ_{12}	δ_{13}	δ_{14}	δ_{15}	δ_{16}
0.01091	0.07925	0.04944	0.01526	0.02643	0.01068	0.01303	0
P_1	P_2	P_3	P_4	P_5	P_6	P_7	P_8
0.00768	0.00309	0.00684	0.00916	0.00701	0.01688	0.01713	0.00514
P_9	P_{10}	P_{11}	P_{12}	P_{13}	P_{14}	P_{15}	P_{16}
0.02628	0.00422	0.00703	0.00771	0.00384	0.04853	0.005	0.0197
Q_1	Q_2	Q_3	Q_4	Q_5	Q_6	Q_7	Q_8
0.0019	0.00149	0.0015	0.00113	0.00172	0.00311	0.00183	0.00231
Q_9	Q_{10}	Q_{11}	Q_{12}	Q_{13}	Q_{14}	Q_{15}	Q_{16}
0.00238	0.00157	0.00167	0.00092	0.00155	0.00309	0.00333	0.00419
P_{W1}	P_{W2}	P_{W3}	P_{W4}	P_{W5}	P_{W6}	P_{W7}	P_{W8}
0.03601	0.00981	0.0208	0.0057	0.00906	0.00717	0.01372	0.00711
P_{W9}	Fault_line$_1$	Fault_line$_2$	Fault_line$_3$	Fault_line$_4$	Fault_line$_5$	Fault_line$_6$	Fault_line$_7$
0.00476	0.02989	0.02545	0.03700	0.03145	0.01671	0.0037	0.00804
Fault_line$_8$	Fault_line$_9$	Fault_line$_{10}$	Fault_line$_{11}$	Fault_line$_{12}$	Fault_line$_{13}$	Fault_line$_{14}$	Fault_line$_{15}$
0.0043	0.0083	0.01092	0.00304	0.00351	0.01067	0.01079	0.00496
Fault_line$_{16}$	Fault_line$_{17}$	Fault_line$_{18}$	Fault_line$_{19}$	Fault_line$_{20}$			
0.00675	0.06121	0.02613	0.05157	0.06100			

Table 4.5: Normalized importance scores of each feature for predicting IM.

δ_1	δ_2	δ_3	δ_4	δ_5	δ_6	δ_7	δ_8
0.00158	0.00043	0.00029	0.00131	0.00023	0.00108	0.00019	0.0004
δ_9	δ_{10}	δ_{11}	δ_{12}	δ_{13}	δ_{14}	δ_{15}	δ_{16}
0.00231	0.00747	0.00564	0.0011	0.00323	0.00215	0.00428	0
P_1	P_2	P_3	P_4	P_5	P_6	P_7	P_8
0.00677	0.00094	0.00101	0.00005	0.00254	0.00667	0.01245	0.00077
P_9	P_{10}	P_{11}	P_{12}	P_{13}	P_{14}	P_{15}	P_{16}
0.04921	0.00044	0.00085	0.00072	0.00119	0.01277	0.00125	0.00117
Q_1	Q_2	Q_3	Q_4	Q_5	Q_6	Q_7	Q_8
0.00035	0.0001	0.00049	0.00144	0.00025	0.00233	0.00081	0.00145
Q_9	Q_{10}	Q_{11}	Q_{12}	Q_{13}	Q_{14}	Q_{15}	Q_{16}
0.00406	0.00352	0.00229	0.00017	0.00032	0.00019	0.00161	0.04969
P_{W1}	P_{W2}	P_{W3}	P_{W4}	P_{W5}	P_{W6}	P_{W7}	P_{W8}
0.02638	0.00181	0.08331	0.0004	0.00057	0.00066	0.00113	0.0018
P_{W9}	Fault_line$_1$	Fault_line$_2$	Fault_line$_3$	Fault_line$_4$	Fault_line$_5$	Fault_line$_6$	Fault_line$_7$
0.00119	0.11134	0.0663	0.11011	0.01701	0.00675	0.00384	0.03326
Fault_line$_8$	Fault_line$_9$	Fault_line$_{10}$	Fault_line$_{11}$	Fault_line$_{12}$	Fault_line$_{13}$	Fault_line$_{14}$	Fault_line$_{15}$
0.01794	0.03606	0.0408	0.00341	0.00094	0.01718	0.10965	0.00467
Fault_line$_{16}$	Fault_line$_{17}$	Fault_line$_{18}$	Fault_line$_{19}$	Fault_line$_{20}$			
0.01100	0.01137	0.03352	0.00874	0.03919			

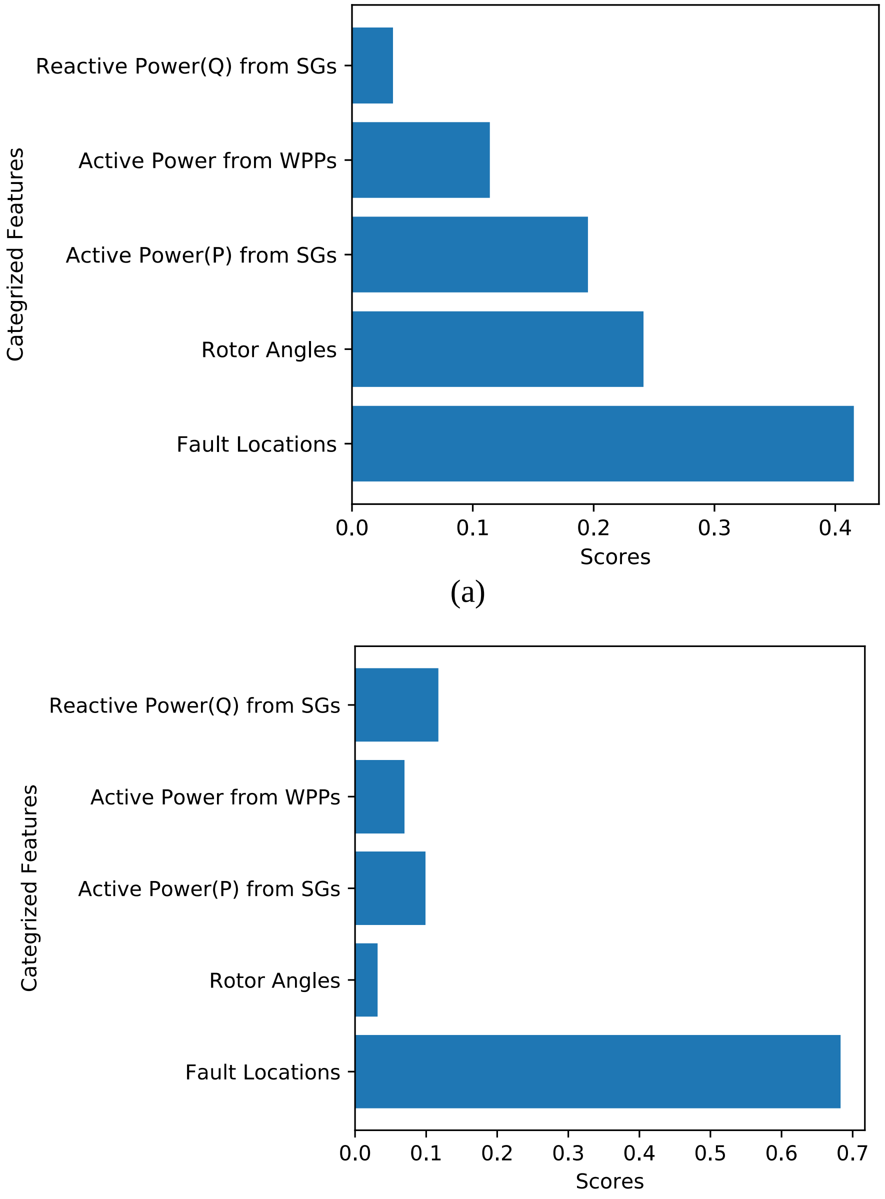

(a)

(b)

Figure 4.7: Importance scores of each categorized feature for predicting (a) CCT and (b) IM for the IEEE 68-bus system.

4.4.2 Test of the Proposed Framework

4.4.2.1 Setting of Parameters

The Ω^{IM}, Ω^{L}, $\boldsymbol{\zeta}$, $\underline{\Delta P}$, $\mathcal{M}$, α_k and $\beta_k \forall\, k \in \Omega^{\mathrm{IM}}$, and hour-ahead PIs for each WPP are required to conduct the test, as shown in steps ①–② in Figure 4.5. The settings of Ω^{IM} and Ω^{L} have been introduced in Section 4.4.1. The $\boldsymbol{\zeta}$ is set to uniform distribution, and thus the $\mathcal{L}$ is set equal to the Ω^{L} in this situation. $\underline{\Delta P}$ is set at 5 MW, which is 0.1% of the upper output limit of the largest SG in the system; $\mathcal{M}$ is set at 10. However, these parameters can be set to any other values without loss of generality. α_k and β_k $\forall\ k \in \Omega^{\text{IM}}$ are listed in Table 4.6. The above settings can be adjusted according to different dispatching requirements. Note that β_k is not set at 100% $\forall\ k \in \Omega^{\text{IM}}$ because this study is concerned with a probabilistic system in which stochastic factors in a power system can affect transient stability. In this regard, the stability level is analyzed from a probabilistic point of view. Setting the probabilistic stability security level at 95% means that after the power dispatch, if a fault occurs, considering uncertainties in the system, the probability of the CCT is greater than the threshold value should no less than 95%. On one hand, considering that the occurrence of a fault is generally a small probability event, setting excessively high probabilistic stability levels (e.g., 100%) against all possible faults may lead to an unnecessary increase in operating costs. Therefore, in the simulations, the security level at 95% seems a reasonable trade-off between economics and stability. On the other hand, the system operators can also use the proposed method to set the probabilistic transient stability level at different values (e.g., 90–100%) based on practical requirements.

Table 4.6: α_k and β_k set for dispatching.

k	1	2	3	4	5	6	7	8
α_k (s)	0.10	0.10	0.20	0.15	0.15	0.16	0.20	0.15
β_k (%)	95 $\forall\ k \in \Omega^{\text{IM}}$							

In addition, to set the assumed hour-ahead PIs for all WPPs in the modified IEEE 68-bus system, nine sets of hourly wind power data with a 5-minute resolution are selected from [77], and then a prediction interval for each data series is produced based on ±10% of the recorded value. The selected data and the corresponding PI curves are shown in Table 4.7 and Figure 4.8, respectively. Following that, 1200 wind power generation scenarios $\Omega^{w}$are generated, i.e., 100 scenarios are randomly sampled every 5 minutes in the dispatching time interval based on the PIs.

So far, the simulation parameters have been set (steps ①–② in Figure 4.5). Subsequently, the procedures in the proposed framework proceed until the terminate condition is met.

Table 4.7: Selected one-hour wind power data.

WPP	Selected time period (MM/DD/YY hr:min)	Output*
1	01/06/19 00:25–01:25	475.81 MW
2	03/25/19 21:10–22:10	366.85 MW
3	05/25/18 23:25–24:25	472.82 MW
4	10/28/18 16:50–17:50	322.72 MW
5	11/28/17 16:50–17:50	551.41 MW
6	11/20/17 15:55–18:55	527.91 MW
7	02/17/16 20:20–21:20	330.90 MW
8	03/06/16 13:50–14:50	323.31 MW
9	10/10/16 00:50–01:50	321.97 MW

*Expected (average) output of each WPP in the following hour.

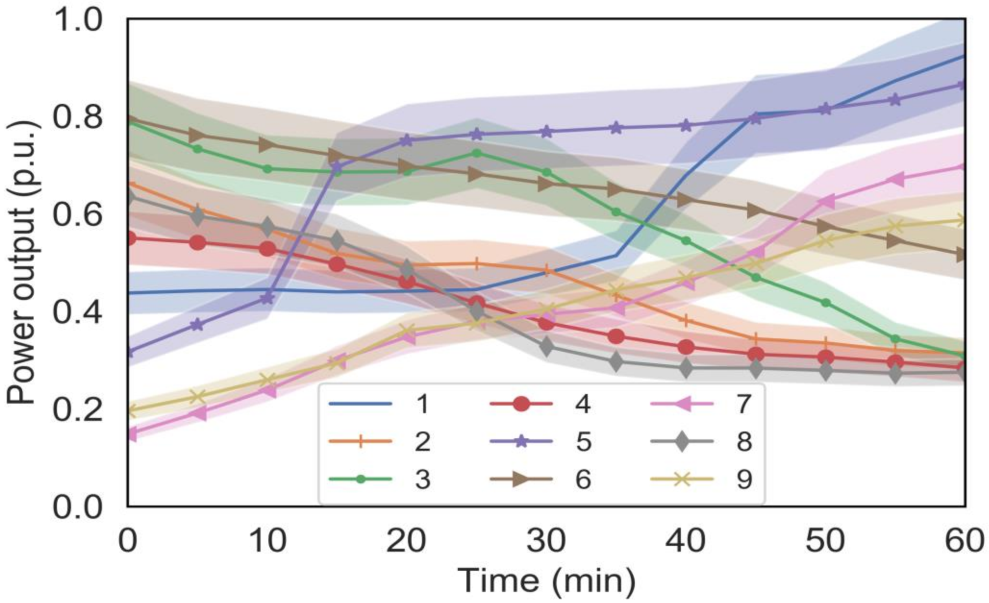

Figure 4.8: Hour-ahead wind power PI for each WPP.

4.4.2.2 Testing Results

Tables 4.8 and 4.9 list the values of $\rho_k(\mathrm{CCT} > \alpha_k)\ \forall\ k \in \Omega^{\mathrm{IM}}$ and corresponding dispatching solution that obtained from the proposed method at each iteration, respectively. It is worth noting that the solution of the first iteration, solved by conventional OPF, does not satisfy the PTSCs. The expected dispatching solution is found after eight iterations using the proposed method, during which the values of $\rho_k(\mathrm{CCT} > \alpha_k)\ \forall\ k \in \Omega^{\mathrm{IM}}$ increase and finally meet the security requirements (i.e., 95%). Notably, the operating cost of the proposed method only increased by 3.26% compared to OPF, as shown in Table 4.9.

The results demonstrate that using the assumed sensitivity in (4.17) is feasible for solving the power-dispatching problem considering PTSCs. In addition, the results show that the proposed method can handle unnecessary over-stabilized situations, e.g., in Table 4.8, the values of the $\rho_k(\mathrm{CCT} > \alpha_k)$ for k= 2, 4, 5, and 6 at the 4th iteration excessively satisfy the β_k, and this issue is alleviated in the following iterations. Accordingly, the operating cost decreases from 110.31 k$/h to 110.11 k$/h, as shown in Table 4.9.

Further, Figure 4.9 compares the probability distributions of CCT $\forall\ k \in \Omega^{\mathrm{IM}}$ before and after applying the proposed method. Specifically, the non-violation areas under each dashed curve correspond to the column values of the first iteration in Table 4.8, and the non-violation areas under each solid curve correspond to the column values of the 8th iteration in Table 4.8. Figure 4.9 shows that the violation areas are greatly reduced by applying the proposed method.

Table 4.8: Values (%) of $\rho_k(\mathrm{CCT} > \alpha_k)$ at each iteration.

k	Iterations							
	1st	2nd	3rd	4th	5th	6th	7th	8th
1	54.56	59.76	99.21	99.99	99.99	99.99	99.99	**99.99**
2	74.96	76.27	83.60	96.80	96.15	95.02	94.52	**95.11**
3	64.71	70.77	93.31	93.23	94.85	95.23	95.31	**95.30**
4	84.05	92.47	95.72	95.43	95.15	95.12	95.09	**95.06**
5	79.61	85.62	98.03	97.04	95.71	95.22	95.31	**95.29**
6	18.61	99.99	99.99	99.99	99.84	99.85	99.69	**98.61**
7	78.31	89.07	96.31	94.46	96.00	96.31	96.61	**96.61**
8	45.85	60.42	82.38	92.57	94.04	94.20	95.04	**95.02**

Table 4.9: Active power output (MW) of each SG and operating cost at each iteration.

SG	Iteration							
	1st	2nd	3rd	4th	5th	6th	7th	8th
1	129.15	139.22	182.14	194.39	192.81	190.79	190.55	**190.42**
2	371.46	388.42	460.39	480.85	478.26	474.90	474.47	**474.26**
3	450.22	468.89	547.35	569.52	566.75	563.12	562.65	**562.41**
4	391.21	391.18	493.60	505.43	519.62	515.83	515.29	**514.81**
5	345.98	346.02	416.83	425.04	434.80	432.18	431.81	**431.48**
6	440.81	414.43	308.46	300.49	274.09	271.57	273.08	**273.51**
7	341.51	317.89	223.15	216.05	192.45	190.20	191.55	**191.93**
8	346.33	346.33	296.05	308.96	324.63	333.70	332.67	**332.45**
9	526.24	476.24	448.58	454.70	458.33	459.58	460.63	**461.41**
10	432.95	453.08	545.34	573.05	569.34	564.81	564.29	**564.01**
11	753.55	703.55	706.63	709.70	712.77	715.75	718.72	**721.61**
12	1177.89	1220.77	1419.97	1479.28	1471.15	1461.32	1460.06	**1459.49**
13	2549.21	2635.68	3039.01	3158.95	3142.43	3122.51	3119.96	**3118.82**
14	1299.66	1249.66	1099.95	1013.91	993.43	979.99	961.31	**962.17**
15	739.43	778.21	627.45	596.01	606.97	616.79	620.77	**620.47**
16	3859.35	3809.35	3259.84	3077.31	3127.83	3174.66	3190.11	**3188.83**
k$/h	106.63	106.74	109.08	110.31	110.32	110.14	110.12	**110.11**

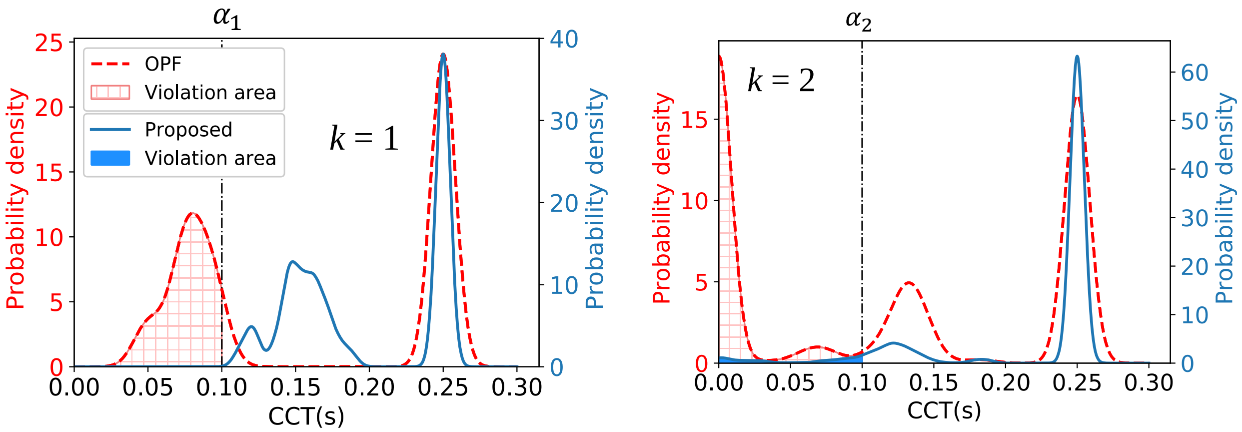

Figure 4.9: Comparison of the probability distribution of CCT $\forall\ k \in \Omega^{\mathrm{IM}}$.

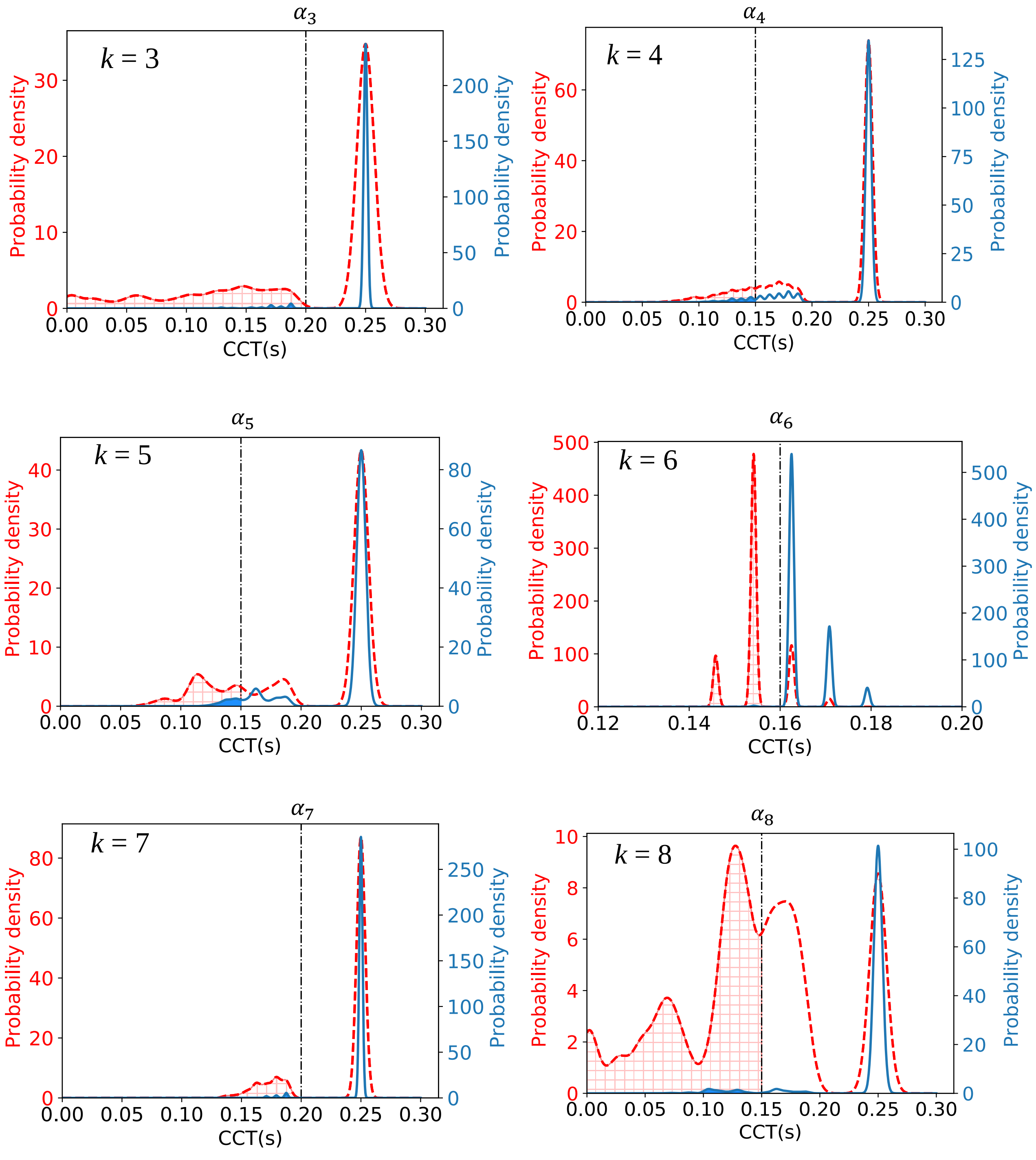

Figure 4.9 Continued

4.4.3 Validating the Results Using TDSs

To verify the dispatching results of the proposed method, two validation tests are carried out:

(1) The stability status of the dispatching results is tested by TDSs. For (1), Table 4.10 lists the validation results and shows that the values of $\rho_k(\mathrm{CCT} > \alpha_k)$ verified by TDSs are quite close to the values output from the proposed method (listed in the last column of Table 4.8). Although the values of the $\rho_k(\mathrm{CCT} > \alpha_k)$ for k =4 and 5 are slightly below 95% by 0.04 and 0.23%, respectively, the error is acceptable from the engineering point of view.

(2) The dispatching solution obtained from TDSs is also investigated, i.e., wherein the $\Omega^{\mathrm{CCT,IM}}$ in step ⑤ of Figure 4.5 is obtained from TDSs instead of the ML-trained model. For (2), the simulation results based on TDSs are listed in Table 4.11. It reveals the dispatching solution and stability levels are very close to those corresponding to the proposed method (listed in the last column of Tables 4.8 and 4.9). In addition, a comparison of the two methods in terms of time consumption and number of iterations is given in Table 4.12. Note that the consumed time in this table is for the online process, i.e., time starts when the system operator obtains information of hour-ahead uncertainties and ends when the expected dispatching solution is found. Notably, the proposed method is 186188/287 ≈ 648 times faster. This is because for each iteration, $\left|\Omega^{\mathcal{L},op}\right|$ =20×1200 =24,000 cases are simulated by TDSs given $|\Omega^{\mathrm{op}}| = 1200$ and $|\mathcal{L}| = 20$ ($\mathcal{L} = \Omega^{\mathrm{L}}$ in this test), which may take an extensive amount of time. In contrast, the proposed method only needs to solve the power flows to generate the Ω^{op}. Then, the $\Omega^{\mathrm{CCT,IM}}$ are accurately and rapidly predicted by the trained model. Thus, the calculation process takes less than 5 minutes, which is quite acceptable for hour-ahead operations.

The comparisons validate the good performance of the proposed framework in terms of practicability, searching for economical solutions, and computational efficiency. Given that most TSC-OPF works [70]–[74], [76], [82], [84] rely on TDSs and thus may have difficulty handling massive fault scenarios, the proposed method has more advantages for dealing with systems with high wind power penetration.

Table 4.10: Values (%) of $\rho_k(\mathrm{CCT} > \alpha_k)$ tested by TDSs.

k	1	2	3	4	5	6	7	8
Verified by TDSs	99.97	95.02	96.46	94.96	94.77	98.92	97.37	95.08

Table 4.11: Dispatching result and values of $\rho_k(\mathrm{CCT} > \alpha_k)$ based on TDSs.

Dispatching result (MW)								
SG	1	2	3	4	5	6	7	8
Output	192.14	477.02	565.44	518.34	433.91	283.68	201.02	297.02
SG	9	10	11	12	13	14	15	16
Output	449.43	567.28	720.73	1466.40	3132.73	969.38	617.19	3173.33
Total generation from SG: 14065.04 MW; Final operating cost: 110.20 k$/h								
Values of $\rho_k(\mathrm{CCT} > \alpha_k)$ for each IM								
IM	1	2	3	4	5	6	7	8
Value (%)	99.94	95.05	95.01	95.14	95.06	95.02	95.76	95.00

Table 4.12: Time consumption and number of iteration of two methods.

Method	Time consumed (s)	Iterations
TDS-based	186188	7
Proposed	287	8

To validate the local quasi-linear relationship in (4.13), the values of $\rho_k(\mathrm{CCT} > \alpha_k)$ with respect to the active power generated from Ω_k^{C} are reported in Figure 4.10. In this test, an IM ($k = 3$) is selected, where the Ω_k^{C} includes SG6 and SG7, and the α_k is set at 0.2 s. Note that the change in the active power of Ω_k^{C} is balanced by SGs in Ω_k^{R} during the simulations. Figure 4.10 shows that a local quasi-linear relationship exists between $\rho_k(\mathrm{CCT} > \alpha_k)$ and the active power generated from Ω_k^{C}. Similar simulation results can be obtained for other IMs.

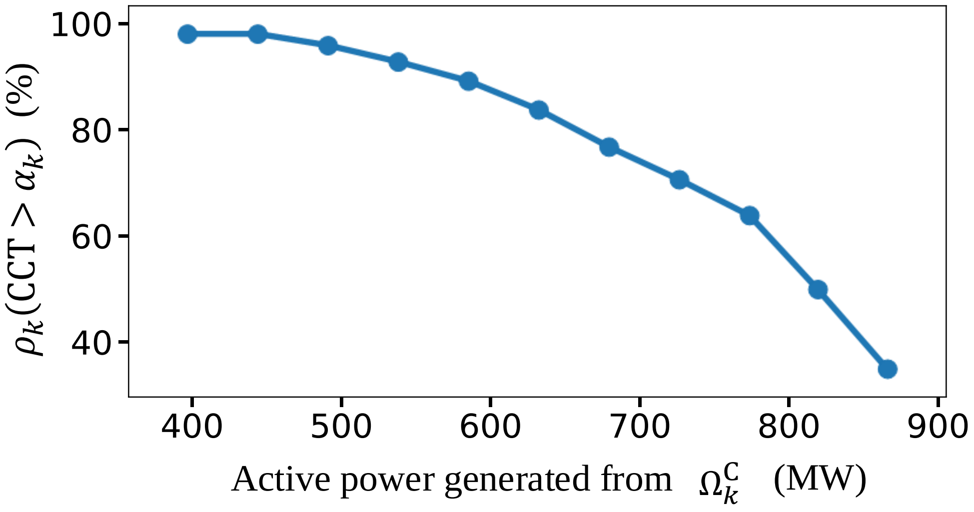

Figure 4.10: The value of $\rho_k(\mathrm{CCT} > \alpha_k)$ vs. the active power generated from Ω_k^{C}.

4.4.4 Comparison with a State-of-the-Art Method

To further validate the advantage of the proposed method, the dispatching solution is compared to that of a method reported in [84], in which the test scenarios of a robust dispatch for wind energy-integrated power networks against transient instability are dramatically reduced using Taguchi's orthogonal array. The results of the latter method are reported in Table 4.13.

Table 4.13: Dispatching result and values of $\rho_k(\mathrm{CCT} > \alpha_k)$ of the comparison method.

Dispatching result (MW)								
SG	1	2	3	4	5	6	7	8
Output	206.94	501.90	592.56	523.98	437.88	256.60	176.86	377.71
SG	9	10	11	12	13	14	15	16
Output	374.55	599.44	698.13	1534.98	3270.93	957.70	544.54	3000.00
Final operating cost: 111.91 k$/h								
Values of $\rho_k(\mathrm{CCT} > \alpha_k)$ for each IM								
IM	1	2	3	4	5	6	7	8
Value (%)	100.00	97.89	98.26	99.23	95.83	99.99	97.30	95.00

It can be seen that the robust dispatch method in [84] yields to a conservative solution, as most of the PTSCs (95%) are over-satisfied; thus, the operating cost reaches 111.91 k$/h. In contrast, the operating cost associated with the proposed method is 110.11 k$/h. Besides the economic advantages, another benefit of the proposed method is that it enables operators to set flexible probabilistic stability levels (e.g., 80~100%) to each IM that needs to be prevented.

4.4.5 Validation of the Framework on the IEEE 300-Bus System

The proposed method is also tested on the modified version of IEEE 300-bus system, which has 69 SGs, 304 transmission lines and 15 WPPs. The details of the system are introduced in Section 3.5.1. Specifically, the installed capacity of each WPP is 800 MW, therefore, the wind power installed capacity accounts for 50% of the total load.

4.4.5.1 Training and Testing of the (CCT, IM) Prediction Model

The training and testing processes described in Section 4.4.1 is applied to train the (CCT, IM) prediction model, during which 152,000 cases are generated by TDSs. The computational time for database generation is 187,163 s. Based on the testing results, the MSE of the prediction for CCT and the accuracy of the prediction for IM are 1.6107×10^{-4} and 99.39%, respectively, as shown in Table 4.14. The results confirm the high accuracy of the trained model.

Also, the importance scores of each feature for predicting CCT and IM for the modified IEEE 300-bus system are reported in Figure 4.11. Similar to Figure 4.7, it can be seen that fault location is of the highest importance for prediction while the other feature also make noteworthy contribution. The trained model is applied to the dispatching operations in the next section.

Table 4.14: Time consumption and performance of the prediction model for the modified IEEE-300 bus system.

Database generation	Prediction for CCT	Prediction for IM
187,163 s	MSE: 1.6107×10^{-4}	Accuracy: 99.39%

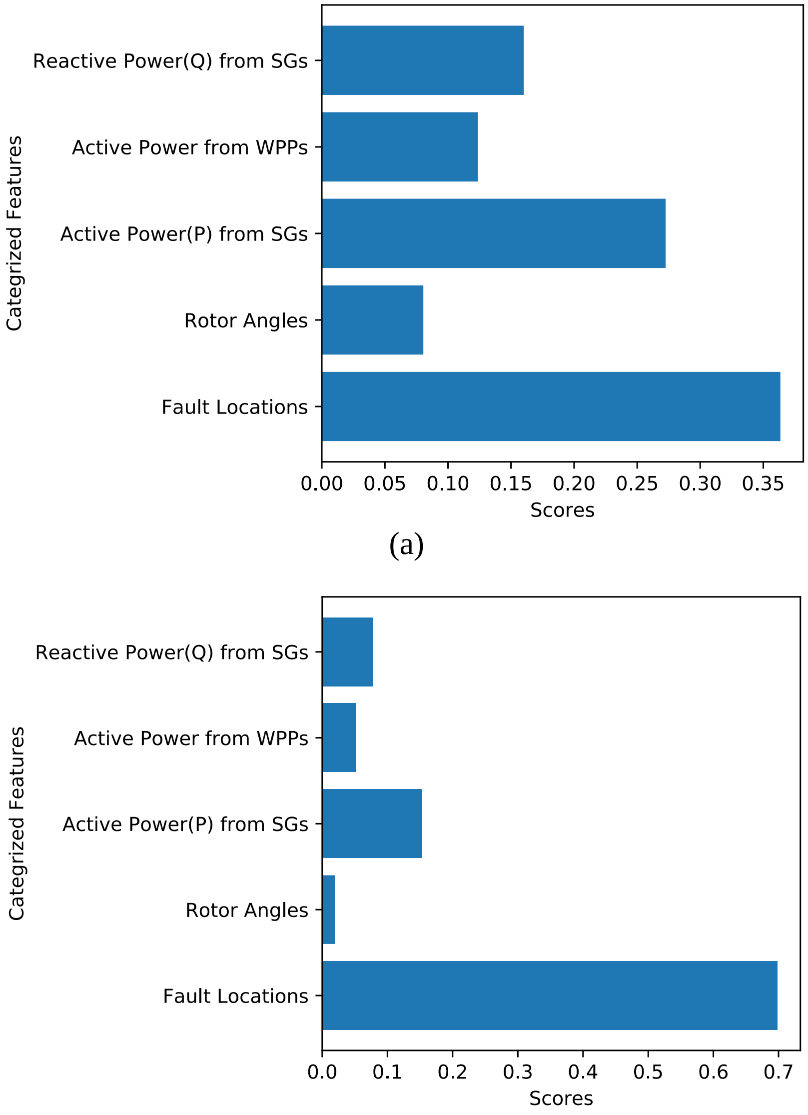

(a)

(b)

Figure 4.11: Importance scores of each categorized feature for predicting (a) CCT and (b) IM for the modified IEEE 300-bus system.

4.4.5.2 Testing Results

For the validation of the framework, nine IMs are selected, as listed in Table 4.15, in which the set of selected fault lines Ω^{L}, as well as α_k and β_k for dispatching, are also given. $\mathcal{M}$ is set at 15. In addition, the wind power datasets listed in Tables 4.7 and 4.16, which are selected from [77], are used to set the assumed hour-ahead PIs for all WPPs. The procedure for setting PIs and other testing parameters is the same as that in Section 4.4.2.

The results solved by OPF without considering the PTSCs and the proposed solutions are listed in Table 4.17, and the results based on TDSs are also given as a benchmark for comparison. Table 4.17 shows that the expected dispatching solution is achieved after 12 iterations utilizing the proposed method, in which the operating cost increased only by 1.12% with respect to the result of OPF. The table also shows that the final operating cost and stability levels of the proposed and TDS-based methods are very similar. Although the results of the proposed method are slightly over-stabilized in this case, it is 174675/549≈318 times faster. Remarkably, the prediction time for each iteration (15,600 cases) is revealed in Table 4.18. It can be seen that once the ML-based model is trained, it can make predictions rapidly for the preconceived fault scenarios. In fact, for the proposed method, most of the time consumed at each iteration is in solving power flows for generating Ω^{OP}. The results and comparison verify the effectiveness of the proposed method.

Table 4.15: Selected IM patterns, Ω^{L}, and the α_k and β_k set for dispatching.

k	IM details (Ω_k^{C})	α_k (s)	β_k (%)	Ω^{L}
1	(SG7166)	0.20	95	(lines between bus-bus) 62-64, 119-120, 119-121, 134-184, 140-182, 162-164, 162-165, 163-164, 165-166, 190-231, 191-192, 191-225, 214-215
2	All SGs except (SG63)	0.20		
3	(SG119)	0.15		
4	(SG119 and SG124)	0.15		
5	(SG185)	0.15		
6	(SG7139)	0.15		
7	(SG190)	0.15		
8	(SG191)	0.15		
9	(SG213, SG242, and SG243)	0.20		

Table 4.16: Selected one hour wind power data.

WPP	Selected time period (MM/DD/YY hr:min)	Output*
1	10/16/16 15:10–16:10	211.19 MW
2	11/28/17 16:50–17:50	308.34 MW
3	11/20/17 15:55–16:55	89.18 MW
4	03/24/15 04:35–05:35	491.56 MW
5	02/07/15 17:20–18:20	398.50 MW
6	08/29/15 05:35–06:35	186.07 MW

*Expected (average) output of each WPP in the following hour.

Table 4.17: Comparison of different methods.

IM	Value (%) of $\rho_k(\mathrm{CCT} > \alpha_k)$		
	OPF (m = 1)	Proposed	TDS-based
1	81.57	96.15	95.18
2	0.00	100	100
3	42.85	95.92	95.53
4	15.43	100	99.68
5	1.57	100	100
6	40.60	95.71	95.11
7	27.69	95.29	95.04
8	0.00	96.06	95.13
9	14.64	96.69	95.38
Comparative item	OPF (m = 1)	Proposed	TDS-based
k$/h	521.72	527.56	527.07
Time consumed (s)	–	549	174675
Iterations	–	12	9

Table 4.18: Prediction time of the trained model at each iteration (15,600 Cases).

	CCT	IM
Time consumed (s)	4.91	0.11
Total (s)	5.02	

4.5 Discussions

This section further discusses the possible problems and countermeasures of the proposed method in practice

- Topology changes of a power system during its operating horizon

The proposed method is capable of addressing possible topology changes in a power system. There are three approaches to realize this:

The first approach is to consider topological changes while generating the training database that results in prediction models that can predict stability for various system layouts. For example, in the studies reported in [17], offline dataset is generated in a way that 85%, 14%, and 1% of the whole cases are related to nominal-power network topology, N−1, and N−2 working conditions, respectively. This approach can help maintain the prediction accuracy of the model when the topology of the system is changed slightly, basically covering the regular utility-known maintenance outages.

The second approach is to consider the change in the topology during the generation of the training database and save the topology information as a feature. It should be noted that this can increase the size of the training data, the complexity of the prediction model, and the raining time. As a result, more complex machine learning algorithms like deep learning might be required.

The third approach is to assign a prediction model to each possible topology structure of the system. This approach can result in more accurate prediction models compared to the first method, and the parallel computation allows to train multiple prediction models in a reasonable time frame. This method is adopted in [58], proved a superior performance in handling the topology changes of networks. This adjustment can also be used in the proposed method in a straightforward manner.

- Scalability of the proposed method

Generally, the size of the database required to train the prediction model would increase with the growth of system complexity. Fortunately, considering the generation of the database and the training process are carried out offline, the calculation time of online operation is barely affected. In addition, the parallel computing technique can significantly accelerate the database generation and training process. In terms of the online application, the increase in system scale has a limited impact on online operation time. For example, in this study, it takes the trained model about 0.7 s and 3.3 s to predicted 10,000 cases for IEEE 68- and 300-bus test systems, respectively. Therefore, this should not be a problem for the proposed method.

4.6 Summary

The challenges of power dispatch for high wind power-integrated systems considering PTSCs are presented and a novel method is proposed. To overcome the necessity of running massive

TDSs, a highly efficient ML-based technique is incorporated to predict CCT and IMs for possible fault scenarios. Next, a set of IM-categorized PTSCs are constructed, and different probabilistic stability standards are set against different faults. A method to convert the PTSCs into explicit dispatching constraints is also presented, such that the constraints are embedded into conventional OPF formulation for dispatch rescheduling. The method is compatible with various types of uncertainties and dynamic models in power systems. The effectiveness of the proposed method is validated on two IEEE test systems, demonstrating superior performance in terms of providing high-quality solutions and computational efficiency. The proposed method is much faster than a TDS-based method, while the solution is quite close (less than 0.1% difference in operating cost).

The main contributions of this chapter are threefold:

(1) An ML technique is utilized, for the first time, to solve the power dispatch problem considering PTSCs. Compared to the existing methods, the proposed method can rapidly evaluate the stability status for a system considering uncertainties without reducing the test scenarios,

(2) IM-categorized PTSCs are formulated to facilitate the dispatching plan against various faults considering uncertainties, and enables operators to set flexible probabilistic stability levels for each IM to be prevented, and

(3) The sensitivity of the probabilistic level of CCT to the active power generated from the critical generators is proposed, whereby the PTSCs can be converted into a set of explicit dispatching constraints; thus, the dispatch is rescheduled to ensure the probabilistic stability requirements are met at an economical operating cost.

5 Conclusions and Suggestions for Future Work

5.1 Conclusions

This thesis addresses the transient stability problem of power systems with high wind power penetration from two perspectives: rapid prediction and preventive dispatch.

In this regard, the challenges of transient stability prediction for wind power-integrated power systems are analyzed. In response, a novel prediction approach is proposed taking advantage of the ML technique and the newly defined *SI* vector. Specifically, the *SI* vector is served as an input feature, and an ensemble learning technique is applied to train a prediction model. The numerical test reveals the superiority of the *SI* vector for stability prediction. Notably, with increasing wind power penetration, the proposed method has a distinct advantage in terms of accuracy compared to other recently published methods. The reason is that each *SI* vector correlates with a set of stability margins of a WPP-connected power system. Therefore, as a feature, it is more informative and discriminative. Furthermore, it has been demonstrated that the proposed are quite robust to the changes in the system typology.

Moreover, this study conducted in this thesis introduced the difficulties in preventive dispatch for high wind power-integrated electrical systems, and accordingly, an ML-incorporated preventive probabilistic transient stability power dispatch method is developed. Specifically, the proposed method can rapidly evaluate the stability status of a system for a massive possible operating scenarios, and reschedule the power generation to ensure the probabilistic stability requirements of the system are met at an economical operating cost. The proposed approach is tested on two IEEE test systems with a high level of wind power penetration, reporting high computational efficiency and high-quality solutions. Remarkably, compared to the existing methods, the proposed approach enables operators to set flexible probabilistic stability requirements for different IM to be prevented. The proposed method can also be flexibly applied to power systems of different scales, and systems with different types of renewables and dynamic models.

5.2 Suggestions for Future Works

The existing ML applications in the power systems have brought a brand new perspective to the entire industry, and huge potential still remain to be further explored. The thesis introduced two examples of incorporating ML-techniques into power system against rotor angle instability, further study can be extend to improve the accuracy, efficiency and general applicability of the methods, and more importantly, explore how ML-techniques can be further and better applied to solve stability-related and other issues in power systems. For future extension of this study, the following research works are recommended:

- Explore more effective ML-incorporated methods for rotor angle prediction

For the performances of all existing perdition models, there is still room for improvement in the accuracy and robustness. This may be addressed from two ends, including 1) explore a more effective feature for prediction, and 2) build more problem-specific ML algorithm structures. Specifically speaking, 1) relates to feature selection and feature extraction studies. It requires researchers to fully consider the physical characteristics of power systems and explore the feature that better reflect the problem. In addition, it may be necessary to develop different feature extraction algorithms for power systems with different types or even proportions of power electronic-based components (e.g., HVDC, FACTS devices, battery storage system, etc.). For 2), directly introduce the existing ML-algorithms to train a model may restrict the prediction performance. In fact, the prediction performance can be further improved by modifying and reorganizing the ML algorithm structure according to the nature of the problem. The work in this area including the building of neural network structure, design of loss function and training process, etc.

- Rapid remedy control strategies

Chapters 2 and 3 discussed the method of transient stability prediction. However, the follow-up remedy control strategies for predicted unstable systems have yet to be addressed. Further study can explore the rapid critical generator identification method, and a set of rapid control strategies to avoid the system from being unstable or minimize the consequence. It also recommend to conduct study on how virtual inertia, battery energy storage system can provide remedy support to prevent system instability.

- Extend the application of the preventive dispatch framework

The preventive dispatch method proposed in chapter 4 could be further extended to a day-ahead dispatch method and be developed as a unit commitment tool with consideration of economic efficiency and probabilistic transient stability. In addition, the framework may be improved to handle significant changes in the system topology and other situations such as under-frequency load shedding. Other state-of-the-art ML techniques may also be applied to power system preventive dispatch to achieve high-quality solutions in shorter response times.

- Study on autonomous control of power system based on reinforcement learning

The application of reinforcement learning (RL) in power system real-time control is another promising extend research. RL is an area of ML concerned with how intelligent agents ought to take actions in an environment in order to maximize the notion of cumulative reward. In power system field, this technique has been tested on some areas, including energy management and demand response. Nevertheless, the application of RL on stability-related issues is relatively undeveloped. Further study can be conducted on RL-based autonomous control of power system for stability enhancement.

List of Publications

Journal Papers

1. **Y. Chen**, S. M. Mazhari, C. Y. Chung, S. O. Faried and B. C. Pal, “Rotor angle stability prediction of power systems with high wind power penetration using a stability index vector,” *IEEE Trans. Power Syst.*, vol. 35, no. 6, pp. 4632–4643, Apr. 2020.

Conference Papers

1- **Y. Chen**, S. M. Mazhari, C. Y. Chung, S. O. Faried, B. Wang and B. Hu, “Power system online transient stability prediction by margin indices and random forests,” presented at *2019 IEEE Canada Electrical Power and Energy Conference (EPEC)*, Montreal, QC, Canada, Oct 16–18, 2019.

Appendix A Formulation of $\boldsymbol{\xi_1}$— $\boldsymbol{\xi_3}$ and $\boldsymbol{\eta_1}$–$\boldsymbol{\eta_6}$

For simplicity, assume that during fault period the value of $\boldsymbol{V}$ can be considered as $\boldsymbol{V}(t_{\mathrm{f}+})$; thus given (2.14)—(2.15), (2.24)–(2.31), and (2.43), ξ_1— ξ_3 can be derived as (A.1)–(A.3). Actually, during fault period, the real time value of $\boldsymbol{V}$ which are obtainable from PMUs can also be used for calculating (2.45) without loss of generality. η_1– η_6 are derived as (A.4) –(A.9) considering(2.14), (2.24)–(2.31), and (2.43).

$$\xi_1 = \frac{M_R}{M_T} {\boldsymbol{E}_C}^{\mathrm{T}} \mathrm{Re}(\boldsymbol{Y}_{CG}(t_{\mathrm{f}+}))\boldsymbol{V}_G(t_{\mathrm{f}+}) - \frac{M_C}{M_T} {\boldsymbol{E}_R}^{\mathrm{T}} \mathrm{Re}(\boldsymbol{Y}_{RH}(t_{\mathrm{f}+}))\boldsymbol{V}_H(t_{\mathrm{f}+}) \tag{A.1}$$

$$\xi_2 = \frac{M_R}{M_T} {\boldsymbol{E}_C}^{\mathrm{T}} \mathrm{Re}(\boldsymbol{Y}_{CH}(t_{\mathrm{f}+}))\boldsymbol{V}_H(t_{\mathrm{f}+}) - \frac{M_C}{M_T} {\boldsymbol{E}_R}^{\mathrm{T}} \mathrm{Re}(\boldsymbol{Y}_{RG}(t_{\mathrm{f}+}))\boldsymbol{V}_G(t_{\mathrm{f}+}) \tag{A.2}$$

$$\xi_3 = \frac{M_R}{M_T} {\boldsymbol{E}_C}^{\mathrm{T}} \mathrm{Im}(\boldsymbol{Y}_{CH}(t_{\mathrm{f}+}))\boldsymbol{V}_H(t_{\mathrm{f}+}) - \frac{M_C}{M_T} {\boldsymbol{E}_R}^{\mathrm{T}} \mathrm{Im}(\boldsymbol{Y}_{RG}(t_{\mathrm{f}+}))\boldsymbol{V}_G(t_{\mathrm{f}+}) \tag{A.3}$$

$$\begin{aligned}\eta_1 = {} & \frac{M_C}{M_T} {\boldsymbol{E}_R}^{\mathrm{T}} \mathrm{Re}(\boldsymbol{Y}_{RH}(t_{\mathrm{cl}+}))\big(\boldsymbol{V}_H(t_{\mathrm{cl}+}) - \boldsymbol{K}_H\delta(t_{\mathrm{cl}})\big) \\ & - \frac{M_R}{M_T} {\boldsymbol{E}_C}^{\mathrm{T}} \mathrm{Re}(\boldsymbol{Y}_{CG}(t_{\mathrm{cl}+}))\big(\boldsymbol{V}_G(t_{\mathrm{cl}+}) - \boldsymbol{K}_G\delta(t_{\mathrm{cl}})\big)\end{aligned} \tag{A.4}$$

$$\eta_2 = \frac{M_C}{2M_T} {\boldsymbol{E}_R}^{\mathrm{T}} \mathrm{Re}(\boldsymbol{Y}_{RH}(t_{\mathrm{cl}+}))\boldsymbol{K}_H - \frac{M_R}{2M_T} {\boldsymbol{E}_C}^{\mathrm{T}} \mathrm{Re}(\mathbf{Y}_{CH}(t_{\mathrm{cl}+}))\boldsymbol{K}_H \tag{A.5}$$

$$\begin{aligned}\eta_3 = {} & \frac{M_C}{M_T} {\boldsymbol{E}_R}^{\mathrm{T}} \mathrm{Re}\big(\boldsymbol{Y}_{RG}(t_{\mathrm{cl}+})\big)\big(\boldsymbol{V}_G(t_{\mathrm{cl}+}) - \boldsymbol{K}_G\delta(t_{\mathrm{cl}})\big) \\ & + \frac{M_R}{M_T} {\boldsymbol{E}_C}^{\mathrm{T}} \mathrm{Re}\big(\boldsymbol{Y}_{CH}(t_{\mathrm{cl}+})\big)\big(\boldsymbol{K}_H\delta(t_{\mathrm{cl}}) - \boldsymbol{V}_H(t_{\mathrm{cl}+})\big)\end{aligned} \tag{A.6}$$

$$\begin{aligned}\eta_4 = {} & \frac{M_C}{M_T} {\boldsymbol{E}_R}^{\mathrm{T}} \mathrm{Im}\big(\boldsymbol{Y}_{RG}(t_{\mathrm{cl}+})\big)\big(\boldsymbol{V}_G(t_{\mathrm{cl}+}) - \boldsymbol{K}_G\delta(t_{\mathrm{cl}})\big) \\ & + \frac{M_R}{M_T} {\boldsymbol{E}_C}^{\mathrm{T}} \mathrm{Im}\big(\boldsymbol{Y}_{CH}(t_{\mathrm{cl}+})\big)\big(\boldsymbol{V}_H(t_{\mathrm{cl}+}) - \boldsymbol{K}_H\delta(t_{\mathrm{cl}})\big)\end{aligned} \tag{A.7}$$

$$\eta_5 = \frac{M_C}{M_T} \boldsymbol{E}_R{}^{\mathrm{T}} \mathrm{Re}(\boldsymbol{Y}_{RG}(t_{\mathrm{cl+}})) \boldsymbol{K}_G - \frac{M_R}{M_T} \boldsymbol{E}_C{}^{\mathrm{T}} \mathrm{Re}(\boldsymbol{Y}_{CH}(t_{\mathrm{cl+}})) \boldsymbol{K}_H \tag{A.8}$$

$$\eta_6 = -\frac{M_C}{M_T} \boldsymbol{E}_R{}^{\mathrm{T}} \mathrm{Im}\big(\boldsymbol{Y}_{RG}(t_{\mathrm{cl+}})\big) \boldsymbol{K}_G - \frac{M_R}{M_T} \boldsymbol{E}_C{}^{\mathrm{T}} \mathrm{Im}\big(\boldsymbol{Y}_{CH}(t_{\mathrm{cl+}})\big) \boldsymbol{K}_H \tag{A.9}$$

Appendix B Parameters of the Components in the Modified IEEE 16-Machine 68-Bus Test System

Table B.1: Parameters of the SGs.

Description	SG1	SG2	SG3	SG4	SG5	SG6	SG7	SG8
MBASE (MVA)	600	600	700	700	600	800	600	600
T'do (s)	10.2	10.2	5.7	5.69	5.4	7.3	5.66	6.7
T"do (s)	0.05	0.05	0.05	0.05	0.05	0.05	0.05	0.05
T'qo (s)	1.5	1.5	1.5	1.5	0.44	0.4	1.5	0.41
T"qo (s)	0.035	0.035	0.035	0.035	0.035	0.035	0.035	0.035
H (s)	7	7	5.1143	4.0857	4.3333	4.35	4.4	4.05
D (pu)	0	0	0	0	0	0	0	0
Xd (pu)	0.6	0.6	1.7465	1.834	1.98	2.032	1.77	1.74
Xq (pu)	0.414	0.414	1.659	1.806	1.86	1.928	1.752	1.68
X'd (pu)	0.186	0.186	0.3717	0.3052	0.396	0.4	0.294	0.342
X'q (pu)	0.25	0.25	0.5	0.41	0.53	0.54	0.4	0.46
X" (pu)	0.15	0.15	0.315	0.245	0.3	0.32	0.24	0.27
Xℓ (pu)	0.075	0.075	0.2128	0.2065	0.162	0.1792	0.1932	0.168
$S_{1.0}$	0.001	0.001	0.001	0.001	0.001	0.001	0.001	0.001
$S_{1.2}$	0.01	0.01	0.01	0.01	0.01	0.01	0.01	0.01
Description	**SG9**	**SG10**	**SG11**	**SG12**	**SG13**	**SG14**	**SG15**	**SG16**
MBASE	900	650	1700	1500	10000	8700	8700	8000
T'do	4.79	9.37	4.1	7.4	5.9	4.1	4.1	7.8
T"do	0.05	0.05	0.05	0.05	0.05	0.05	0.05	0.05
T'qo	1.96	1.5	1.5	1.5	1.5	1.5	1.5	1.5
T"qo	0.035	0.035	0.035	0.035	0.035	0.035	0.035	0.035
H	3.8333	4.7692	1.6588	6.1533	4.96	3.4483	3.4483	5.625
D	0	0	0	0	0	0	0	0
Xd	1.8954	1.0985	2.176	1.515	1.48	1.566	1.566	1.424
Xq	1.845	0.7475	2.091	1.425	1.43	1.5051	1.5051	1.336
X'd	0.513	0.297	0.306	0.465	0.275	0.248	0.248	0.284
X'q	0.69	0.4	0.41	0.63	0.37	0.33	0.33	0.38

Table B.1 Continued

X"	0.405	0.26	0.204	0.375	0.2	0.2001	0.2001	0.22
Xℓ	0.2682	0.075	0.075	0.075	0.075	0.075	0.075	0.075
$S_{1.0}$	0.001	0.001	0.001	0.001	0.001	0.001	0.001	0.001
$S_{1.2}$	0.01	0.01	0.01	0.01	0.01	0.01	0.01	0.01

Table B.2: Parameters of the excitation systems (SG9 excluded).

Description	SG1	SG2	SG3	SG4	SG5	SG6	SG7	SG8
Type	DC4B	DC4B	DC4B	DC4B	DC4B	DC4B	DC4B	DC4B
T_R	0.01	0.01	0.01	0.01	0.01	0.01	0.01	0.01
K_P	200	200	200	200	200	200	200	200
K_I	50	50	50	50	50	50	50	50
K_D	50	50	50	50	50	50	50	50
T_D	0.01	0.01	0.01	0.01	0.01	0.01	0.01	0.01
VR_{MAX}	10	10	10	10	10	10	10	10
VR_{MIN}	-10	-10	-10	-10	-10	-10	-10	-10
K_A	1	1	1	1	1	1	1	1
T_A	0.02	0.02	0.02	0.02	0.02	0.02	0.02	0.02
K_E	1	1	1	1	1	1	1	1
T_E	0.785	0.785	0.785	0.785	0.785	0.785	0.785	0.785
K_F	0.03	0.03	0.03	0.03	0.03	0.03	0.03	0.03
T_F	1	1	1	1	1	1	1	1
VE_{MIN}	-10	-10	-10	-10	-10	-10	-10	-10
E_1	3.9267	3.9267	3.9267	3.9267	3.9267	3.9267	3.9267	3.9267
$S_E(E_1)$	0.07	0.07	0.07	0.07	0.07	0.07	0.07	0.07
E_2	5.2356	5.2356	5.2356	5.2356	5.2356	5.2356	5.2356	5.2356
$S_E(E_2$）	0.91	0.91	0.91	0.91	0.91	0.91	0.91	0.91
Description	SG10	SG11	SG12	SG13	SG14	SG15	SG16	
Type	DC4B	DC4B	DC4B	DC4B	DC4B	DC4B	DC4B	
T_R	0.01	0.01	0.01	0.01	0.01	0.01	0.01	
K_P	200	200	200	200	200	200	200	
K_I	50	50	50	50	50	50	50	

Table B.2 Continued

K_D	50	50	50	50	50	50	50	
T_D	0.01	0.01	0.01	0.01	0.01	0.01	0.01	
VR_{MAX}	10	10	10	10	10	10	10	
VR_{MIN}	-10	-10	-10	-10	-10	-10	-10	
K_A	1	1	1	1	1	1	1	
T_A	0.02	0.02	0.02	0.02	0.02	0.02	0.02	
K_E	1	1	1	1	1	1	1	
T_E	0.785	0.785	0.785	0.785	0.785	0.785	0.785	
K_F	0.03	0.03	0.03	0.03	0.03	0.03	0.03	
T_F	1	1	1	1	1	1	1	
VE_{MIN}	-10	-10	-10	-10	-10	-10	-10	
E_1	3.9267	3.9267	3.9267	3.9267	3.9267	3.9267	3.9267	
$S_E(E_1)$	0.07	0.07	0.07	0.07	0.07	0.07	0.07	
E_2	5.2356	5.2356	5.2356	5.2356	5.2356	5.2356	5.2356	
$S_E(E_2$）	0.91	0.91	0.91	0.91	0.91	0.91	0.91	

Table B.3: Parameters of the excitation system (SG9).

Description	SG9
Type	SEXS
T_A/T_B	0
T_B	0.01
K	200
T_E	0
E_{MIN}	-5

Table B.4: Parameters of the stabilizers.

Description	SG1	SG2	SG3	SG4	SG5	SG6	SG7	SG8
Type	IEEEST	IEEEST	IEEEST	IEEEST	IEEEST	IEEEST	IEEEST	IEEEST
A_1	0.04	0.04	0.04	0.04	0.04	0.04	0.04	0.04
A_2	0	0	0	0	0	0	0	0
A_3	0	0	0	0	0	0	0	0
A_4	0	0	0	0	0	0	0	0
A_5	0.15	0.15	0.15	0.15	0.15	0.15	0.15	0.15
A_6	0	0	0	0	0	0	0	0
T_1	0.15	0.15	0.15	0.15	0.15	0.15	0.15	0.15
T_2	0.04	0.04	0.04	0.04	0.04	0.04	0.04	0.04
T_3	0.15	0.15	0.15	0.15	0.15	0.15	0.15	0.15
T_4	0.04	0.04	0.04	0.04	0.04	0.04	0.04	0.04
T_5	15	15	15	15	15	15	15	15
T_6	15	15	15	15	15	15	15	15
K_S	20	20	20	20	20	20	20	20
LS_{MAX}	0.2	0.2	0.2	0.2	0.2	0.2	0.2	0.2
LS_{MIN}	-0.05	-0.05	-0.05	-0.05	-0.05	-0.05	-0.05	-0.05
V_{CU}	0	0	0	0	0	0	0	0
V_{CL}	0	0	0	0	0	0	0	0

Description	SG9	SG10	SG11	SG12	SG13	SG14	SG15	SG16
Type	IEEEST	IEEEST	IEEEST	IEEEST	IEEEST	IEEEST	IEEEST	IEEEST
A_1	0.04	0.04	0.04	0.04	0.04	0.04	0.04	0.04
A_2	0	0	0	0	0	0	0	0
A_3	0	0	0	0	0	0	0	0
A_4	0	0	0	0	0	0	0	0
A_5	0.15	0.15	0.15	0.15	0.15	0.15	0.15	0.15
A_6	0	0	0	0	0	0	0	0
T_1	0.15	0.15	0.15	0.15	0.15	0.15	0.15	0.15
T_2	0.04	0.04	0.04	0.04	0.04	0.04	0.04	0.04
T_3	0.15	0.15	0.15	0.15	0.15	0.15	0.15	0.15
T_4	0.04	0.04	0.04	0.04	0.04	0.04	0.04	0.04
T_5	15	15	15	15	15	15	15	15
T_6	15	15	15	15	15	15	15	15
K_S	20	20	20	20	20	20	20	20
LS_{MAX}	0.2	0.2	0.2	0.2	0.2	0.2	0.2	0.2
LS_{MIN}	-0.05	-0.05	-0.05	-0.05	-0.05	-0.05	-0.05	-0.05
V_{CU}	0	0	0	0	0	0	0	0
V_{CL}	0	0	0	0	0	0	0	0

Table B.5: Parameters of the electrical control model of the DFIGs.

Description	Value
Tfv, Filter time constant in voltage regulator (sec)	0.15
Kpv, Proportional gain in voltage regulator (pu)	18
KIV, Integrator gain in voltage regulator (pu)	5
Xc, Line drop compensation reactance (pu)	0
TFP, Filter time constant in torque regulator	0.05
Kpp, Proportional gain in torque regulator (pu)	3
KIP, Integrator gain in torque regulator (pu)	0.6
PMX, Max limit in torque regulator (pu)	1.12
PMN, Min limit in torque regulator (pu)	0.04
QMX, Max limit in voltage regulator (pu)	0.436
QMN, Min limit in voltage regulator (pu)	-0.436
IPMAX, Max active current limit	1.1
TRV, Voltage sensor time constant	0.02
RPMX, Max power order derivative	0.45
RPMN, Min power order derivative	-0.45
T_Power, Power filter time constant	5
Kqi, MVAR/Voltage gain	0.1
VMINCL,Min voltage limit	0.9
VMAXCL, Max voltage limit	1.1
Kqv, Voltage/MVAR gain	40
XIQmin	0.5
XIQmax	1.45
Tv, Lag time constant in WindVar controller	0.05
Tp, Pelec filter in fast PF controller	0.05
Fn, A portion of online wind turbines	1
ωPmin, Shaft speed at Pmin (pu)	0.3
ωP20, Shaft speed at 20% rated power (pu)	0.69
ωP40, Shaft speed at 40% rated power (pu)	0.78
ωP60, Shaft speed at 60% rated power (pu)	0.98
Pmin, Minimum power for operating at ωP100 speed (pu)	0.74
ωP100, Shaft speed at 100% rated power (pu)	1.2

Table B.6: Parameters of the generator/converter model of the DFIGs.

Description	Value
Tiqcmd, Converter time constant for IQcmd	0.02
Tipcmd, Converter time constant for IPcmd	0.02
KPLL, PLL gain	0
KIPLL, PLL integrator gain	0
PLLMAX, PLL max. limit	0.1
Prated	1.5
VLVPL1, LVPL voltage 1 Low voltage power logic	0.5
VLVPL2, LVPL voltage 2	0.9
GLVPL, LVPL gain	1.11
VHVRCR, High Voltage Reactive Current (HVRC) logic, pu voltage	1.2
CURHVRCR, HVRC logic, current (pu)	2
RIp_LVPL, Rate of active current change	5
T_LVPL, Voltage sensor for LVPL, second	0.02

Table B.7: Parameters of the mechanical control (wind turbine) model of the DFIGs.

Description	Value
VW, Initial wind, (pu of rated wind speed)	1.25
H, Total inertia constant, (sec)	4.95
DAMP, Machine damping factor	0
Kaero, Aerodynamic gain factor	0.007
Theta2, Blade pitch at twice rated wind speed, (deg).	21.98
Htfrac, Turbine inertia fraction (Hturb/H)	0
Freq1, First shaft torsional resonant frequency (Hz)	1.8
Dshaft, Shaft damping factor (pu)	1.5

Table B.8: Parameters of the pitch control model of the DFIGs.

Description	Value
Tp, Blade response time constant	0.3
Kpp, Proportional gain of PI regulator (pu)	150
Kip, Integrator gain of PI regulator (pu)	25
Kpc, Proportional gain of the compensator (pu)	3
Kic, Integrator gain of the compensator (pu)	30
TetaMin, Lower pitch angle limit (degrees)	0
TetaMax, Upper pitch angle limit (degrees)	27
RTetaMax, Upper pitch angle rate limit (degrees/sec)	10
P_{MX}, Power reference, pu on MBASE	1

Appendix C Cost function Coefficients of Each Generator

Each generator in the system is subject to the standard cost function (C.1), and the cost function coefficients of each generator in the modified IEEE 16-machine 68-bus test system are listed in Table C.1.

$$\text{Cost} = a_0 + a_1 P_i + a_2 P_i^2 \ (\$/\text{hour}) \qquad i \in \Omega^{\text{gen}} \tag{C.1}$$

Table C.1: Cost function coefficients of each generator.

Generator	a_0 (\$)	a_1 (\$/MWh)	a_2 (\$/MW^{2}h)	P_{max} (MW)	P_{min} (MW)	Q_{min} (MVAr)	Q_{min} (MVAr)
SG1	0	6.9	0.0193	375	100	148.5	-148.5
SG2	0	3.7	0.0111	817.5	100	248.5	-248.5
SG3	0	2.8	0.0104	975	100	280.5	-280.5
SG4	0	4.7	0.0088	948	100	274.56	-274.56
SG5	0	2.8	0.0128	757.5	100	232.65	-232.65
SG6	0	3.7	0.0094	1050	100	297	-297
SG7	0	4.8	0.0099	840	100	250.8	-250.8
SG8	0	3.6	0.0113	810	100	244.2	-244.2
SG9	0	3.7	0.0071	1200	100	330	-330
SG10	0	3.9	0.009	750	100	231	-231
SG11	0	4	0.005	1250	500	396	-396
SG12	0	2.9	0.004	1687.5	500	511.5	-511.5
SG13	0	2.5	0.0019	4488.8	2000	1060.29	-1060.29
SG14	0	3.3	0.0033	2231.3	500	655.05	-655.05
SG15	0	3.8	0.005	1250	500	396	-396
SG16	0	3.5	0.0014	5000	3000	1386	-1386

Appendix D Copyright Permission Letters from Co-Authors

To Whom It May Concern:

I, Chi Yung Chung, hereby grant permission to Mr. Yuchuan Chen to include the following paper in his thesis titled “Machine Learning-Incorporated Transient Stability Prediction and Preventive Dispatch for Power Systems with High Wind Power Penetration”.

1. Y. Chen, S. M. Mazhari, **C. Y. Chung**, S. O. Faried and B. C. Pal, “Rotor angle stability prediction of power systems with high wind power penetration using a stability index vector,” *IEEE Trans. Power Syst.*, vol. 35, no. 6, pp. 4632–4643, Apr. 2020.

2. Y. Chen, S. M. Mazhari, **C. Y. Chung**, S. O. Faried, B. Wang and B. Hu, “Power system on-line transient stability prediction by margin indices and random forests,” presented at *2019 IEEE Canada Electrical Power and Energy Conference (EPEC)*, Montreal, QC, Canada, Oct 16–18, 2019.

I am aware that all University of Saskatchewan theses are also posted in the digital USask eCommons thesis repository, making the thesis openly available on the internet.

Date:

Signature:

To Whom It May Concern:

I, Sherif Omar Faried, hereby grant permission to Mr. Yuchuan Chen to include the following paper in his thesis titled “Machine Learning-Incorporated Transient Stability Prediction and Preventive Dispatch for Power Systems with High Wind Power Penetration”.

1. Y. Chen, S. M. Mazhari, C. Y. Chung, **S. O. Faried** and B. C. Pal, “Rotor angle stability prediction of power systems with high wind power penetration using a stability index vector,” *IEEE Trans. Power Syst.*, vol. 35, no. 6, pp. 4632–4643, Apr. 2020.

2. Y. Chen, S. M. Mazhari, C. Y. Chung, **S. O. Faried**, B. Wang and B. Hu, “Power system on-line transient stability prediction by margin indices and random forests,” presented at *2019 IEEE Canada Electrical Power and Energy Conference (EPEC)*, Montreal, QC, Canada, Oct 16–18, 2019.

I am aware that all University of Saskatchewan theses are also posted in the digital USask eCommons thesis repository, making the thesis openly available on the internet.

Date:

Signature:

To Whom It May Concern:

I, Seyed Mahdi Mazhari, hereby grant permission to Mr. Yuchuan Chen to include the following paper in his thesis titled "Machine Learning-Incorporated Transient Stability Prediction and Preventive Dispatch for Power Systems with High Wind Power Penetration".

1. Y. Chen, **S. M. Mazhari**, C. Y. Chung, S. O. Faried and B. C. Pal, "Rotor angle stability prediction of power systems with high wind power penetration using a stability index vector," *IEEE Trans. Power Syst.*, vol. 35, no. 6, pp. 4632–4643, Apr. 2020.

2. Y. Chen, **S. M. Mazhari**, C. Y. Chung, S. O. Faried, B. Wang and B. Hu, "Power system online transient stability prediction by margin indices and random forests," presented at *2019 IEEE Canada Electrical Power and Energy Conference (EPEC)*, Montreal, QC, Canada, Oct 16–18, 2019.

I am aware that all University of Saskatchewan theses are also posted in the digital USask eCommons thesis repository, making the thesis openly available on the internet.

Date:

Signature:

To Whom It May Concern:

I, Bikash Chandra Pal, hereby grant permission to Mr. Yuchuan Chen to include the following paper in his thesis titled “Machine Learning-Incorporated Transient Stability Prediction and Preventive Dispatch for Power Systems with High Wind Power Penetration”.

1. Y. Chen, S. M. Mazhari, C. Y. Chung, S. O. Faried and **B. C. Pal**, “Rotor angle stability prediction of power systems with high wind power penetration using a stability index vector,” *IEEE Trans. Power Syst.*, vol. 35, no. 6, pp. 4632–4643, Apr. 2020.

I am aware that all University of Saskatchewan theses are also posted in the digital USask eCommons thesis repository, making the thesis openly available on the internet.

Date:

Signature:

To Whom It May Concern:

I, Bingzhi Wang, hereby grant permission to Mr. Yuchuan Chen to include the following paper in his thesis titled “Machine Learning-Incorporated Transient Stability Prediction and Preventive Dispatch for Power Systems with High Wind Power Penetration”.

1. Y. Chen, S. M. Mazhari, C. Y. Chung, S. O. Faried, **B. Wang** and B. Hu, “Power system on-line transient stability prediction by margin indices and random forests,” presented at *2019 IEEE Canada Electrical Power and Energy Conference (EPEC)*, Montreal, QC, Canada, Oct 16–18, 2019.

I am aware that all University of Saskatchewan theses are also posted in the digital USask eCommons thesis repository, making the thesis openly available on the internet.

Date:

Signature:

To Whom It May Concern:

I, Bo Hu, hereby grant permission to Mr. Yuchuan Chen to include the following paper in his thesis titled "Machine Learning-Incorporated Transient Stability Prediction and Preventive Dispatch for Power Systems with High Wind Power Penetration".

1. Y. Chen, S. M. Mazhari, C. Y. Chung, S. O. Faried, B. Wang and **B. Hu**, "Power system online transient stability prediction by margin indices and random forests," presented at *2019 IEEE Canada Electrical Power and Energy Conference (EPEC)*, Montreal, QC, Canada, Oct 16–18, 2019.

I am aware that all University of Saskatchewan theses are also posted in the digital USask eCommons thesis repository, making the thesis openly available on the internet.

Date:

References

[1] P. Kundur *et al.*, "Definition and classification of power system stability," *IEEE Trans. Power Syst.*, vol. 19, pp. 1387–1401, 2004.

[2] P. N. Papadopoulos and J. V. Milanovic, "probabilistic framework for transient stability assessment of power systems with high penetration of renewable generation," *IEEE Trans. Power Syst.*, vol. 32, no. 4, pp. 3078–3088, 2017.

[3] D. Gautam, V. Vittal, and T. Harbour, "Impact of increased penetration of DFIG-based wind turbine generators on transient and small signal stability of power systems," *IEEE Trans. Power Syst*., vol. 24, no. 3, pp. 1426–1434, Aug. 2009.

[4] R. Yousefian, R. Bhattarai, and S. Kamalasadan, "Transient stability enhancement of power grid with integrated wide area control of wind farms and synchronous generators," *IEEE Trans. Power Syst.*, vol. 32, no. 6, pp. 4818–4831, Nov. 2017.

[5] A. K. Ekanth Vittal, Mark O'Malley, "Rotor angle stability with high penetration of wind generation," *IEEE Trans. Power Syst.*, vol. 27, no. 1, pp. 353–362, 2012.

[6] A. Mohammed, B. Tarek, "Power system transient stability analysis with high wind power penetration," *International Electrical Engineering Journal*. vol. 4, no. 1, pp. 907-913, 2013

[7] M. Rostami and S. Lotfifard, "Scalable coordinated control of energy storage systems for enhancing power system angle stability," *IEEE Trans. Sustain. Energy*, vol. 9, no. 2, pp. 763–770, Apr. 2018.

[8] M. Edrah, K. L. Lo, and O. Anaya-Lara, "Impacts of high penetration of DFIG wind turbines on rotor angle stability of power systems," *IEEE Trans. Sustain. Energy*, vol. 6, no. 3, pp. 759–766, Jul. 2015.

[9] J. Ruan, Z. Lu, Y. Qiao, and Y. Min, "Transient stability of wind turbine adopting a generic model of DFIG and singularity-induced instability of generators/units with power-electronic interface," *IEEE. Trans. Energy Convers*., vol. 30, no. 3, pp. 1069–1080, May 2015.

[10] GWEC, "Global Wind Energy Outlook 2016: Wind Power to dominate power sector growth", [Online]. Available: http://gwec.net/publications/global-wind-energy-outlook/global-wind-energy-outlook-2016/http://gwec.net/publications/global-wind-energy-outlook/global-wind-energy-outlook-2016/

[11] GWEC. Global wind report 2019. *Tech. rep.*, Global Wind Energy Council; 2020. [online] Available: https://gwec.net/wp-content/uploads/2020/08/Annual-Wind-Report_2019_digital_final_2r.pdf

[12] Https://canwea.ca/wind-energy/installed-capacity/

[13] Https://canwea.ca/blog/2015/11/27/saskpower-capitalizes-on-wind-energys-cost-competitiveness/

[14] IEA. IEA WIND 2019 annual report. *Tech. rep*. International Energy Agency;2020. . [online] Available: https://community.ieawind.org/publications/ar#:~:text=IEA%20Wind%20TCP%202019%20Annual%20Report&text=This%20report%20provides%20a%20summary,to%20the%20world%20energy%20supply.

[15] Https://www.epaper.dk/steppaper/iea2/us-chapters/

[16] P. Kundur, *Power System Stability and Control*. New York: McGraw- Hill, 1994.

[17] S. M. Mazhari, N. Safari, C. Y. Chung, and I. Kamwa, “A Hybrid fault cluster and thevenin equivalent based framework for rotor angle stability prediction,” *IEEE Transactions on Power Systems*, vol. 33, no. 5, pp. 5594–5603, Jul. 2018.

[18] P. M. Anderson and A. A. Fouad, *Power System Control and Stability*, 2nd ed. Piscataway, NJ: IEEE, 2003.

[19] J. R. B. Jan Machowski, Janusz W. Bialek, *Power System Dynamics Stability and Control*, no. December. 2006.

[20] DSATools. [online] Available: https://www.dsatools.com/

[21] DIgSILENT. [online] Available: https://www.digsilent.de/en/

[22] EMTP. [online] Available: https://www.emtp.com/

[23] ETAP. [online] Available: https://www.etap.com/

[24] Power World. [online] Available: https://www.powerworld.com/

[25] Siemens Power Technologies International, PSS®E 34.2 Program Application Guide: Volume 2, Apr 2017.

[26] PSCAD. [online] Available: https://www.pscad.com/

[27] L. Wehenkel, T. V. Cutsem, and M. Ribbens-Pavella, “An artificial intelligence framework for online transient stability assessment of power systems,” *IEEE Trans. Power Syst*., vol. 4, no. 2, pp. 789–800, May 1989.

[28] M. A. Pai, K. R. Padiyar, and C. RadhaKrishna, “Transient stability analysis of multi-machine AC/DC power systems via energy-function method,” *IEEE Trans. Power App. Syst.*, vol. PAS-100, no. 12, pp. 5027–5035, Dec. 1981

[29] A. N. Michel, A. A. Fouad and V. Vittal, “Power system transient stability using individual machine energy functions”, *IEEE Trans. Circuits Syst.*, Vol. CAS-30, no. 5, pp. 266–276, May. 1983.

[30] N. A. Tsolas, A. Arapostathis, and P.P.Varaiya, “A structure preserving energy function for power system transient stability analysis,” *IEEE Trans. Circuits Syst*., vol. CAS-32, no. 10, pp. 1041–1049, Oct. 1985.

[31] H.D.Chiang, F.F. Wu, and P.P. Varaiya. “Foundations of direct methods for power system transient stability analysis,” *IEEE Trans. Circuits Syst.*, vol. 34, no. 2, pp. 160–173, Feb. 1987.

[32] Y. Xue, T. Van Cutsem, and M. Ribbens-Pavella, “A simple direct method for fast transient stability assessment of large power systems,” *IEEE Trans. Power Syst.*, vol. 3, no. 2, pp. 400–412, 1988.

[33] H. D. Chiang, F. F. Wu, and P. P. Varaiya, "Foundations of the potential energy boundary surface method for power system transient stability analysis," *IEEE Trans. Power Syst.*, vol. 35, no. 6, pp. 712–728, Jun. 1988.

[34] A. A. Fouad, V. Vittal, and T. K. Oh, "Critical energy for direct transient stability assessment of a multi-machine power system," *IEEE Trans. Power App. Syst.*, vol. PAS-103, no. 8, pp. 2199–2206, Aug. 1984.

[35] H.D. Chiang, F. F. Wu, and P. P. Varaiya, "A BCU Method for direct analysis of power system transient stability," *IEEE Trans. Power Syst.*, vol. 9, no. 3, pp. 1194–1208, Aug. 1994.

[36] A. R. Bergen and D.J. Hill, "A Structure preserving model for power system stability analysis," *IEEE Trans. Power App. Syst.*, vol. PAS-100, no. 1, pp. 25–35, Jan. 1981.

[37] M. Pavella, D. Ernst, and D. Ruiz-Vega, *Transient Stability of Power Systems: A Unified Approach to Assessment and Control*. Kluwer Academic Publishers, 2000.

[38] Y. Zhang, L. Wehenkel, P. Rousseaux, and M. Pavella, "SIME: A hybrid approach to fast transient stability assessment and contingency selection," *Electrical Power & Energy Systems*, vol. 19, no. 3, pp. 195–208, Mar. 1997.

[39] D. Ernst, D. Ruiz-Vega, M. Pavella, P. M. Hirsch, and D. Sobajic, "A unified approach to transient stability contingency filtering, ranking and assessment," *IEEE Trans. Power Syst.*, vol. 16, no. 3, pp. 435–443, Aug. 2001.

[40] D. Ruiz-Vega and M. Pavella, "A comprehensive approach to transient stability control: part I: near optimal preventive control," *IEEE Trans. Power Syst.*, vol. 18, no. 4, pp. 1446–1453, Nov. 2003.

[41] T. L. Vu and K. Turitsyn, "Lyapunov functions family approach to transient stability assessment," *IEEE Trans. Power Syst.*, vol. 31, no. 2, pp. 1269–1277, 2016.

[42] D. Rimorov, X. Wang, I. Kamwa, and G. Joos, "An approach to constructing analytical energy function for synchronous generator models with subtransient dynamics," *IEEE Trans. Power Syst.*, vol. 33, no. 6, pp. 5958–5967, 2018.

[43] P. Bhui and N. Senroy, "Real-time prediction and control of transient stability using transient energy function," *IEEE Trans. Power Syst.*, vol. 32, no. 2, pp. 923–934, 2017.

[44] Z. Lin, F. Wen, Y. Ding, and Y. Xue, "Data-driven coherency identification for generators based on spectral clustering," *IEEE Trans. Ind. Informatics*, vol. 14, no. 3, pp. 1275–1285, 2018.

[45] J. Wei, D. Kundur, and K. L. Butler-Purry, "A novel bio-inspired technique for rapid real-time generator coherency identification," *IEEE Trans. Power Syst.*, vol. 6, no. 1, pp. 178–188, 2015.

[46] Y. Wu, M. Musavi, and P. Lerley, "Synchrophasor-based monitoring of critical generator buses for transient stability," *IEEE Trans. Power Syst.*, vol. 31, no. 1, pp. 287–295, Jan. 2016.

[47] *IEEE Standard for Synchrophasor Data Transfer for Power Systems*, IEEE Std. C37.118.2-2011, Dec. 2011.

[48] R. Ghiga, K. Martin, Q. Wu, and A. H. Nielsen, “Phasor Measurement unit test under interference conditions,” *IEEE Trans. Power Deliv.*, vol. 33, no. 2, pp. 630–639, Apr. 2018.

[49] J. Warichet, T. Sezi, T, J.C., Maun, “Considerations about synchrophasors measurements in dynamic system conditions,” *International Transactions on Electrical Energy System*, 2009.

[50] P. Jena, A.K. Pradhan, “Reducing current transformer saturation effect in phasor measurement unit,” *Int. Trans. Electr. Energ. Syst.*, 2016

[51] A.G. Phadke, B. Kasztenny, “Synchronized phasor and frequency measurement under transient conditions,” *IEEE Trans. Power Deliv.*, vol. 24, no. 1, pp. 89–95, Jan. 2009.

[52] D. M. Laverty, D. J. Morrow, A. McKinley, and M. Cregan, "OpenPMU: open source platform for synchrophasor applications and research," in *IEEE Power and Energy Society General Meeting*, Detroit, USA, 2011.

[53] A. G. Phadke and J. S. Thorp, Synchronized Phasor Measurements and Their Applications. New York: Springer, 2008.

[54] T. Amraee and S. Ranjbar, “Transient instability prediction using decision tree technique,” *IEEE Trans. Power Syst.*,. vol. 28, no. 3, pp. 3028–3037, 2013.

[55] T. Guo, G. S. Member, and J. V Milanovic, “Probabilistic framework for assessing the accuracy of data mining tool for online prediction of transient stability,” *IEEE Trans. Power Syst.*, vol. 29, no. 1, pp. 377–385, 2014.

[56] T. Guo, S. Member, and J. V Milanović, “Online identification of power system dynamic signature using PMU measurements and data mining,” *IEEE Trans. Power Syst.*, vol. 31, no. 3, pp. 1760–1768, 2016.

[57] H. Supreme, L.A. Dessaint, I. Kamwa, and A. Heniche-Oussedik, “Development of new predictors based on the concept of center of power for transient and dynamic instability detection,” *IEEE Trans. Smart Grid.*, vol. pp, no. 99, pp. 1–11, 2017.

[58] P. N. Papadopoulos, T. Guo, and J. V. Milanovic, “Probabilistic framework for online identification of dynamic behavior of power systems with renewable generation,” *IEEE Trans. Power Syst.*, vol. 33, no. 1, pp. 45-54, 2018.

[59] M. C. Passaro, A. P. A. Da Silva, and A. C. S. Lima, “Preventive control stability via neural network sensitivity,” *IEEE Trans. Power Syst.*, vol. 29, no. 6, pp. 2846–2853, 2014.

[60] J. J. Q. Yu, D. J. Hill, A. Y. S. Lam, J. Gu, and V. O. K. Li, “Intelligent time-adaptive transient stability assessment system,” *IEEE Trans. Power Syst.*, vol. 33, no. 1, pp. 1049–1058, Jan. 2018.

[61] F. R. Gomez, A. D. Rajapakse, S. Member, U. D. Annakkage, S. Member, and I. T. Fernando, “Support vector machine-based algorithm for post-fault transient stability status prediction using synchronized measurements,” *IEEE Trans. Power Syst.*, vol. 26, no. 3, pp. 1474–1483, 2011.

[62] Y. Zhou, J. Wu, “Support vector machine ensemble classifier and its confidence evaluation for transient stability prediction of power systems”, *Power System Technology.* vol. 41, no. 4, pp. 1188–1196, Apr. 2017.

[63] R. Zhang, Y. Xu, Z. Y. Dong, and K. P. Wong, "Post-disturbance transient stability assessment of power systems by a self-adaptive intelligent system.," *IET Gener. Transm. Distrib.*, vol. 9, no. March 2014, pp. 296–305, 2015.

[64] B. Wang, B. Fang, Y. Wang, H. Liu, and Y. Liu, "Power system transient stability assessment based on big data and the core vector machine," *IEEE Trans. Smart Grid.*, vol. 7, no. 5, pp. 2561–2570, Sep. 2016.

[65] J. Bosch, I. Staffell, and A. D. Hawkes, "Temporally-explicit and spatially-resolved global onshore wind energy potentials," *Energy*, vol. 131, pp. 207–217, Jul. 2017.

[66] Y. Tang, F. Li, Q. Wang, and Y. Xu, "Hybrid method for power system transient stability prediction based on two-stage computing resources," *IET Gener. Transm. Dis.*, vol. 12, no. 8, pp. 1697–1703, Apr. 2018.

[67] D. Gan, R. J. Thomas, and R. D. Zimmerman, "Stability-constrained optimal power flow," *IEEE Trans. Power Syst.*, vol. 15, no. 2, pp. 535–540, May 2000.

[68] Q. Jiang, B. Zhou, and M. Zhang, "Parallel augment lagrangian relaxation method for transient stability constrained unit commitment," *IEEE Trans. Power Syst.*, vol. 28, no. 2, pp. 1140–1148, 2013.

[69] C. J. Ye and M. X. Huang, "Multi-objective optimal power flow considering transient stability based on parallel NSGA-II," *IEEE Trans. Power Syst.*, vol. 30, no. 2, pp. 857–866, Mar. 2015.

[70] L. Tang and W. Sun, "An automated transient stability constrained optimal power flow based on trajectory sensitivity analysis," *IEEE Trans. Power Syst.*, vol. 32, no. 1, pp. 590–599, Jan. 2017.

[71] A. Pizano-Martínez, C. R. Fuerte-Esquivel, E. A. Zamora-Cárdenas, and J. M. Lozano-Garcia, "Directional derivative-based transient stability-constrained optimal power flow," *IEEE Trans. Power Syst.*, vol. 32, no. 5, pp. 3415–3426, Sep. 2017.

[72] D. Ruiz-Vega and M. Pavella, "A comprehensive approach to transient stability control I: Near optimal preventive control," *IEEE Trans. Power Syst.*, vol. 18, no. 4, pp. 1446–1453, Nov. 2003.

[73] A. Pizano-Martinez, C. R. Fuerte-Esquivel, and D. Ruiz-Vega, "Global transient stability-constrained optimal power flow using an OMIB reference trajectory," *IEEE Trans. Power Syst.*, vol. 25, no. 1, pp. 392–403, Feb. 2010

[74] Y. Xu, J. Ma, Z. Y. Dong, and D. J. Hill, "Robust transient stability-constrained optimal power flow with uncertain dynamic loads," *IEEE Trans. Smart Grid.*, vol. 8, no. 4, pp. 1911–1921, Jul. 2017.

[75] H. R. Cai, C. Y. Chung, and K. P. Wong, "Application of differential evolution algorithm for transient stability constrained optimal power flow," *IEEE Trans. Power Syst.*, vol. 23, no. 2, pp. 719–728, May 2008.

[76] S. W. Xia, B. Zhou, K. W. Chan, and Z. Z. Guo, "An improved GSO method for discontinuous non-convex transient stability constrained optimal power flow with complex system model," *Int. J. Electr. Power Energy Syst.*, vol. 64, pp. 483–492, 2015.

[77] Data download from the website: https://transmission.bpa.gov/Business/Operations/Wind/

[78] R. Canyasse, G. Dalal, and S. Mannor, “Supervised learning for optimal power flow as a real-time proxy,” in *Proc. IEEE PES Innovative Smart Grid Technol.*, 2017, pp. 1–5.

[79] M. Ghofrani, A. Arabali, M. Etezadi-Amoli, and M. S. Fadali, “A framework for optimal placement of energy storage units within a power system with high wind penetration,” *IEEE Trans. Sustain. Energy*, vol. 4, no. 2, pp. 434–442, Apr. 2013.

[80] R. Billinton and P. R. S. Kuruganty, “Probabilistic assessment of transient stability in a practical multimachine system,” *IEEE Trans. Power App. Syst.*, vol. PAS-100, no. 7, pp. 3634–3641, Jul. 1981.

[81] S. O. Faried, R. Billinton, and S. Aboreshaid, “Probabilistic evaluation of transient stability of a wind farm,” *IEEE Trans. Energy Convers.*, vol. 24, no. 3, pp. 733–739, Sep. 2009.

[82] S. Xia, X. Luo, K. W. Chan, M. Zhou, and G. Li, “Probabilistic transient stability constrained optimal power flow for power systems with multiple correlated uncertain wind generations,” *IEEE Trans. Sustain. Energy*, vol. 7, no. 3, pp. 1133–1144, Jul. 2016.

[83] K. Hua, Y. Mishra, and G. Ledwich, “Fast unscented transformation-based transient stability margin estimation incorporating uncertainty of wind generation,” *IEEE Trans. Sustain. Energy*, vol. 6, no. 4, pp. 1254–1262, Oct. 2015.

[84] Y. Xu, M. Yin, Z. Y. Dong, R. Zhang, D. J. Hill, and Y. Zhang, “Robust dispatch of high wind power-penetrated power systems against transient instability,” *IEEE Trans. Power Syst.*, vol. 33, no. 1, pp. 174–186, Jan. 2018.

[85] S. J. Russell, P. Norvig, Artificial Intelligence: A Modern Approach, 3rd ed, Prentice Hall ISBN 9780136042594, 2010

[86] F. Golestaneh, P. Pinson, and H. B. Gooi, “Very short-term nonparametric probabilistic forecasting of renewable energy generation - With application to solar energy,” *IEEE Trans. Power Syst.*, vol. 31, no. 5, pp. 3850–3863, Sep. 2016.

[87] L. S. Moulin, A. P. Alves Da Silva, M. A. El-Sharkawi, and R. J. Marks, “Support vector machines for transient stability analysis of large-scale power systems,” *IEEE Trans. Power Syst.*, vol. 19, no. 2, pp. 818–825, May 2004.

[88] C. Wan, Z. Xu, P. Pinson, Z. Y. Dong, and K. P. Wong, “Probabilistic forecasting of wind power generation using extreme learning machine,” *IEEE Trans. Power Syst.*, vol. 29, no. 3, pp. 1033–1044, 2014.

[89] M. He and D. He, “Deep learning based approach for bearing fault diagnosis,” *IEEE Trans. Ind. Appl.*, vol. 53, no. 3, pp. 3057–3065, May 2017.

[90] O. A. Alimi, K. Ouahada, and A. M. Abu-Mahfouz, “A review of machine learning approaches to power system security and stability,” *IEEE Access*, vol. 8, pp. 113512–113531, 2020.

[91] Y. Xu, Z. Y. Dong, J. H. Zhao, P. Zhang, and K. P. Wong, “A reliable intelligent system for real-time dynamic security assessment of power systems,” *IEEE Trans. Power Syst.*, vol. 27, no. 3, pp. 1253–1263, 2012.

[92] J. L. Cremer, I. Konstantelos, S. H. Tindemans, and G. Strbac, “Data-driven power system operation: Exploring the balance between cost and risk,” *IEEE Trans. Power Syst.*, vol. 34, no. 1, pp. 791–801, Jan. 2019.

[93] F. L. Quilumba, W. Lee, H. Huang, D. Y. Wang and R. L. Szabados, "Using smart meter data to improve the accuracy of intraday load forecasting considering customer behavior similarities," *IEEE Trans. Smart Grid.*, vol. 6, no. 2, pp. 911-918, March 2015.

[94] Q. Liu, K. M. Kamoto, X. Liu, M. Sun and N. Linge, "Low-complexity non- intrusive load monitoring using unsupervised learning and generalized appliance models," *IEEE Trans. Consum. Electron.*, vol. 65, no. 1, pp. 28-37, Feb. 2019.

[95] A. A. Munshi and Y. A. I. Mohamed, "Unsupervised nonintrusive extraction of electrical vehicle charging load patterns," *IEEE Trans. Ind. Informatics.*, vol. 15, no. 1, pp. 266-279, Jan. 2019.

[96] E. Mocanu, D. C. Mocanu, P. H. Nguyen, A. Liotta, M. E. Webber, M. Gibescu, and J. G. Slootweg, “On-line building energy optimization using deep reinforcement learning,” *IEEE Trans. Smart Grid.*, vol. 10, no. 4, pp. 3698–3708, Jul. 2019.

[97] Z. Q. Wan, H. P. Li, H. B. He, and D. Prokhorov, “Model-free real- time EV charging scheduling based on deep reinforcement learning, ” *IEEE Trans. Smart Grid.*, vol. 10, no. 5, pp. 5246–5257, Sep. 2019.

[98] R. Z. Lu and S. H. Hong, “Incentive-based demand response for smart grid with reinforcement learning and deep neural network,” *Applied Energy*, vol. 236, pp. 937–949, Feb. 2019.

[99] T. Remani, E. A. Jasmin, and T. P. ImthiasAhamed, “Residential load scheduling with renewable generation in the smart grid: a reinforcement learning approach,” *IEEE Systems Journal*, vol. 13, no. 3, pp. 3283– 3294, Sep. 2019.

[100] T. Chen and W. C. Su, “Indirect customer-to-customer energy trading with reinforcement learning,” *IEEE Trans. Smart Grid.*, vol. 10, no. 4, pp. 4338–4348, Jul. 2018.

[101] H. C. Xu, H. B. Sun, D. Nikovski, S. Kitamura, K. Mori, and H. Hashimoto, “Deep reinforcement learning for joint bidding and pricing of load serving entity, ” *IEEE Trans. Smart Grid.*, Vol. 10, no. 6, pp. 6366–6375, Nov. 2019.

[102] X. S. Zhang, Q. Li, T. Yu, and B. Yang, “Consensus transfer Q- learning for decentralized generation command dispatch based on virtual generation tribe,” *IEEE Trans. Smart Grid*, vol. 9, no. 3, pp. 2152–2165, May 2018.

[103] Z. M. Yan and Y. Xu, “Data-driven load frequency control for stochastic power systems: a deep reinforcement learning method with continuous action search,” *IEEE Trans. Power Syst.*, vol. 34, no. 2, pp. 1653–1656, Mar. 2018.

[104] J. P. Barddal, H. M. Gomes, and F. Enembreck, “Analyzing the impact of feature drifts in streaming learning,” in *Proc. ICONIP*, Istanbul, Turkey, 2015, pp. 21–28.

[105] J. Tilman G. Weckesser, “General rights on-line dynamic security assessment in power systems.” Ph.D. dissertation, Technical University of Denmark, Denmark, 2014.

[106] Y. Xue, T. Van Cutsem, and M. Ribbens-Pavella, “Extended equal area criterion justifications, generalizations, applications,” *IEEE Trans. Power Syst.*, vol. 4, no. 1, pp. 44–52, 1989.

[107] A. M. Khalil and R. Iravani, “A dynamic coherency identification method based on frequency deviation signals,” *IEEE Trans. Power Syst.*, vol. 31, no. 3, pp. 1779–1787, May. 2016.

[108] A. M. Khalil and R. Iravani, “Power system coherency identification under high depth of penetration of wind power,” *IEEE Trans. Power Syst.*, vol. 33, no. 5, pp. 5401–5409, Sep. 2018.

[109] WECC *Wind Plant Dynamic Modelling Guidelines*, May 2014, [online] Available: https://www.wecc.org/reliability/wecc%20wind%20plant%20dynamic%20modelling%20guidelines.pdf

[110] D. Wang, H. Wang, J. Jia, and Y. Zhang, “Reactive power control of doubly fed induction generator in wind farm under low grid voltage,” in *Proc., CRIS 2010,* Beijing, China, 2010, pp. 1–6.

[111] Y. Lei, A. Mullane, G. Lightbody, and R. Yacamini, “Modelling of the wind turbine with a doubly fed induction generator for grid integration studies,” *IEEE Trans. Energy Convers.*, vol. 21, no. 1, pp. 257–264, Mar. 2006.

[112] J.W. Lee, W.K Kim, J. Han, and W.H. Jang, C.H Kim, “Fault area estimation using traveling wave for wide area protection,” *J. Mod. Power Syst. Clean Energy,* vol. 4, no. 3, pp. 478–486, 2016.

[113] Q. Jiang, X. Li, B. Wang, and H. Wang, “PMU-based fault location using voltage measurements in large transmission networks,” *IEEE Trans. Power Del.*, vol. 27, no. 3, pp. 1644–1652, 2012.

[114] J. Ma, J.L Li, Z.P. Wang, and Q.X. Yang, “A novel wide-area fault location algorithm based on fault model,” in *Proc. Power and Energy Engineering Conf.*, pp. 1-4, 2010.

[115] P. Bhui and N. Senroy, “Online identification of tripped line for transient stability assessment,” *IEEE Trans. Power Syst.*, vol. 31, no. 3, pp. 2214–2224, 2016.

[116] Y. Ge, A.J. Flueck, D.K. Kim, and J.B. Ahn, J.D. Lee, D.Y Kwon, “Power system real-time event detection and associated data archival reduction based on synchrophasors,” *IEEE Trans. Smart Grid.,* vol. 6, no. 4, pp. 2088–2097, 2015.

[117] S. Wei, M. Yang, J. Qi, J. Wang, S. Ma, and X. Han, “Model-Free MLE Estimation for Online Rotor Angle Stability Assessment with PMU Data,” *IEEE Trans. Power Syst.*, vol. 33, no. 3, pp. 2463–2476, May. 2018.

[118] A. K. Singh and B. C. Pal, “Report on the 68-bus, 16-machine, 5-area system,” *IEEE PES Task Force on Benchmark Systems for Stability Controls,* Ver. 3.3, 2013.

[119] T. Hong, P. Pinson, S. Fan, H. Zareipour, A. Troccoli, and R. J. Hyndman, “Probabilistic energy forecasting: Global Energy Forecasting Competition 2014 and beyond,” *Int. J. Forecast.*, vol. 32, no. 3, pp. 896–913, Jul. 2016.

[120] Data download from the website: http://www.pjm.com/markets-and-operations/ops-analysis/historical-load-data.aspx.

[121] L. Breiman, J. H. Friedman, R. A. Olshen, and C. J. Stone, “Classification and regression trees,” *Wadsworth & Brooks Monterey,* CA, 1984.

[122] Y. Freund and R. E. Schapire, “A decision-theoretic generalization of on-line learning and an application to boosting,” *J. Comput. Syst. Sci.*, vol. 55, no. 1, pp. 119–139, 1997.

[123] R. Zimmerman C. E. Murillo-Sánchez, and R. J. Thomas, “MATPOWER steady-state operations, planning and analysis tools for power systems research and education,” *IEEE Trans. Power Syst.*, vol. 26, no. 1, pp. 12–19, Feb. 2011.

[124] F. Pedregosa *et al.*, “Scikit-learn: Machine learning in python,” *J. Mach. Learn. Res.*, vol. 12, no. Oct, pp. 2825–2830, 2011.

[125] Data download from the website: https://setis.ec.europa.eu/EMHIRES-datasets.

[126] C. Wang, R. Gao, F. Qiu, J. Wang, and L. Xin, “Risk-based distributionally robust optimal power flow with dynamic line rating,” *IEEE Trans. Power Syst.*, vol. 33, no. 6, pp. 6074–6086, Jun. 2018.

[127] R. T. F. A. King, X. Tu, and L. A. Dessaint, “Independent component analysis for feature reduction in critical clearing time estimation,” in *Proc. CCECE 2016*, Vancouver, BC, Canada, 2016, pp. 1–5.

[128] J. Zhu, H. Zou, S. Rosset, and T. Hastie, “Multi-class AdaBoost,” *Statist. Interface*, vol. 2, no. 1, pp. 349–360, 2009.

[129] H. Drucker, “Improving regressors using boosting techniques,” in *Proc. 14th Int. Conf. Mach. Learn.*, 1997, pp. 107–115.

[130] J. Ma, C. Wang, M. Yang, and Y. Lin, “Ultra-short-term probabilistic wind turbine power forecast based on empirical dynamic modelling,” *IEEE Trans. Sustain. Energy*, vol. 11, no. 2, pp. 906–915, Apr. 2020.

[131] B. W. Silverman, *Density estimation for statistics and data analysis*, vol. 26. Boca Raton, FL, USA: CRC Press, 1986.

[132] R. Preece, “A probabilistic approach to improving the stability of meshed power networks with embedded HVDC lines,” Ph.D. dissertation, Univ. Manchester, Manchester, U.K., 2013.

[133] IEEE *Guide for Breaker Failure Protection of Power Circuit Breakers*,” IEEE Std. C37.119-2016 Jul. 2016.